Modelling of non-ideal steady detonations

Malcolm Cartwright

The University of Leeds

Department of Applied Mathematics

Submitted in accordance with the requirements for the degree of

Doctor of Philosophy

September 2016

The candidate confirms that the work submitted is his own and that appropriate credit has been given where reference has been made to the work of others.

Acknowledgements

I would like to thank my supervisor Sam Falle for his patience, guidance and friendship over the course of my PhD studies. I am also grateful to Nicholas Whitworth, Robin Williams, Caroline Handley, Alex Hodgson and Brian Lambourn (all of AWE) for their insight and useful discussions. Thank you to my family for always being there for me. And finally to Gary Sharpe, without whom this PhD project would never have existed. I acknowledge the financial support of AWE.

Abstract

Steady state detonations of rate-stick explosives can be modelled via a streamline based approach. The Straight Streamline Approximation (SSA) is a method for predicting the shape of the shock front and sonic surface for an explosive rate-stick. The SSA model is implemented with different explosives models to verify its ability to accurately match high resolution Direct Numerical Simulations (DNS) beyond the simple polytropic EOS (equation of state) and power law reaction rate models. For explosive models using a reaction rate with an induction zone it shown that the SSA is unable to capture diameter effect curves when compared with DNS.

The CREST model is implemented into the ZND and Wood-Kirkwood steady-state detonation models. Implementing the CREST model into the steady-state models required the development of a thermodynamic relation not published before. Rate-stick calculations are performed for the SSA model and compared with DNS for various explosive models. With a realistic equation of state there is a limit on the boundary that the SSA model can integrate to, beyond this the streamlines begin to converge and the model equations break down. This places a limit on the SSA's modelling capabilities not previously reported.

Equations for the post-shock streamline curvature with a reaction term are developed. The streamline curvature is calculated for a polytropic EOS with and without reaction at the shock. It is shown that when reaction is a maximum at the shock the magnitude of the streamline curvature is reduced and, in some cases, changes the sign of the curvature. With no reaction at the shock the streamline curvature is significantly larger. Moreover DNS shows that the streamlines are more curved for reaction rates with induction zones when compared to simple power law reaction rates. The implications for the SSA's validity are discussed.

Contents

List of Figures

List of Tables

Abbreviations

CJ - Chapman Jouguet

D - Detonation velocity

D_{CJ} - Chapman Jouguet detonation velocity

ZND - Zeldovich-Von Neumann-Doering

SSA - Straight streamline approximation

DSD - Detonation shock dynamics

DNS - Direct numerical simulation

HLLC - Harten-Lax-Van Leer-contact

EOS - Equation of state

ISE - Isentropic solid equation

JWL - Jones-Wilkins-Lee

ANFO - Ammonium nitrate fuel oil

DDZ - Detonation driving zone

Chapter 1

Introduction

1.1 Detonation of Condensed Phase Explosives

A detonation wave is a combustion wave that propagates through explosive material at supersonic velocity. At the head of a detonation wave is a shock which causes a jump in the pressure, density and temperature of the explosive which initiate chemical reactions. The heat released by the chemical reaction supports the propagation of the shock wave. Behind the shock the reacting explosive produces expanding gases which can affect surroundings [1]. This thesis focuses on the detonation of a rate-stick which is a cylindrical charge of explosive material typically used in mining and military applications. A schematic of a rate-stick is shown in figure 1.1. The explosive is ignited at one end and a detonation wave is formed which propagates along the explosive.

Explosives can be categorised as either low or high depending upon the propagation velocity of the combustion wave [2]. Low explosives produce a deflagration wave that propagates at a subsonic velocity. An example of a low explosive is gunpowder. The energy transfer in deflagration waves is dominated by thermal diffusion processes.

High explosives produce a detonation wave that propagates at a supersonic velocity (up to $10kms^{-1}$). The energy transfer is dominated by compressive shock heating from the leading shock which, across a length scale of the order of a few nanometres, converts quiescent explosive to a supersonic, chemically reacting flow at temperatures of thousands of degrees kelvin [1]. An example of a high explosive is HMX with molecular formulae $C_4H_8N_4(NO_2)_4$. Due to the complex structure of the explosive the chemical decomposition follows a large number of reaction pathways, with intermediate species, to produce stable reaction products such as CO, H_2O, CO_2 and solid carbon (soot) [3].

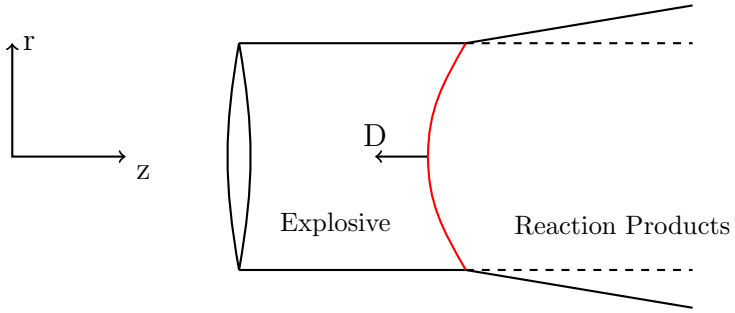

Figure 1.1: Schematic of rate-stick detonation. The shock wave (red line) is propagating from right to left at velocity D into a cylindrical stick of explosive. The flow behind the shock wave is expanding.

Typically, ignition of detonation waves in explosives is driven by imparting a shock wave upon the explosive with a detonator. The mechanism(s) by which the initial shock wave produces a detonation is determined by whether the explosive is homogeneous or heterogeneous. Homogeneous explosives (e.g. liquid and single crystal) have a uniform micro-structure (i.e. no voids or impurities) and a detonation wave is produced by thermal shock heating [4]. That is, the initial shock wave propagates through the explosive material and, after an induction stage, a thermal runaway occurs in the material that has been shocked the longest, producing a second shock wave that catches up

with the initial shock [5]. Heterogeneous explosives (e.g. cast, pressed, plastic bonded) have a non-uniform micro-structure due to the presence of defects (e.g. voids, pores and cracks) and exhibit different initiation behaviour to homogeneous explosives. The presence of defects is believed to produce localised hot spots, for example due to the collapse of a void. When the initial shock wave compresses the explosive, these hot spots induce chemical reactions which release further heat and drive the propagation of the initial shock[5]. Thus the shock initiation picture for heterogeneous explosives is that of an initial shock wave producing rapid heat release, with no significant induction stage, that initiates local chemical reactions that support the propagation of the shock wave. The rate of heat release is thus dependent upon both chemical (conversion of explosive to reaction products) and mechanical (hot spot) effects - this makes modelling the heat release of heterogeneous explosive difficult as there is presently no fundamental understanding of how the reaction and hot spot kinetics interact with each other or how they couple with the hydrodynamics [6].

It is possible for an explosive to undergo a Deflagration to Detonation Transition i.e. transitioning from a subsonic deflagration wave to a supersonic detonation wave [7]. This phenomena is observed experimentally and there is ongoing research into the underlying processes of the transition [8][9]. This thesis is not concerned with the DDT process.

A common method of characterising high explosives is by their detonation velocity (i.e. the velocity at which the shock wave propagates through the explosive). The detonation velocity for a rate-stick of explosive varies as a function of its radius (or size). A schematic of a typical size effect curves is shown in figure 1.2. For large radii there is an upper limit on the detonation velocity. As the charge radius is reduced the detonation velocity reduces until the explosive fails to detonate, this is indicated by the point F. This is the failure radius and shows that there is a minimum charge size required for

detonation to occur. Diameter effect curves can be used to calibrate numerical models of explosives. Other factors affecting the detonation velocity include the porosity of the unreacted explosive, the ambient temperature and explosive confinement. At small charge diameters, the detonation velocity has been shown to decrease as a function of ambient temperature [10].

High explosives can also be characterised as either ideal or non-ideal depending upon their reaction zone thickness. For ideal explosives the reaction zone thickness is small compared to the engineering scale (e.g. diameter of explosive) which means that geometrical effects do not have a strong effect on the propagation of the detonation wave. However, for non-ideal explosives the reaction zone thickness is much longer and the flow is more readily influenced by geometry and confinement effects. This difference manifests itself in the diameter effect curve as shown in figure 1.2, for small charge sizes there is a greater deficit in the detonation velocity for the non-ideal explosive compared to an ideal explosive. Release waves at the edge of the explosive are able to influence more of the shock front due to the thicker reaction zone, generating a more curved front and a reduced detonation velocity.

Confinement of an explosive enables detonation to occur at diameters below the critical diameter for an unconfined rate-stick. This is due to the confiner reducing the lateral expansion of the gaseous products, thus maintaining a higher pressure in the detonation reaction zone compared to the unconfined case [11].

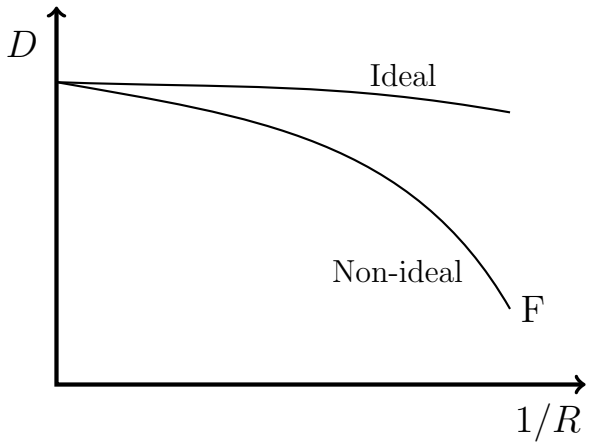

Figure 1.2: Schematic of size effect curves for ideal and non-ideal rate-stick explosives. The point F indicates the failure radius - below this the rate-stick fails to detonate.

1.2 Modelling

One of the primary motivations for detonation modelling arises from the high costs of performing real experiments. With a reliable explosive model, numerical simulations can be performed to provide an understanding and predictive capability of detonations in geometries more complex than that of a simple rate-stick, thus providing a valid alternative to high-cost experiments. It is important, however, that any numerical model should be validated against experimental data to give the modeller confidence in the predictive capabilities of the model.

Since detonation of heterogeneous explosives is complex, present day models are phenomenological and attempt to describe the burning of the explosive at the continuum level. At this length scale the Euler equations are assumed to provide an accurate description of the physics governing the flow. To model an individual explosive two additional equations are required: (i) An equation of state relating the specific inter-

nal energy to two other thermodynamic variables (e.g. pressure and density); (ii) An equation describing the chemical reaction progress (heat release) as the explosive reacts to form detonation products [12]. Equations of state are typically multiphase where each phase has its own separate equation of state. The phases are assumed to be in pressure (mechanical) equilibrium and propagate at the same velocity. Popular choices of equations of state include Jones-Wilkins-Lee (JWL), Williamsburg, polytropic and finite-strain. Apart from the polytropic EOS, these equations of state are empirical and must be calibrated to available experimental data. The equation(s) governing the chemical reaction rate are also empirical and are typically calibrated to ignition timing and size-effect data [13][14]. Reaction rate equations are typically related to the shock strength via a dependency upon one of the thermodynamic variables; pressure [15], temperature [1] and entropy [16] based models have been considered.

A method of solving the rate-stick problem is to solve the full time dependent Euler equations in a Direct Numerical Simulation (DNS) [17]. This method produces the most accurate numerical solutions as grid independent solutions of the full governing equations can be obtained, providing a complete picture of the detonation solution. However, this method is computationally expensive and can require the use of high-performance-computing facilities in order to complete calculations in a reasonable time frame. As a method of solving the rate-stick problem DNS calculations have only been feasible since the turn of the century.

As an alternative to performing full numerical calculations, simplified/reduced detonation models have been developed that dramatically reduce computational expense.

Solutions to the steady state detonation problem were first obtained by Chapman [18] and Jouguet [19], who considered the explosive to jump immediately to its fully reacted state immediately behind the shock, where the solution was obtained via the

use of the one-dimensional conservation equations. Zeldovich [20], Von-Neumann [21], and Doering [22] independently extended the Chapman-Jouguet model to incorporate a finite reaction zone behind the leading shock, this solution assumes that the flow is planar. Theoretical attempts to extend the theory beyond one-dimension have been attempted by Eyring [23], Jones [24] and Wood-Kirkwood [25]. Eyring's model was based upon the assumption that locally the detonation wave was spherical and the local detonation velocity could be related to the shock front curvature. The model of Jones was based upon a streamtube assumption where the detonation velocity was related to the expansion of the detonation products. The Wood-Kirkwood model was the first to consider the axisymmetric Euler equations, however the solution requires specifying an unknown radial divergence term and relating this to the shock front curvature [14] - this requires calibration to experimental data.

Further advancements in detonation modelling was borne from the work of Bdzil [26], from which Detonation Shock Dynamics (DSD) was developed [27]. It is based upon the assumption that the detonation velocity is asymptotically close to the CJ velocity and that the shock is weakly curved. Although valid for ideal explosives where the detonation velocity does not depart significantly from the CJ speed, DSD has been shown to significantly underpredict the detonation velocity for non-ideal explosives, where the detonation velocity can be as low as 50% of the CJ speed [28]. DSD models can be used to model the propagation of a detonation front in complex geometries [29].

A novel approach to solving the two-dimensional detonation problem was the Straight Streamline Approximation (SSA) model developed by Watt et al [30]. Here, no assumptions are made regarding the shock front curvature. The assumption in the model arises from the shape of the streamlines. The SSA was shown to be able to accurately match diameter effects curves when compared to high resolution DNS calculations for non-ideal explosives. However, they only considered the simple case of

a polytropic equation of state and simple power law reaction rate. It is yet to be seen whether the SSA model produces accurate results for different equations of state and reaction rate models.

1.3 Thesis Overview

The purpose of this thesis is to consider the SSA model with different equations of state and reaction rate forms to establish whether the SSA model can be used, in place of high resolution DNS calculations, to calculate unconfined diameter effect curves to be used as part of explosive model calibration.

First, an overview of relevant detonation theory and some basic models are presented. Next the CREST reactive burn model is implemented into the basic models and verified against DNS calculations. The Streamline detonation model is derived and implemented with different equations of state and reaction rate equations.

Chapter 2

Detonation Models

2.1 Introduction

This chapter introduces the governing equations used in detonation modelling and presents an overview of the ZND and WK reduced detonation models with solutions for a polytropic EOS with power law reaction rate.

2.2 Governing Equations

2.2.1 Reactive Euler Equations

The compressible Euler equations governing fluid flows are used to model detonations. As the flow is supersonic, hyperbolic terms dominate. To this end viscosity, thermal and mass diffusion terms can be neglected. The equations are

$$\frac{D\rho}{Dt} + \rho\nabla \cdot \boldsymbol{u} = 0, \tag{2.1}$$

$$\rho\frac{D\boldsymbol{u}}{Dt} + \nabla p = 0, \tag{2.2}$$

$$\frac{De}{Dt} - \frac{p}{\rho^2}\frac{D\rho}{Dt} = 0, \tag{2.3}$$

$$\frac{D\lambda}{Dt} = W, \tag{2.4}$$

where

$$\frac{D}{Dt} = \frac{\partial}{\partial t} + \boldsymbol{u} \cdot \nabla, \tag{2.5}$$

is the material derivative. These are equations for continuity, momentum, energy and the chemical reaction progress. Here ρ is density, $\mathbf{u}$ is the flow velocity, p is pressure, e is specific internal energy (i.e. per unit mass) and λ is the chemical reaction progress variable (ranging from 0 for no reaction to 1 for complete reaction). W is a function that describes the rate at which chemical reaction proceeds in the explosive and must be determined for a particular explosive; the function is typically dependent upon λ and local thermodynamic variables.

The reactive Euler equations can also be expressed in conservation form, in two-dimensions 2.1-2.4 become

$$\mathbf{U}_t + \mathbf{F}(\mathbf{U})_x + \mathbf{G}(\mathbf{U})_y = \mathbf{S}, \tag{2.6}$$

with

$$\mathbf{U} = \begin{bmatrix} \rho \\ \rho u \\ \rho v \\ E \\ \rho\lambda \end{bmatrix}, \quad \mathbf{F} = \begin{bmatrix} \rho u \\ \rho u^2 + p \\ \rho uv \\ u\left(E + p\right) \\ \rho u\lambda \end{bmatrix}, \quad \mathbf{G} = \begin{bmatrix} \rho v \\ \rho uv \\ \rho v^2 + p \\ v\left(E + p\right) \\ \rho v\lambda \end{bmatrix}, \quad \mathbf{S} = \begin{bmatrix} 0 \\ 0 \\ 0 \\ 0 \\ \rho W \end{bmatrix}. \tag{2.7}$$

These equations are for mass, x-momentum, y-momentum, energy and reaction progress variable respectively. The total energy E is given by a combination of the total internal

energy and kinetic energy

$$E = \rho\left(e + \frac{1}{2}\left(u^2 + v^2\right)\right). \tag{2.8}$$

An equation of state, relating the specific internal energy, e, of the explosive (reactants and products) to the thermodynamic variables, must be specified to close the reactive Euler equations. It is typically related to the local thermodynamic variables and the extent of reaction such that

$$e = e(p, \rho, \lambda). \tag{2.9}$$

2.3 ZND Model

Zeldovich [20], Von-Neumann [21], and Doering [22] independently developed the ZND model of detonation. The model assumes that the flow is laminar (one-dimensional) and, in a frame moving with the shock, steady state (i.e. time derivatives equal zero). The shock, propagating at a speed D, initiates an exothermic chemical reaction that supports the propagation of the front. Local thermodynamic equilibrium is assumed throughout the flow.

The flow equations are given by the one-dimensional conservation laws of continuity (mass), momentum and energy. It is convenient to transform from the laboratory frame to the shock-attached, steady state frame. We consider the velocity transform given by $u = U - D$ where u is the velocity in the shock-attached frame. The Euler equations are invariant under this velocity transformation. In this reference frame the unreacted explosive propagates into the stationary shock at velocity D.

The governing equations can be immediately obtained using the conservation form of the Euler equations. In one spatial dimension and using the steady state condition

equation 2.6 reduces to

$$\mathbf{F}(\mathbf{U})_x = \mathbf{S}, \tag{2.10}$$

which, when combined with 2.7-2.8 can be integrated with respect to the shock-attached coordinate to give

$$\rho u = \rho_0 D, \tag{2.11}$$

$$p + \rho u^2 = p_0 + \rho_0 D^2, \tag{2.12}$$

$$e + \frac{p}{\rho} + \frac{1}{2}u^2 = e_0 + \frac{p_0}{\rho_0} + \frac{1}{2}D^2. \tag{2.13}$$

These are equations in mass, momentum and energy. The terms with subscript 0 on the right-hand-side of these equations refer to the initial conditions of the explosive. The variation of the primitive variables can be obtained by integration of the reaction rate equation

$$\frac{d\lambda}{dx} = \frac{W}{u}, \tag{2.14}$$

which is coupled to the conservation equations via the equation of state. A useful insight into the ZND solution can be obtained by considering the solution in the $p - V$ plane. First eliminating u from equations 2.12 and 2.13 gives the equation for the Rayleigh line

$$R = \rho_0^2 D^2 - \frac{(p - p_0)}{(V_0 - V)} = 0, \tag{2.15}$$

where $V = 1/\rho$ is the specific volume. The Rayleigh line is a straight line in the (p, V) plane with slope $-\rho_0^2 D^2$ and represents conservation of momentum.

Eliminating u and D from equation 2.13 using 2.11 and 2.12 gives

$$H = e - e_0 - \frac{1}{2}(p + p_0)(V_0 - V) = 0. \tag{2.16}$$

This is the equation of the Hugoniot curve and represents conservation of energy. Figure 2.1 shows Hugoniot curves for the unburnt material ($H_{\lambda=0}$) and fully reacted material

($H_{\lambda=1}$) in the $p - V$ plane. Between these curves are partially reacted Hugoniots ($H_{partial}$). The solution proceeds from the post-shock state I, down a Rayleigh line, until the $H_{\lambda=1}$ curve is reached.

As the Rayleigh line is dependent upon D varying the magnitude of D will alter the final state solution. For $D = D_{CJ}$ (Rayleigh line R_{CJ}) there is a unique solution where the Rayleigh line and Hugoniot curve are tangent (labelled C). This is the minimum detonation velocity that satisfies the conservation equations and is called the Chapman-Jouguet (CJ) velocity. For a CJ detonation the fully reacted flow is exactly sonic, with respect to the shock. For $D > D_{CJ}$ (Rayleigh line R_{D_+}) there are two solutions, a strong (S) and weak (W) solution. The strong solution is subsonic in the shock- attached frame and the flow velocity remains subsonic when the reaction is complete. This solution is only possible if the detonation is supported at the rear boundary by, for example, a piston. It should be noted that for pathological detonations, in which endothermic chemical reactions are considered, there is a solution path from I to the weak point W [17]. However for strictly exothermic reactions (considered in this thesis) there is no solution path to the weak point [31]. For $D < D_{CJ}$ there is no intersection between the Rayleigh line and the fully reacted Hugoniot and thus no solution.

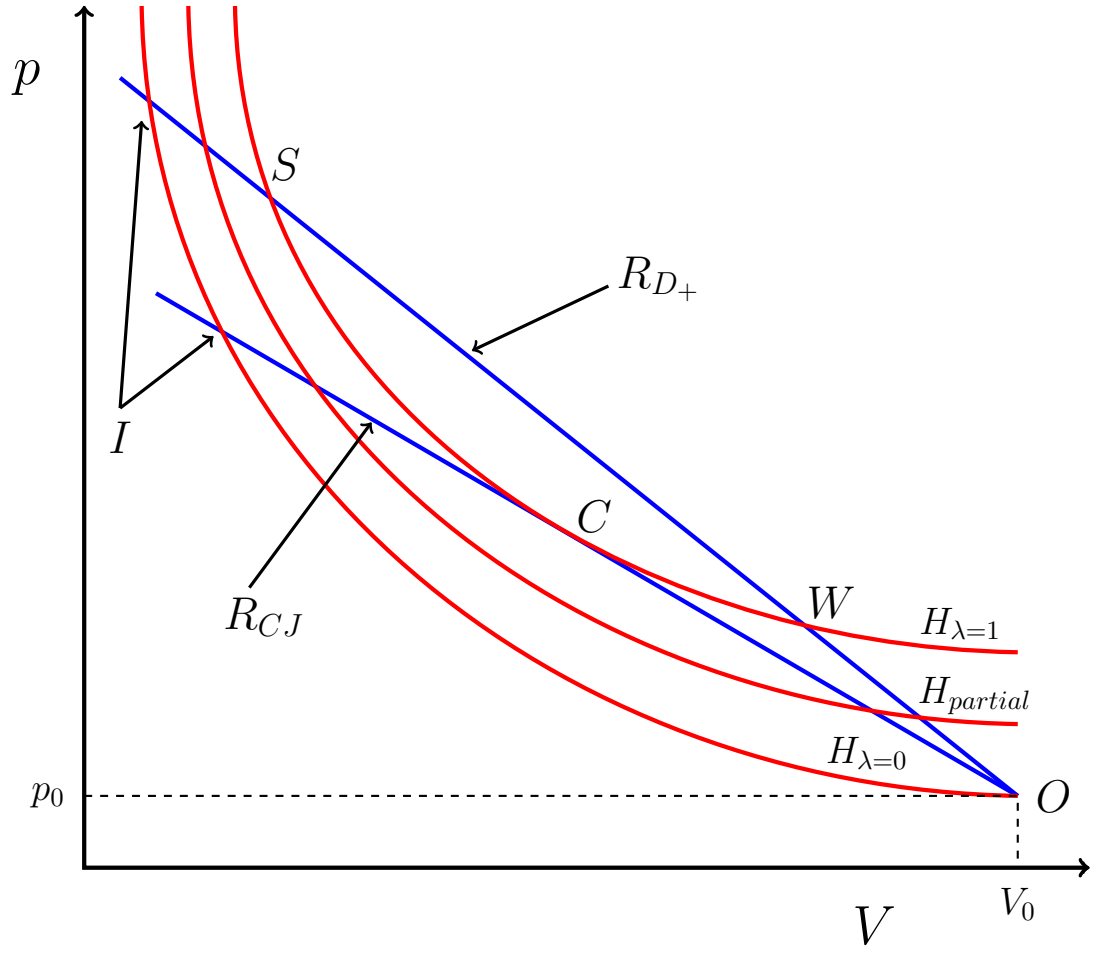

Figure 2.1: Hugoniot curves and Rayleigh lines for one-dimensional detonation in the $p-V$ plane. The Rayleigh lines are blue and are shown for the cases of $D > D_{CJ}$ (R_{D_+}) and $D = D_{CJ}$ (R_{CJ}). The Hugoniot curves are in red and are shown for the unreacted ($H_{\lambda=0}$), partial ($H_{partial}$) and the fully reacted state ($H_{\lambda=1}$). The post-shock states are indicated by I for a given Rayleigh line. The final solution point lies on the intersection between $H_{\lambda=1}$ and the Rayleigh line. Possible solutions are weak (W) and strong (S) for $D > D_{CJ}$; the Chapman-Jouguet solution (C) for $D = D_{CJ}$; there is no solution for $D < D_{CJ}$.

2.4 Wood-Kirkwood Model of Detonation

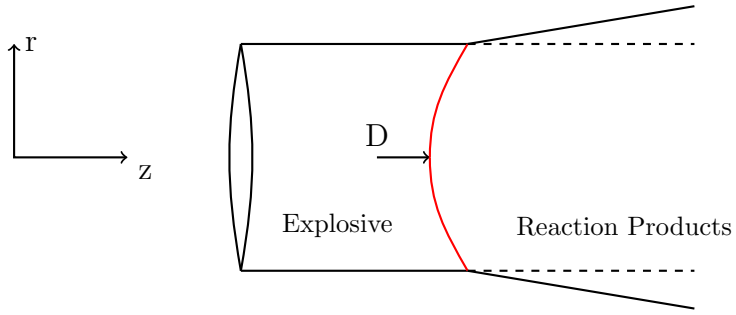

Figure 2.2: Schematic of rate-stick detonation in the shock attached frame. In this frame the quiescent explosive propagates from left to right (positive z direction) at velocity D into the stationary shock.

Wood and Kirkwood [25] considered the detonation of a rate-stick of condensed phase explosive as shown in 2.2. They developed a quasi-one dimensional theory, assuming that the flow was on axis ($r = 0$), that introduced divergence of the flow field behind the shock wave; the divergence of the flow is related to the curvature of the shock wave. It is intuitive to assume that there will be some expansion of the high pressure gases behind the shock front perpendicular to the flow direction. The divergence of the flow is analogous to a heat loss term and thus there will be less heat energy to support the detonation front. The detonation speed for a divergent flow will therefore be lower than D_{CJ}.

2.4.1 Flow Equations

The starting point for deriving the Wood-Kirkwood model is to consider the Euler equations for two-dimensional flow in axisymmetric geometry (r, z). The shock is assumed to be propagating at a steady velocity in the axial z direction only. The equations are

formulated in the rest frame of the shock. With these assumptions the reactive Euler equations 2.1-2.4 become

$$\omega\frac{\partial\rho}{\partial r}+u\frac{\partial\rho}{\partial z}+\rho\frac{\partial\omega}{\partial r}+\rho\frac{\partial u}{\partial z}+\rho\frac{\omega}{r}=0, \tag{2.17}$$

$$\rho\omega\frac{du}{dr}+\rho u\frac{\partial u}{\partial z}+\frac{\partial p}{\partial z}=0, \tag{2.18}$$

$$\rho\omega\frac{\partial\omega}{\partial r}+\rho u\frac{\partial\omega}{\partial z}+\frac{\partial p}{\partial r}=0, \tag{2.19}$$

$$\omega\frac{\partial e}{\partial r}+u\frac{\partial e}{\partial z}-\omega\frac{p}{\rho^2}\frac{\partial\rho}{\partial r}-u\frac{p}{\rho^2}\frac{\partial\rho}{\partial z}=0, \tag{2.20}$$

$$\omega\frac{\partial\lambda}{\partial r}+u\frac{\partial\lambda}{\partial z}=W. \tag{2.21}$$

Here z now represents the axial coordinate in the shock-attached frame, u is the axial flow velocity (in the shock attached frame) and ω is the radial flow velocity.

We specialize the equations to the axis, where $\omega = r = 0$ by symmetry. Within equation 2.17 the term $\rho\frac{\omega}{r}$ is singular at $r = 0$, we therefore consider the limit of this function as $r \to 0$ using L'Hôpital's rule such that

$$\lim_{r\to 0}\frac{\omega}{r}=\frac{(\frac{\partial\omega}{\partial r})}{(\frac{\partial r}{\partial r})}=\frac{\partial\omega}{\partial r}.$$

With this result and using the assumptions stated above 2.17-2.21 become

$$u\frac{\partial\rho}{\partial z}+\rho\frac{\partial u}{\partial z}=-2\rho\frac{\partial\omega}{\partial r}, \tag{2.22}$$

$$\rho u\frac{\partial u}{\partial z}+\frac{\partial p}{\partial z}=0, \tag{2.23}$$

$$\frac{\partial p}{\partial r}=0, \tag{2.24}$$

$$\frac{\partial e}{\partial z}-\frac{p}{\rho^2}\frac{\partial\rho}{\partial z}=0, \tag{2.25}$$

$$u\frac{\partial\lambda}{\partial z}=W. \tag{2.26}$$

If $\omega_r = 0$ then the equations are identical to those for planar flow. Equation 2.24 tells us that the pressure is constant in the radial direction. All of the remaining flow equations are in z only and thus can be written as total derivatives rather than partial derivatives. Due to the presence of the term on the RHS of the continuity equation 2.22 it is not possible to integrate it to get an algebraic equation for the mass flux. Equations 2.22-2.26 can be solved using numerical integration.

2.4.2 Master Equation in u

It is convenient to reduce the flow equations in ρ, u, p, e into a single differential equation in the flow velocity coupled to the rate law. This is done through successive substitutions of $\frac{d\rho}{dz}$ and $\frac{dp}{dz}$ in favour of $\frac{du}{dz}$ (here total derivative notation is now used).

To proceed we must specify the form of the equation of state, we will assume that there is a single phase and that the specific internal energy is a function of pressure, density and reaction variable, that is $e = e(p, \rho, \lambda)$. Substituting this into the energy equation 2.25 gives

$$\frac{de}{dz} = \left(\frac{\partial e}{\partial p}\right)_{\rho,\lambda} \frac{dp}{dz} + \left(\frac{\partial e}{\partial \rho}\right)_{p,\lambda} \frac{d\rho}{dz} + \left(\frac{\partial e}{\partial \lambda}\right)_{p,\rho} \frac{d\lambda}{dz} = \frac{p}{\rho^2}\frac{d\rho}{dz}.$$

Bringing terms in $\frac{d\rho}{dz}$ to the LHS and dividing by $\left(\frac{\partial e}{\partial p}\right)_{\rho,\lambda}$ gives

$$\left(\frac{p}{\rho^2} - \left(\frac{\partial e}{\partial \rho}\right)_{p,\lambda}\right)\left(\frac{\partial e}{\partial p}\right)_{\rho,\lambda}^{-1} \frac{d\rho}{dz} = \frac{dp}{dz} + \left(\frac{\partial e}{\partial \lambda}\right)_{p,\rho}\left(\frac{\partial e}{\partial p}\right)_{\rho,\lambda}^{-1} \frac{d\lambda}{dz}.$$

The term pre-multiplying $\frac{d\rho}{dz}$ is the square of the frozen sound speed (see appendix A) which gives

$$c^2 \frac{d\rho}{dz} = \frac{dp}{dz} + Q\frac{d\lambda}{dz}, \tag{2.27}$$

where Q is the thermicity parameter and, for an equation of state of the form $e = e(p, \rho, \lambda)$, is given by

$$Q = \left(\frac{\partial e}{\partial \lambda}\right)_{p,\rho} \left(\frac{\partial e}{\partial p}\right)^{-1}_{\rho,\lambda}. \tag{2.28}$$

Next we substitute for the pressure derivative using 2.23 and the density derivative using 2.22 into 2.27, which gives

$$-c^2 \left(\frac{\rho}{u}\frac{du}{dz} + \frac{2\rho}{u}\frac{d\omega}{dr}\right) = -\rho u \frac{du}{dz} + Q\frac{d\lambda}{dz}.$$

Rearranging for the velocity derivative gives

$$\frac{du}{dz} = \frac{\phi}{\eta} = \frac{2c^2\frac{d\omega}{dr} + \frac{Qu}{\rho}\frac{d\lambda}{dz}}{(u^2 - c^2)}. \tag{2.29}$$

This equation is coupled to the reaction rate equation

$$\frac{d\lambda}{dz} = \frac{W}{u}. \tag{2.30}$$

The derivatives in ρ, p, e can be written in terms of the velocity derivative to give

$$\frac{d\rho}{dz} = -\frac{\rho}{u}\frac{du}{dz}, \tag{2.31}$$

$$\frac{dp}{dz} = -\rho u \frac{du}{dz}, \tag{2.32}$$

$$\frac{de}{dz} = \frac{p}{\rho u}\frac{du}{dz}. \tag{2.33}$$

Equations 2.29-2.33 can be integrated to give the solution to the flow for a given divergence $\frac{d\omega}{dr}$. The initial conditions are given by the shock relations - solving the conservation equations of mass, momentum and energy across the shock 2.11-2.13 where the pre-shocked state of the explosive is known. The rear boundary condition is that the velocity u must be exactly sonic; the argument for this follows from the Chapman-Jouguet condition that requires the flow velocity go transonic in order for downstream

rarefactions to not affect (i.e. weaken) the shock wave. Equation 2.29 shows that when the flow speed is exactly sonic ($u = c$) $\eta = 0$ and the equation becomes singular. As we cannot have a singularity in the flow we require that ϕ becomes identically zero and so the rear boundary condition is the generalised CJ condition ($\phi = \eta = 0$). Due to the nonlinear coupling between the reaction rate and the divergence term $\frac{d\omega}{dr}$ the solution at each point in the flow cannot be determined via conservation equations. Thus a numerical scheme is required to integrate the flow equations. For a given form of $\frac{d\omega}{dr}$ there will be a unique, or eigenvalue, detonation speed that satisfies the general CJ conditions.

2.4.3 Expression for ω_r

An expression for ω_r can be derived by consideration of the continuity equation in spherical geometry. With r_L the radial coordinate in the laboratory frame and assuming spherical symmetry we have

$$\frac{\partial \rho}{\partial t} + \frac{\partial (\rho u_L)}{\partial r_L} = -\frac{2\rho u_L}{r_L}. \tag{2.34}$$

Here u_L is the radial velocity in the laboratory frame. We now transform to a reference frame moving at a constant velocity D such that at $t = 0$ $r_L = R_s$. If z is the distance in this frame, then it is related to r_L and t via

$$z = R_s + Dt - r_L.$$

Here $z = 0$ corresponds to $t = 0, r_L = R_s$. Next we transform the derivatives to the moving frame, using the velocity transform

$$u_L = D - u,$$

where u is the flow velocity in the shock-attached frame. The partial derivatives become

$$\left(\frac{\partial}{\partial t}\right)_{r_L} = \left(\frac{\partial}{\partial t}\right)_z + \left(\frac{\partial z}{\partial t}\right)_{r_L}\left(\frac{\partial}{\partial z}\right)_t, = \left(\frac{\partial}{\partial t}\right)_z + D\left(\frac{\partial}{\partial z}\right)_t,$$

and

$$\left(\frac{\partial}{\partial r_L}\right)_t = -\left(\frac{\partial}{\partial z}\right)_t.$$

Application of these transformation equations to 2.34 gives

$$\frac{\partial \rho}{\partial t} + \frac{\partial (\rho u)}{\partial z} = -\frac{2\rho(D-u)}{R_s + Dt - z}.$$

For steady state flow the time derivative can be dropped and assuming that $R_s >> z$ and small t we have

$$\frac{\partial (\rho u)}{\partial z} = -\frac{2\rho(D-u)}{R_s}. \tag{2.35}$$

Comparing 2.35 with 2.22 gives

$$\frac{d\omega}{dr} = \frac{D-u}{R_s}, \tag{2.36}$$

where R_s is the radius of curvature of the shock front.

2.4.4 Equation of state and reaction rate

With the flow equations specified, the equation of state and chemical reaction model must be specified. The polytropic EOS was used, it is given by

$$e = \frac{p}{(\gamma - 1)\rho} - \lambda q. \tag{2.37}$$

Here q is the detonation specific energy and represents the net chemical energy available for the explosive. The reaction rate equation is

$$W = \alpha (1-\lambda)^m p^n. \tag{2.38}$$

Here α is a rate-constant, m and n are dimensionless constants. For fixed values of m and n, the magnitude of α is chosen such that $\lambda = \frac{1}{2}$ when $z = \frac{1}{2}$ in the ZND detonation model.

The problem is non-dimensionalised by setting the initial density $\rho_0 = 1$ and the detonation speed $D_{CJ} = 1$. Then all flow variables are scaled to these. With the equation of state specified the shock relations can be used to give the initial conditions for the numerical integration. Applying the strong shock assumption ($p_0 = 0$) to the equations for conservation of mass, momentum and energy to give the post-shock conditions

$$u = -\frac{\gamma - 1}{\gamma + 1} D \ , \ \rho = \frac{\gamma + 1}{\gamma - 1} \ , \ p = \frac{2}{\gamma + 1} D^2. \tag{2.39}$$

In addition - for the polytropic equation of state - the detonation specific energy is given by

$$q = \frac{1}{2(\gamma^2 - 1)}. \tag{2.40}$$

$\gamma = 3$ is typically used for modelling condensed phase explosives [1].

2.4.5 Shooting Method

With the equation of state and reaction rate model specified there are two free parameters - the shock curvature R_s and the detonation speed D. If the detonation velocity is specified the flow equations 2.29-2.33 form an eigenvalue problem in the shock curvature. There will be a unique value of the shock curvature R_S for which the rear boundary conditions, as described above, are satisfied. The numerical shooting method is used to obtain the shock curvature for a given detonation velocity. The procedure is to make a guess for R_s and integrate the flow equations (with the shock relations giving the initial conditions) until one of the generalised CJ conditions are satisfied ($\phi = 0$ or $\eta = 0$). The detonation velocity is varied, and the flow equations integrated from the

shock, until both $\phi = \eta = 0$ are obtained simultaneously or R_s has converged up to an arbitrary precision. A bisection method was used to iterate on the detonation velocity.

2.4.6 Calculations

The relationship between the detonation velocity and the shock curvature was investigated. The relationship was determined for different values of the rate parameter n.

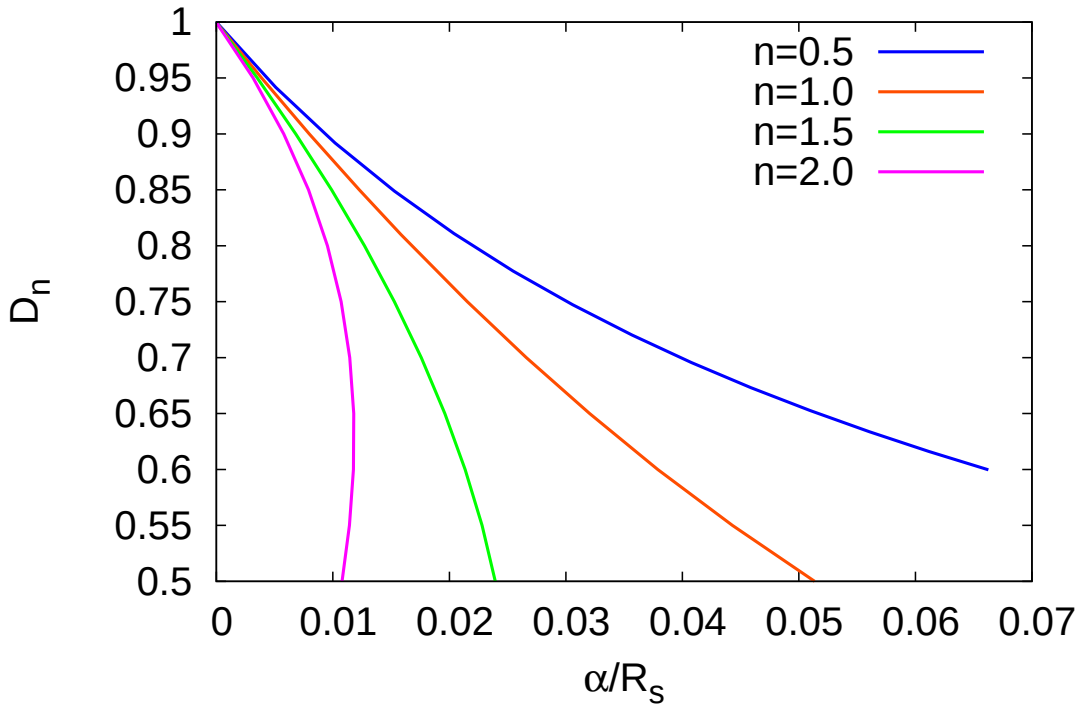

Figure 2.3: Normal detonation velocity as a function of shock front curvature with different values of the rate parameter n, $m = \frac{1}{2}$ was used for all cases.

Figure 2.3 shows that increasing the shock curvature reduces the normal prop-

agation velocity for $n <= 1.5$. The presence of the curvature term in the continuity equation is analogous to that of a heat loss term along the normal flow direction. One therefore expects the expansion of the flow to reduce the propagation velocity of the detonation front. For $n > 1.5$ there is always a turning point in the curve and the solution can be multivalued, as was first shown by Cowperthwaite [32]. This is evident in figure 2.3 for $n = 2$ where there is a turning point in the curve at $D \sim 0.65$, this is called the extinction/failure point of the solution. For detonation speeds lower than this the solution is unstable [33] and thus one would always consider the larger velocity solution for a given value of $\frac{\alpha}{R_s}$. The extinction point represents a lower limit on the steady state propagation velocity based upon the shock curvature. If one could relate the shock front curvature to the diameter of the charge, then one could obtain a lower limit on the diameter of a charge in which a detonation could propagate.

Downstream of the sonic locus the flow continues to react and expand. To integrate the solution beyond the sonic locus one can linearise the flow equations at the point $u = c$, calculate the eigenvalues and eigenvectors, and determine the solution trajectory beyond the singular point. It can be shown that the sonic locus is a saddle point in the (u, λ) plane.

There are no analytical models for relating the rate-stick diameter to the shock front curvature for the Wood-Kirkwood model. Empirical models, based upon experimental data, are used to attempt to calibrate mathematical relationships between curvature and charge size [34]. With this one can relate the detonation velocity to size of the explosive [14] to obtain diameter effect curves. This method of obtaining diameter effect curves will not be considered in this thesis.

One-dimensional calculations (with $\omega_r = 0$) were performed to investigate the sensitivity of the flow structure to the detonation velocity. Figure 2.4 shows Mach number ($M = u/c$) as a function of the reaction progress variable for different deto-

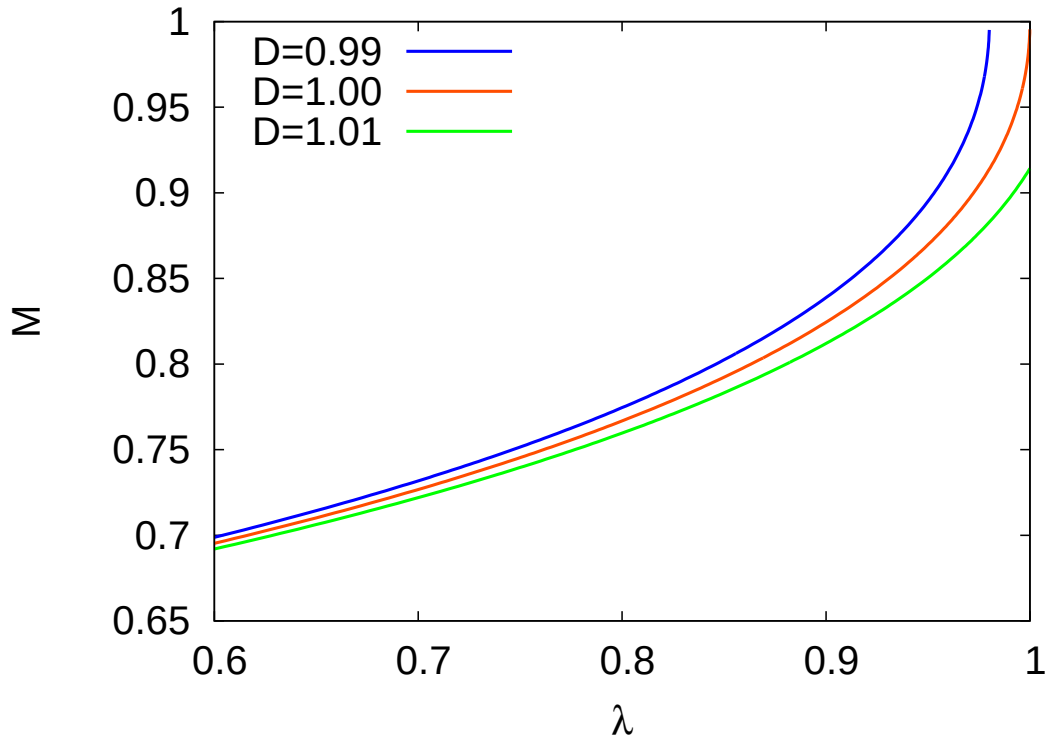

Figure 2.4: Mach number as a function of reaction progress variable for a one-dimensional detonation with reaction rate parameters $m = \frac{1}{2}$ and $n = 0$. Solutions for different D are indicated by the key.

nations speeds. For $D = 0.99$ it is the clear that the flow goes supersonic before the reaction is complete. For $D = 1.01$ the flow remains subsonic when the reaction completes. For $D = 1.00$ the flow goes exactly sonic when the reaction completes. It is clear that the solution is very sensitive to the value of D. This is evidence of the saddle point behaviour in the (u, λ) plane and shows that to obtain a correct solution to the eigenvalue problems requires a precise value of D.

Chapter 3

CREST Reactive Burn Model

3.1 Introduction

CREST is a reactive burn model for condensed phase explosives comprising of a two-phase equation of state and an entropy dependent reaction rate. The use of an entropy based reaction rate is unique to this model when compared with other commonly used reactive burn models which have reaction rates depending on the pressure or temperature [14][15][26][35]. When modelling detonation of a rate-stick with CREST, the reaction rate is dependent upon the entropy of the shocked, unreacted, explosive. The entropy remains constant throughout the reaction zone.

CREST has been shown to accurately reproduce the run-time to detonation and diameter effect curves [36]. Previously published work [16][36][37][38] has seen CREST implemented into DNS calculations. However, the model has not been implemented into any steady state detonation models such as the Wood-Kirkwood model or DSD. In the following sections an overview of the CREST reactive burn model is given; the model is implemented into the steady one-dimensional and Wood-Kirkwood detonation

models.

3.2 Details of CREST

The equation of state is a two-phase model consisting of an unreacted (solid) phase and fully reacted (gaseous) phase and mechanical (pressure) equilibrium between the two phases is assumed. Simple mixture laws are used to determine the overall thermodynamic variables at any given time. The reaction rate model comprises of a 'fast' reaction term and a 'slow' reaction term that contribute to a global reaction rate for the explosive. The global reaction is one-way and the specific detonation energy is released implicitly via the transition from the solid phase to the gaseous phase.

3.2.1 Equation of State

The solid and gas phase equations of state can be written in the form $e_k = e_k(p_k, \rho_k)$ where the k subscript denotes the phase of explosive, s will be used for the solid and g for the gas phase.

The equation of state for the solid phase [36] is

$$e_s = e_i(\rho_s) + \frac{p_s - p_i(\rho_s)}{\rho_s \Gamma(\rho_s)}, \tag{3.1}$$

where

$$
\begin{aligned}
p_i(\rho_s) &= 3K_{0s} f (2f+1)^{5/2} \left(F + \frac{f}{2}\frac{dF}{df} \right), \\
e_i(\rho_s) &= \frac{9}{2}\frac{K_{0s}}{\rho_{0s}} f^2 F + E_d, \\
f &= \frac{1}{2}\left[\left(\frac{\rho_s}{\rho_{0s}} \right)^{2/3} - 1 \right], \\
F &= \exp\left[g(f) \right], \\
g(f) &= g_A + g_B + g_C, \\
g_A &= A_1 f + A_2 f^2 + A_3 f^3 \\
&\quad + \left[B_1 (f - f_c) + B_2 (f - f_c)^2 + B_3 (f - f_c)^3 \right] \frac{1}{2}\left[1 - \frac{2}{\pi}\tan^{-1}\left(\frac{(f - f_c)}{\delta} \right) \right], \\
g_B &= \frac{\delta}{2\pi}\left(B_1 - \delta^2 B_3 \right) \ln\left[\delta^2 + (f - f_c)^2 \right] - \frac{B_2 \delta^2}{\pi}\tan^{-1}\left(\frac{(f - f_c)}{\delta} \right) \\
&\quad + \frac{\delta}{2\pi}(f - f_c)\left[2B_2 + B_3 (f - f_c) \right], \\
g_C &= \left[B_1 f_c - B_2 f_c^2 + B_3 f_c^3 \right] \frac{1}{2}\left[1 - \frac{2}{\pi}\tan^{-1}\left(\frac{-f_c}{\delta} \right) \right] \\
&\quad - \frac{\delta}{2\pi}\left(B_1 - \delta^2 B_3 \right) \ln\left[\delta^2 + f_c^2 \right] + \frac{B_2 \delta^2}{\pi}\tan^{-1}\left(\frac{-f_c}{\delta} \right) \\
&\quad + \frac{\delta}{2\pi} f_c (2B_2 - B_3 f_c), \\
\Gamma(\rho_s) &= \gamma_{00} + \Gamma_1 \left(\frac{\rho_{0s}}{\rho_s} \right)^m \exp\left[-\Gamma_2 \left(\frac{\rho_{0s}}{\rho_s} \right) \right]
\end{aligned}
\tag{3.2}
$$

Here $p_i(\rho_s)$ and $e_i(\rho_s)$ are the equations for the pressure and internal energy on the principal isentrope that have been fitted to experimental data, $\Gamma(\rho_s)$ is the Grüneisen gamma, f is the finite strain variable that describes compression of the solid, E_d is the specific detonation energy of the explosive, K_{0s} and ρ_{0s} are the bulk modulus and solid density of the unreacted explosive at theoretical maximum density in standard conditions, and A_1, A_2, A_3, B_1, B_2, B_3, f_c, δ, m, γ_{00}, Γ_1, and Γ_2 are constants.

The gas phase is modelled by a Jones-Wilkins-Lee (JWL) equation of state [2] given by

$$e_g = \frac{p_g}{\rho_g w} + A\left(\frac{1}{R_1\rho_{0s}} - 1\right)\exp\left(-R_1\frac{\rho_{0s}}{\rho_g}\right) + B\left(\frac{1}{R_2\rho_{0s}} - 1\right)\exp\left(-R_2\frac{\rho_{0s}}{\rho_g}\right), \quad (3.3)$$

where A, B, R_1, R_2, and w are constants.

3.2.2 Reaction Rate

The reaction rate equation [16] comprises of a slow reaction rate coupled to a fast reaction. The fast reaction attempts to model the initial high reaction rate produced by 'hot-spots' immediately behind the shock. The slow reaction, which is coupled to the first, models the overall bulk burn of the explosive. The reaction rate equations are given by

$$\frac{d\lambda}{dt} = m_1\frac{d\lambda_1}{dt} + m_2\frac{d\lambda_2}{dt}, \quad (3.4)$$

$$\frac{d\lambda_1}{dt} = (1-\lambda_1)\left[-2b_1\ln(1-\lambda_1)\right]^{\frac{1}{2}}, \quad (3.5)$$

$$\frac{d\lambda_2}{dt} = (1-\lambda_2)\lambda_1\left[2b_2\left(\frac{b_2\lambda_1}{b_1} - \ln(1-\lambda_2)\right)\right]^{\frac{1}{2}}, \quad (3.6)$$

where

$$b_1 = c_0(Z_s)^{c_1}\ ,\ b_2 = c_2(Z_s)^{c_3}, \quad (3.7)$$

and

$$m_1 = (1-\lambda)\frac{c_6(Z_s)^{c_{12}}}{\sqrt{b_1}}\ ,\ m_2 = (1-\lambda)\left[\frac{c_8(Z_s)^{-c_9} + c_{10}(Z_s - c_{13})^{c_{11}}}{\sqrt{b_1}}\right]. \quad (3.8)$$

Here c_0 through c_{13} are constants. Z_S is a function of the solid phase entropy and is given by

$$Z_s = \frac{e_s(v_s) - e_i(v_s)}{\tau(v_s)}, \quad (3.9)$$

where $\tau(v_s)$ is related to the Grüneisen Γ by

$$\tau(v_s) = \exp\left(-\int_{v_{0s}}^{v_s} \frac{\Gamma}{v_s} dv_s\right). \tag{3.10}$$

This expression is derived by integrating the first law of thermodynamics with the solid equation of state; see appendix B for details of the derivation.

3.2.3 Mixing Model

The Isentropic Solid Equation (ISE) model is used to determine the equation of state of the reacting mixture [39]. The model assumes that pressure equilibrium is maintained throughout the reaction zone between the solid explosive and gaseous detonation products. Simple mixture laws relating to the total density and specific internal energy to the solid and gas phase are used. To close the equations the solid phase is assumed to be on an isentrope such that the first law of thermodynamics for an adiabatic process can be invoked.

The equations are

$$de_s = \frac{p}{\rho_s^2} d\rho_s, \tag{3.11}$$

$$\frac{1}{\rho} = \frac{(1-\lambda)}{\rho_s} + \frac{\lambda}{\rho_g}, \tag{3.12}$$

$$e = (1-\lambda)e_s + \lambda e_g, \tag{3.13}$$

$$p_s - p_g = 0, \tag{3.14}$$

where λ describes the total progress of the chemical reaction between the solid and gas phase (0 for no reaction and 1 for complete).

3.2.4 Frozen Sound Speed in a two-phase system

To determine the frozen sound speed of a multi-phase system we consider the mixture equation for density 3.12, as the pressure is the same for the solid and gas phase we can take the partial derivative with respect to pressure giving

$$\frac{1}{\rho^2}\left(\frac{\partial \rho}{\partial p}\right)_\lambda = \frac{1-\lambda}{\rho_s^2}\left(\frac{\partial \rho_s}{\partial p}\right)_\lambda + \frac{\lambda}{\rho_g^2}\left(\frac{\partial \rho_g}{\partial p}\right)_\lambda .$$

Noting that $c^2 = \frac{\partial p}{\partial \rho}$ is the square of the sound speed we can write

$$\frac{1}{\rho^2 c^2} = \frac{1-\lambda}{\rho_s^2 c_s^2} + \frac{\lambda}{\rho_g^2 c_g^2}, \tag{3.15}$$

where c_s and c_g are the sound speeds of the solid and gas phases respectively. The general form for the sound speed is derived in appendix A and is

$$c_k^2 = \left(\frac{p}{\rho_k^2} - \left(\frac{\partial e_k}{\partial \rho_k}\right)_p\right) \Big/ \left(\frac{\partial e_k}{\partial p}\right)_{\rho_k}, \tag{3.16}$$

where k indicates the phase of the explosive.

3.2.5 Explosive models

In this thesis the CREST model is applied to two explosives - EDC37 and PBX9502. The parameters are taken directly from previously published work [36] and are reproduced here for completeness. The equation of state and reaction rate parameters for each explosive are summarised in table 3.1.

Parameter	EDC37	PBX9502	Units
ρ_0	1.8445	1.890	g/cm^3
ρ_{0s}	1.8445	1.942	g/cm^3
A	6.642021	4.603	$Mbar$
B	0.2282927	0.09544	$Mbar$
R_1	4.25	3.903	
R_2	1.825	1.659	
ω	0.25	0.48	
E_d	0.0719557	0.0373	$Mbar\,cm^3/g$
K_{0s}	0.1424525	0.090314021	$Mbar$
A_1	2.417494	0.246257	
A_2	2.208027	11.44221	
A_3	0.0	0.0	
B_1	0.0	16.8477	
B_2	0.0	6.534913	
B_3	0.0	0.0	
f_s	0.0	0.05	
δ	0.0	0.021322	
Γ_1	32.33557	126.4052	
Γ_2	3.596933	6.554447	
γ_{00}	0.4	0.4	
m	2.0	2.0	
c_0	2.0×10^8	2.0×10^7	$\mu s^{-2}(Mbar\,cm^3/g)^{-c_1}$
c_1	2.0	2.5	
c_2	2.2×10^8	8.0×10^6	$\mu s^{-2}(Mbar\,cm^3/g)^{-c_3}$
c_3	2.5	2.5	
c_6	0.0	1.8×10^{12}	μs^{-1}
c_8	1.6×10^{-4}	0.0	$\mu s^{-1}(Mbar\,cm^3/g)^{c_9}$
c_9	1.0	1.0	
c_{10}	4.0×10^5	3.0×10^{13}	$\mu s^{-1}(Mbar\,cm^3/g)^{-c_{11}}$
c_{11}	1.8	1.25	
c_{12}	0.0	5.0	
c_{13}	0.0	0.0012	$Mbar\,cm^3/g$

Table 3.1: Equation of state and reaction rate parameters for CREST reactive burn models EDC37 and PBX9502.

3.3 CREST in Wood-Kirkwood Model

In section 2.4 the differential equations for the Wood-Kirkwood model were derived for a single phase equation of state. As CREST uses a multiphase equation of state additional steps are required to determine an expression relating the thermodynamic variables to the chemical reaction rate. The procedure is very similar and the resulting equations are of a similar form.

3.3.1 Differential Energy Equation

We begin by considering the specific internal energy of the individual phases. The solid phase is assumed to be on a isentrope and thus, from 3.11

$$de_s = \frac{p}{\rho_s^2} d\rho_s = \frac{p}{\rho_s^2 c_s^2} dp, \tag{3.17}$$

where we have used the relation $c_s^2 = \frac{\partial p}{\partial \rho_s}$. For the gas phase we make no assumptions about the thermodynamics and expand the specific internal energy in terms of p and ρ_g. With $e_g(p, \rho_g)$ we have

$$de_g = \left(\frac{\partial e_g}{\partial p}\right) dp + \left(\frac{\partial e_g}{\partial \rho_g}\right) d\rho_g. \tag{3.18}$$

To derive an expression relating the global thermodynamic variables we take the differential form of the internal energy mixture equation 3.13,

$$de = (1 - \lambda)\, de_s + \lambda de_g + (e_g - e_s)\, d\lambda.$$

Substituting for de_s with 3.17 and de_g with 3.18

$$de = \frac{(1-\lambda)}{\rho_s^2 c_s^2} p\, dp + \lambda \left[\left(\frac{\partial e_g}{\partial p}\right) dp + \left(\frac{\partial e_g}{\partial \rho_g}\right) d\rho_g \right] + (e_g - e_s)\, d\lambda. \tag{3.19}$$

To find an expression for $d\rho_g$ we consider the differential form of 3.12

$$-\frac{1}{\rho^2}d\rho = -\frac{(1-\lambda)}{\rho_s^2}d\rho_s - \frac{\lambda}{\rho_g^2}d\rho_g + \left(\frac{1}{\rho_g} - \frac{1}{\rho_s}\right)d\lambda.$$

Substituting for $d\rho_s$ using 3.17 and rearranging for $d\rho_g$

$$d\rho_g = \frac{\rho_g^2}{\lambda}\left[\frac{d\rho}{\rho^2} - \frac{(1-\lambda)}{\rho_s^2 c_s^2}dp + \left(\frac{1}{\rho_g} - \frac{1}{\rho_s}\right)d\lambda\right].$$

Substituting this expression into 3.19 and using the first law of thermodynamics, equation 2.3, to substitute for de

$$\begin{aligned}\frac{p}{\rho^2}d\rho =& \frac{(1-\lambda)}{\rho_s^2 c_s^2}p\,dp + \lambda\left(\frac{\partial e_g}{\partial p}\right)dp + (e_g - e_s)\,d\lambda \\ &+ \rho_g^2\left(\frac{\partial e_g}{\partial \rho_g}\right)\left[\frac{d\rho}{\rho^2} - \frac{(1-\lambda)}{\rho_s^2 c_s^2}dp + \left(\frac{1}{\rho_g} - \frac{1}{\rho_s}\right)d\lambda\right].\end{aligned}$$

Grouping terms multiplying derivatives in ρ, p, λ

$$\begin{aligned}\left(p - \rho_g^2\left(\frac{\partial e_g}{\partial \rho_g}\right)\right)\frac{d\rho}{\rho^2} =& \left[\left(p - \rho_g^2\left(\frac{\partial e_g}{\partial \rho_g}\right)\right)\frac{(1-\lambda)}{\rho_s^2 c_s^2} + \lambda\left(\frac{\partial e_g}{\partial p}\right)\right]dp \\ &+ \left[\rho_g^2\left(\frac{\partial e_g}{\partial \rho_g}\right)\left(\frac{1}{\rho_g} - \frac{1}{\rho_s}\right) + (e_g - e_s)\right]d\lambda. \qquad (3.20)\end{aligned}$$

The sound speed squared of the gas can be written

$$c_g^2 = \left(\frac{p}{\rho_g^2} - \left(\frac{\partial e_g}{\partial \rho_g}\right)\right) \Bigg/ \left(\frac{\partial e_g}{\partial p}\right).$$

Rearranging this expression gives

$$p - \rho_g^2\left(\frac{\partial e_g}{\partial \rho_g}\right) = \rho_g^2 c_g^2\left(\frac{\partial e_g}{\partial p}\right).$$

Substituting this into the left-hand-side of 3.20

$$\begin{aligned}\rho_g^2 c_g^2\left(\frac{\partial e_g}{\partial p}\right)\frac{d\rho}{\rho^2} =& \left[\rho_g^2 c_g^2\left(\frac{\partial e_g}{\partial p}\right)\frac{(1-\lambda)}{\rho_s^2 c_s^2} + \lambda\left(\frac{\partial e_g}{\partial p}\right)\right]dp \\ &+ \left[\rho_g^2\left(\frac{\partial e_g}{\partial \rho_g}\right)\left(\frac{1}{\rho_g} - \frac{1}{\rho_s}\right) + (e_g - e_s)\right]d\lambda,\end{aligned}$$

multiplying this expression by $\rho^2/\rho_g^2 c_g^2 \left(\frac{\partial e_g}{\partial p}\right)$

$$d\rho = \rho^2 \left[\frac{(1-\lambda)}{\rho_s^2 c_s^2} + \frac{\lambda}{\rho_g^2 c_g^2}\right] dp + \frac{\rho^2}{\rho_g^2 c_g^2 \left(\frac{\partial e_g}{\partial p}\right)} \left[\rho_g^2 \left(\frac{\partial e_g}{\partial \rho_g}\right) \left(\frac{1}{\rho_g} - \frac{1}{\rho_s}\right) + (e_g - e_s)\right] d\lambda.$$

By 3.15, the term in the first set of square braces is $\frac{1}{\rho^2 c^2}$, using this result and multiplying by c^2

$$c^2 d\rho = dp + Q\, d\lambda, \tag{3.21}$$

where

$$Q = \frac{\rho^2 c^2}{\rho_g^2 c_g^2 \left(\frac{\partial e_g}{\partial p}\right)} \left[\rho_g^2 \left(\frac{\partial e_g}{\partial \rho_g}\right) \left(\frac{1}{\rho_g} - \frac{1}{\rho_s}\right) + (e_g - e_s)\right]. \tag{3.22}$$

Here Q is the thermicity parameter for CREST. Equation 3.21 is simply a consequence of the first law of thermodynamics and is independent of the remaining flow equations and geometry of the problem.

3.3.2 Master Equation

We are now in a position to reduce the system of equations into a master equation in the flow velocity u. A similar procedure to that of section 2.4.2, for the single phase equation of state, is followed.

Substituting for the density derivative using 2.22 and the pressure derivative using 2.23 into the differential energy equation 3.21 we have

$$-c^2 \frac{\rho}{u} \frac{du}{dz} - 2c^2 \frac{\rho}{u} \frac{d\omega}{dr} = -\rho u \frac{du}{dz} + Q \frac{d\lambda}{dz}.$$

Solving for the velocity derivative gives

$$\frac{du}{dz} = \frac{2c^2 \frac{d\omega}{dr} + \frac{Qu}{\rho} \frac{d\lambda}{dz}}{u^2 - c^2}. \tag{3.23}$$

This is the master equation in the flow velocity, u, which is coupled directly to the reaction rate equation 3.4. Differential equations for the other flow variables are coupled to the velocity equation via

$$\frac{d\rho}{dz} = \frac{\rho}{u}\frac{du}{dz}\ ,\ \frac{dp}{dz} = -\rho u\frac{du}{dz}\ ,\ \frac{d\rho_s}{dz} = -\frac{\rho u}{c_s^2}\frac{du}{dz}\ ,\ \frac{de}{dz} = \frac{pu}{\rho}\frac{du}{dz}. \tag{3.24}$$

For the remaining flow variables, e_s can be calculated from the equation of state 3.1. Then e_g and ρ_g can be calculated using the mixture equations 3.12 and 3.13.

The flow equations for the CREST Wood-Kirkwood model must be solved between the post-shock state and the generalised CJ condition. The generalised CJ conditions require that the numerator and denominator of the RHS of 3.23 be identically zero i.e.

$$2c^2\frac{d\omega}{dr} + \frac{Qu}{\rho}\frac{d\lambda}{dz} = 0, \quad u^2 = c^2. \tag{3.25}$$

For a given detonation velocity D there will be a unique value of $\frac{d\omega}{dr}$ that will satisfy 3.25 identically, which must be found as part of the solution process.

3.3.3 Shock Relations

In the shock-attached frame the pre-shocked explosive has density ρ_0, detonation specific energy E_d and velocity D. It is assumed that the explosive is non-reacting as it is shocked ($\lambda = 0$). Although in practice some reaction may be expected to occur through the shock this assumption is necessary to ensure a unique post-shock state. As the solid phase equation of state is non-linear in ρ_s analytical solutions to the shock relations are not readily possible: it must thus be determined numerically. The procedure for solving the shock relations is now outlined.

We first consider the equations for conservation of mass, momentum and energy.

$$\rho_s u_s = \rho_0 D, \tag{3.26}$$

$$p_s + \rho_s u_s^2 = p_0 + \rho_0 D^2, \tag{3.27}$$

$$e_s(\rho_s, p_s) + \frac{p_s}{\rho_s} + \frac{1}{2}u_s^2 = e_s(\rho_0, p_0) + \frac{p_0}{\rho_0} + \frac{1}{2}D^2, \tag{3.28}$$

Equations 3.26 and 3.27 can be used to eliminate u_s and ρ_s in turn to give

$$\rho_s = \frac{\rho_0^2 D^2}{\rho_0 D^2 + p_s - p_0}, \tag{3.29}$$

and

$$u_s = \frac{\rho_0 D^2 + p_s - p_0}{\rho_0 D}. \tag{3.30}$$

Substituting equations 3.29 and 3.30 into the energy equation 3.28 leaves only p_s to be determined. A secant routine was used to iterate on p_s, terminating when the error post-shock pressure was less than $10^{-6} Mbar$.

3.3.4 Modelling Details

An explicit fourth-order Runge-Kutta scheme was used to integrate the flow equations between the shock and CJ condition.

Immediately behind the shock the explosive is unreacted and the thermodynamic term in the master equation 3.23 $Q = 0$. The mixture of solid and gas is initialised when λ first becomes greater than a small parameter ϵ. For $\lambda > \epsilon$ the mixture equations are used and the flow variables are updated using the differential equations 3.24. For these simulations $\epsilon = 10^{-2}$ was used. The small parameter ϵ was chosen to match the value used in the DNS calculations.

At the point of initial mixing we evaluate the mass, momentum and energy which gives

$$\rho u = \rho_n u_n = M_1, \tag{3.31}$$

$$p + \rho u^2 = p_n + \rho_n u_n^2 = \Pi_1, \tag{3.32}$$

$$e + \frac{p}{\rho} + \frac{1}{2}u^2 = E_0. \tag{3.33}$$

Here M_1 and Π_1 will not be the same as the initial mass and momentum flux due to the presence of the divergent flow term, u_n and ρ_n are the current flow velocity and density. The total energy E_0 is conserved along the flow and is given by the RHS of equation 3.28 from the shock relations. Introducing the reaction term releases some detonation energy into the system, it is therefore necessary to adjust the flow variables to introduce this energy. To determine the mixed state the solid phase density is varied until the conservation equations 3.31-3.33 and the CREST mixture equations 3.12-3.14 are satisfied.

The procedure is outlined below. An initial guess is made for the new solid density, ρ_s^{n+1}, using the isentropic expansion of the solid 3.11 we obtain the solid specific internal energy

$$e_s^{n+1} = e_s^n - p^n \left(\frac{1}{\rho_s^{n+1}} - \frac{1}{\rho_s^n} \right), \tag{3.34}$$

where p^n and ρ_s^n are the solid pressure and density before the mixing. The new pressure can be immediately obtained from the solid phase equation of state

$$p^{n+1} = p_s \left(\rho_s^{n+1}, e_s^{n+1} \right). \tag{3.35}$$

Eliminating ρ from the mass 3.31 and momentum 3.32 equations gives

$$u^{n+1} = \frac{\Pi_0 - p^{n+1}}{M_1}, \tag{3.36}$$

which immediately can be used with 3.31 to obtain the density

$$\rho^{n+1} = \frac{M_1}{u^{n+1}}. \tag{3.37}$$

With the total density and solid density computed the gas density is obtained using 3.12

$$\rho_g^{n+1} = \frac{\lambda^n}{\frac{1}{\rho^{n+1}} - \frac{1-\lambda^n}{\rho_s^{n+1}}}. \tag{3.38}$$

By 3.14 the solid and gas pressures are equal and with ρ_g known, we can compute the specific internal energy of the gas

$$e_g^{n+1} = e_g(\rho_g^{n+1}, p^{n+1}). \tag{3.39}$$

The total specific internal energy is given by 3.13,

$$e^{n+1} = (1-\lambda^n)e_s^{n+1} + \lambda^n e_g^{n+1}. \tag{3.40}$$

Finally using the conservation of energy equation 3.33 we have

$$e^{n+1} + \frac{p^{n+1}}{\rho^{n+1}} + \frac{1}{2}\left(u^{n+1}\right)^2 - E_0 = 0. \tag{3.41}$$

This condition is used to form the basis an iterative scheme to adjust the flow variables when the gaseous phase is introduced. A secant method is used to iterate on ρ_s which is terminated when equation 3.41 is satisfied to a prescribed numerical accuracy, in this case when

$$e^{n+1} + \frac{p^{n+1}}{\rho^{n+1}} + \frac{1}{2}\left(u^{n+1}\right)^2 - E_0 < 5 \times 10^{-6},$$

the secant routine was terminated.

The expression for $\frac{d\omega}{dr}$ - derived in section 2.4.3 - used in these calculations was

$$\frac{d\omega}{dr} = \frac{D-u}{R_s}, \tag{3.42}$$

where R_s is the shock curvature. For a given detonation velocity D the model reduces to an eigenvalue problem in the shock curvature R_s. The numerical shooting method was used to determine R_s, integrating the flow equations from the shock until one of

the generalised CJ conditions 3.25 was satisfied, R_s was then varied using a bisection method and the flow equations integrated again. The bisection method was terminated when the fractional change in R_s was less than 1 in 10^{-5}.

3.3.5 Wood-Kirkwood Calculations

Figure 3.1 shows that for PBX9502 the detonation velocity at which extinction occurs is at a much higher fraction of D_{CJ} than that of EDC37. This suggests that EDC37 would support detonation velocities at a smaller fraction of its CJ speed compared to PBX9502 in 2D calculations. The curvature at which extinction occurs in PBX9502 is approximately half of that of EDC37. This can be understood by inspection of figure 3.2, which shows that the Detonation Driving Zone (DDZ) length (i.e. the distance between the shock and the sonic locus) increases more rapidly for PBX9502 as a function of curvature compared with EDC37. For small shock curvature the reaction zone thickness for PBX9502 is thinner than EDC37 which suggests that PBX9502 could sustain detonation at larger magnitudes of curvature than EDC37. However, the reaction zone thickness for PBX9502 is more sensitive to the entropy than EDC37, which is a function of the detonation velocity. As the shock front curvature increases (and detonation velocity decreases) the reaction zone thickness increases more rapidly for PBX9502 resulting in the failure curvature being smaller than that of EDC37.

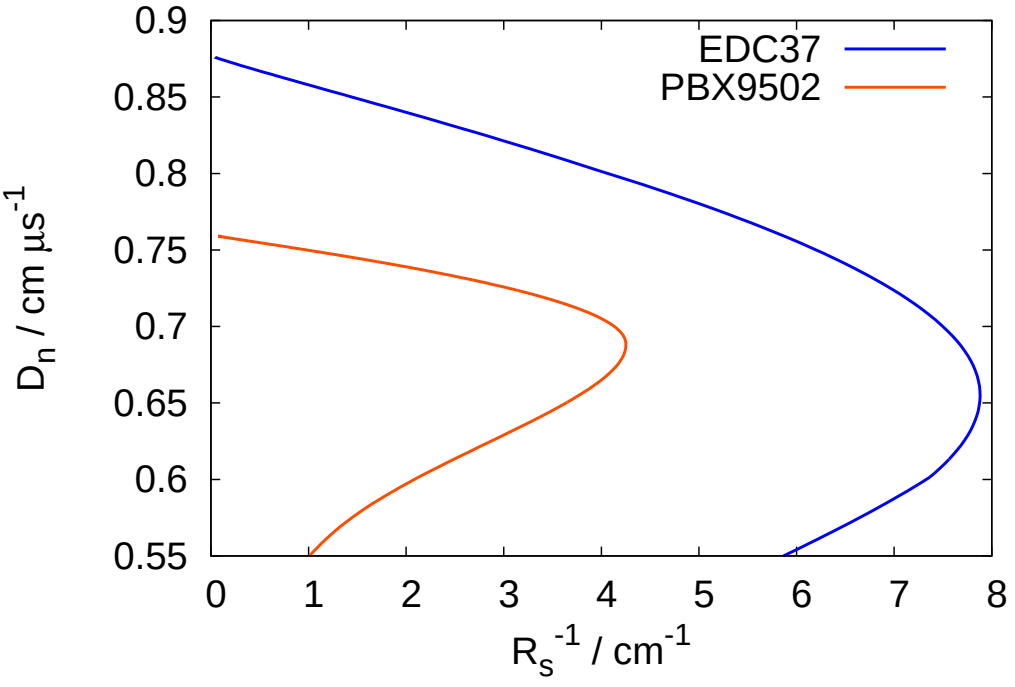

Figure 3.1: Normal shock velocity versus shock front curvature for CREST explosives models.

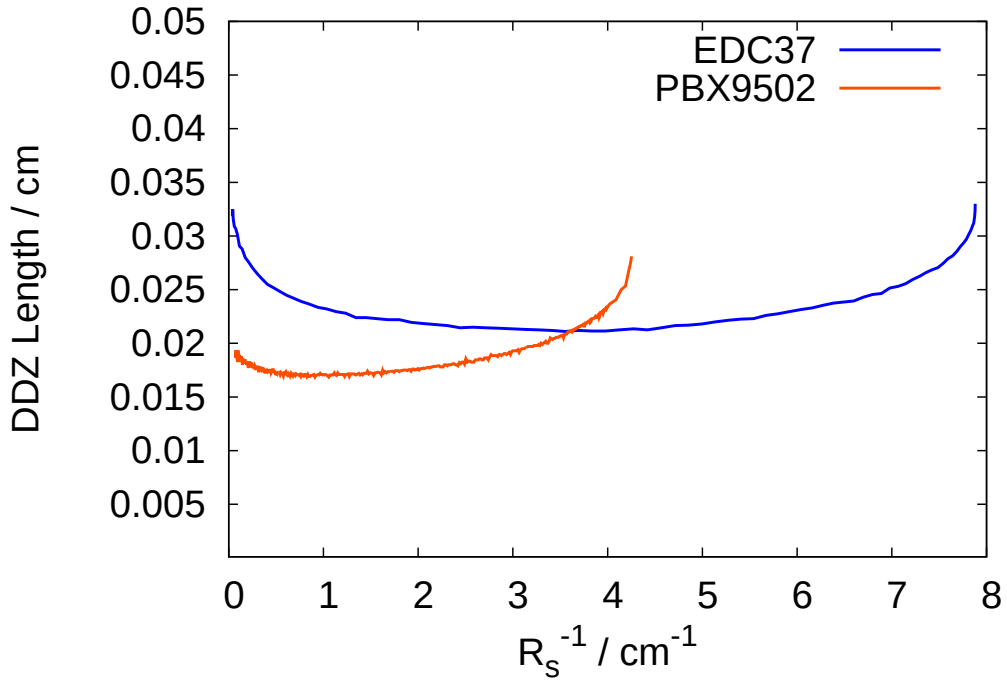

Figure 3.2: Distance between shock front and sonic locus for CREST explosive models. Only data up to the extinction point is shown.

Chapter 4

Numerical Methods for DNS

4.1 Introduction

Implementing the explosive model (i.e. equation of state and reaction rate) into the DNS requires the addition of a sub-routine to compute the equation of state and additional parameters related to the extent of reaction. An overview of the numerical scheme used to solve the rate-stick detonation problem is given.

4.2 Conservative Schemes

Solving the Euler equations using a conservative based scheme is a natural choice as only conservative schemes, if convergent, will converge to the weak solution of the conservation law [40]. As the detonation problem involves a propagating shock and the chemical reaction rate depends on the shock strength it is important that the shock is captured accurately.

Equations 2.1-2.4 without the source terms can be expressed in differential con-

servation form as

$$\frac{\partial \mathbf{u}}{\partial t} + \frac{\partial \mathbf{f}}{\partial x} = 0, \tag{4.1}$$

where $\mathbf{u}$ is a vector of primitive variables and scalars, $\mathbf{f} = \mathbf{f}(\mathbf{u})$ is the corresponding flux vector and is a function of $\mathbf{u}$. For shock-capturing it is necessary to use the weak, or integral, formulation of the equations. Using one spatial dimension we consider an arbitrary fixed interval $[x_1, x_2]$ in which the corresponding integral form of 4.1 is

$$\frac{d}{dt}\int_{x_1}^{x_2} \mathbf{u}\, dx + \mathbf{f}(x_2, t) - \mathbf{f}(x_1, t) = 0. \tag{4.2}$$

We now consider a numerical domain split into J cells, of equal width, where the jth cell is given by

$$x_{j-1/2} = x_L + (j-1)\Delta x \leq x \leq x_{j-1/2} = x_L + j\Delta x \quad \left[\Delta x = \frac{x_R - x_L}{J}\right].$$

Here x_L and x_R are the left and right boundaries of the $x-$domain and x_j are nodes located at the centre of each cell as shown in figure 4.1. Between each node at $x = x_j$ are cell interfaces located at $x = x_{j-1/2}$ and $x = x_{j+1/2}$. We define the average of $\mathbf{u}$ in the jth cell at time $t = t_k$ by

$$\mathbf{u}_j^k = \frac{1}{\Delta x}\int_{x_{j-1/2}}^{x_{j+1/2}} \mathbf{u}(x, t_k) dx. \tag{4.3}$$

Putting $x_1 = x_{j-1/2}$, $x_2 = x_{j+1/2}$ and integrating from t_k to t_{k+1} then 4.2 becomes

$$\int_{t_k}^{t_{k+1}} \frac{d}{dt}\int_{x_{j-1/2}}^{x_{j+1/2}} \mathbf{u}(x, t_k)\, dx + \int_{t_k}^{t_{k+1}} \left[\mathbf{f}(x_{j+1/2}, t) - \mathbf{f}(x_{j-1/2}, t)\right] dt = 0.$$

Using the definition of the cell average in 4.3 we can write

$$\mathbf{u}_j^{k+1} = \mathbf{u}_j^k + \frac{1}{\Delta x}\int_{t_k}^{t_{k+1}} \left[\mathbf{f}(x_{j-1/2}, t) - \mathbf{f}(x_{j+1/2}, t)\right] dt. \tag{4.4}$$

This expression is the starting point for all conservative schemes. It tells us that for a cell located at $x = x_j$ and time $t = t_k$ we are required to compute the time integral of

the flux at the interface with the adjacent cell at $x = x_{j+1/2}$ and $x = x_{j-1/2}$. Equation 4.4 is exact provided that the fluxes $\mathbf{f}$ are known exactly. However, since the flux is not known exactly an approximation must be made to the time integral of the flux. Applying equation 4.3 for the cell average to the time integral of the flux function in 4.4 we can write

$$\mathbf{u}_j^{k+1} = \mathbf{u}_j^k + \frac{\Delta t}{\Delta x}\left[\bar{\mathbf{f}}_{j-1/2} - \bar{\mathbf{f}}_{j+1/2}\right]. \tag{4.5}$$

Here $\bar{\mathbf{f}}_{j-1/2}$ is the time average of the numerical flux at the jth cell interface. The method chosen to approximate the numerical flux is the feature that distinguishes different conservative schemes. One obvious choice is the central difference approximation to the flux given by

$$\bar{\mathbf{f}}_{j+1/2} = \frac{1}{2}\left[\mathbf{f}_{j+1}^k + \mathbf{f}_j^k\right],$$

where the flux $\mathbf{f}_j^k = \mathbf{f}(\mathbf{u}_j^k)$ is a function of the solution state. This scheme can be shown to be unconditionally unstable even for a simple linear advection problem. Therefore an alternative approach must be considered. One solution to this problem is the method of calculating the flux due to Godunov.

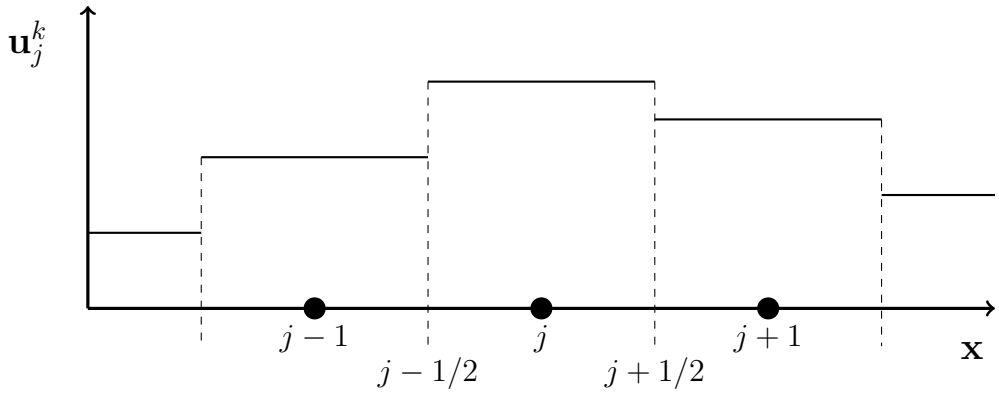

Figure 4.1: Piece-wise constant distribution of variables in a conservative scheme at time t_k. Each cell, centred at node $x = x_j$, has cell interfaces located at $x = x_{j-1/2}$ and $x = x_{j+1/2}$. In a conservative scheme it is assumed that the cell average is constant over a time step.

4.3 Godunov Schemes

The approach of Godunov [41] was to utilize the assumption that the solution at a given time was described by a series of piece-wise constant states. At the edges of a cell there is a discontinuity as the solution jumps to that of the neighbouring cell as shown in figure 4.1. In isolation this discontinuity forms a local Riemann problem at the interface between adjacent cells - the solution of which can be found iteratively.

The solution to the Riemann problem, for the one-dimensional Euler equations, can contain three types of wave: rarefactions, a contact discontinuity and shocks. Figure 4.2 shows a schematic of one of the possible wave patterns in which the shock and contact waves have positive wave velocity and the rarefaction wave has negative wave velocity. The three waves separate constant states in the flow; the solution is smooth and continuous through the rarefaction wave and discontinuities in the flow separate the solutions for the contact and shock waves. Other solution patterns are possible [42].

As the solution state, $\mathbf{u}$, at the interface is constant in time and can be determined exactly for the Riemann problem the corresponding flux $\mathbf{f}$ can then be used in equation 4.5 to update the solution in a cell.

Figure 4.3 illustrates the Godunov method in one spatial dimension. At cell j there are two solutions to the Riemann problem at nodes $j - 1/2$ and $j + 1/2$. The solutions to these Riemann problems are taken at time t_{k+1} and are used to compute the numerical flux in equation 4.4 to update the solution in the cell. An important feature in 4.3 is that at time t_{k+1} the solutions of the two Riemann problems either side of cell j do not overlap - a small enough time step Δt must be used to ensure that no information is lost in the solution.

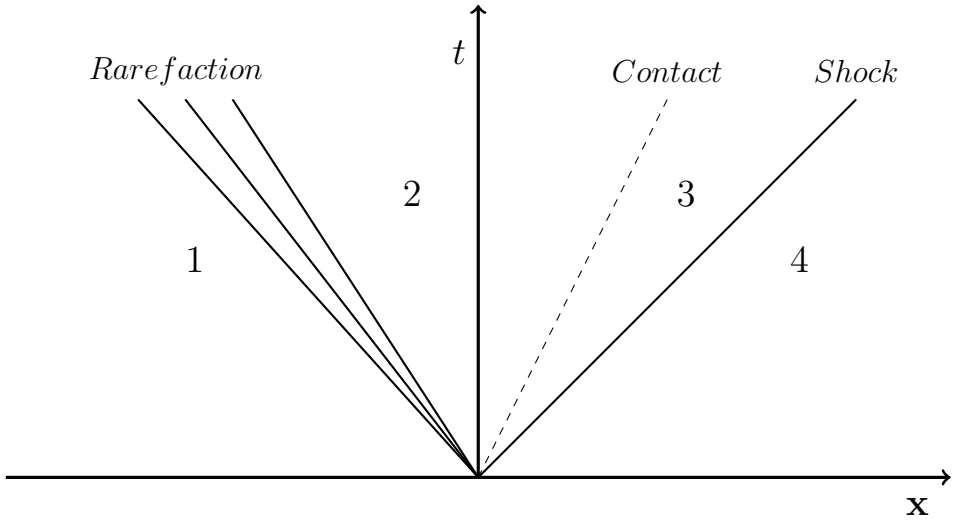

Figure 4.2: Schematic of the solution regime in $x - t$ space of the one-dimensional Riemann problem. There are four regions where the solution is constant. These regions are separated by a rarefaction wave, contact discontinuity and a shock wave.

Each Riemann problem at cell interfaces can be solved exactly using an iterative

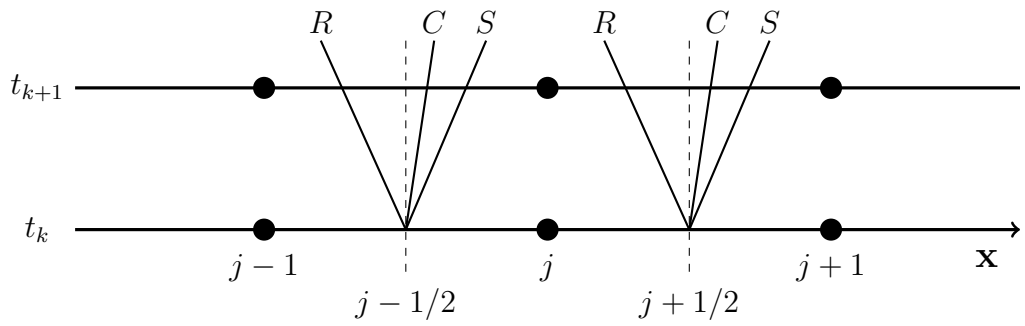

Figure 4.3: Illustration of Godunov's method - the solution at node $[j, t_{k+1}]$ is updated using the fluxes at the interfaces $j-1/2$ and $j+1/2$. The fluxes at the interfaces are obtained from the solution to the Riemann problem. The waves separating the solution state for each Riemann problem are shown labelled as R, C, S corresponding to the rarefaction, contact and shock solution.

method. However, this process can be become computationally expensive when a large number of numerical cells are being used with an arbitrary equation of state. To this end a number of approximate Riemann solvers have been developed.

4.4 HLLC Scheme

The HLLC approximate Riemann solver was used for the DNS calculations. It was chosen as it maintains contact and shear waves [43]. This is important for 2D rate-stick calculations where the explosive is confined by an inert with a steep profile at the interface. If a solver were too diffuse this boundary would become smoothed changing the initial conditions of the pre-shocked explosive - this may have an effect upon the post-shock state of the flow and affect the wave speed. Another advantage of the HLLC

scheme over other schemes, such as those due to Roe and Osher, is that the Jacobian of the flux vector is not required. As the CREST equation of state 3.1 requires extensive computation for each call, use of the HLLC scheme avoids the computational expense of calculating the Jacobian.

The HLLC approximate Riemann solver assumes that there are four constant solution states, separated by three waves with speeds S_L, S_R, S_* corresponding to the smallest, largest and intermediate wave speeds (the wave speeds can be negative). The smallest and largest wave speeds are determined from the initial state of the Riemann problem, the intermediate wave speed S_* is approximated using a combination of the smallest and largest wave speeds. The solution state is given by

$$\bar{\mathbf{u}} = \begin{cases} \mathbf{u_L} & \text{if } 0 \leq S_L\,, \\ \mathbf{u_{*L}} & \text{if } S_L \leq 0 \leq S_*\,, \\ \mathbf{u_{*R}} & \text{if } S_* \leq 0 \leq S_R\,, \\ \mathbf{u_R} & \text{if } 0 \geq S_R\,. \end{cases} \tag{4.6}$$

Here $\mathbf{u_L}$ and $\mathbf{u_R}$ correspond to the solution states 1 and 4 in figure 4.2 and correspond to the initial left and right states in the Riemann problem. Here we are using the convention that S_L is the slowest wave and S_R is the fastest. The intermediate wave S_* separates states $\mathbf{u_{*L}}$ and $\mathbf{u_{*R}}$. These states are given by

$$\mathbf{u_{*K}} = \rho_K \left(\frac{S_K - u_K}{S_K - S_*} \right) \begin{bmatrix} 1 \\ S_* \\ \frac{E_K}{\rho_K} + (S_* - u_K) \left[S_* + \frac{p_K}{\rho_K (S_K - u_K)} \right] \end{bmatrix}, \tag{4.7}$$

where $K = L$ for the left state and $K = R$ for the right state. Here the vector u_{*K} corresponds to the conserved variables in mass, momentum and energy. To implement

the HLLC scheme the numerical flux is required, this is given by

$$\mathbf{f^{hllc}} = \begin{cases} \mathbf{f_L} & \text{if } 0 \leq S_L\,, \\ \mathbf{f_{*L}} = \mathbf{f_L} + \mathbf{S_L}\left(\mathbf{u_{*L}} - \mathbf{u_L}\right) & \text{if } S_L \leq 0 \leq S_*\,, \\ \mathbf{f_{*R}} = \mathbf{f_R} + \mathbf{S_R}\left(\mathbf{u_{*R}} - \mathbf{u_R}\right) & \text{if } S_* \leq 0 \leq S_R\,, \\ \mathbf{f_R} & \text{if } 0 \geq S_R\,, \end{cases} \tag{4.8}$$

where u_{*L} and u_{*R} are given by 4.7. This approximation to the numerical flux is used in equation 4.5 to integrate the solution in time. For an advected scalar q (e.g. the reaction parameter) the HLLC state is given by

$$(\rho q)_{*K} = \rho_K \left(\frac{S_K - u_K}{S_K - S_*}\right) q_K, \tag{4.9}$$

which can then be used in equation 4.8 to compute the corresponding flux.

The middle wave speed S_* was calculated based upon the expression developed by Batten [44]

$$S_* = \frac{p_R - p_L + \rho_L u_L\left(S_L - u_L\right) - \rho_R u_R\left(S_R - u_R\right)}{\rho_L\left(S_L - u_L\right) - \rho_R\left(S_R - u_R\right)}. \tag{4.10}$$

This choice of wave speed estimate has the advantage that it is unchanged if a different equation of state is implemented.

4.5 MG Software

The DNS calculations were performed using Falle's *MG* software [45][46]. In the following section some important features of the software are discussed and an overview of the adaptations made to the software to incorporate the multi-phase CREST model.

4.5.1 Adaptive Mesh Refinement

MG utilises Adaptive Mesh Refinement (AMR) such that high resolution (i.e. smaller numerical cells) is employed only where necessary. To achieve this it employs a hierarchical structure of grids $G^0, G^1, ..., G^N$ where $N+1$ is the total number of levels. The grid spacing, h_n, for G^n is given by $\frac{h_0}{2^n}$, where h_0 is that on G^0. The solution on grids G^0 and G^1 are present across the whole domain. Refinement beyond grid G^1 is determined by comparing the differences in the solution between G^{n-1} and G^n in each cell on G^n. If this exceeds a set tolerance then the cell is refined to G^{n+1}. The refinement algorithm continues to be applied until the difference between the solutions on two levels is smaller than the tolerance or the solution has been refined to the maximum level N (specified by the user).

For the simulations performed in this thesis an additional refinement algorithm, based upon the chemical reaction rate, was included to ensure that the solution was always resolved to the finest level in the reaction zone.

4.5.2 Second Order Integration

Second order accuracy is achieved by integrating the first order scheme (equation 4.5) to get the solution $\mathbf{u}_j^{k+1/2}$ at the half time step. Average gradients of the primitive variables $\mathbf{p} = (\rho, u, v, p)$, in each cell, are computed and then used to update the fluxes in the Riemann problem to achieve second order integration.

The gradient in the axial coordinate direction is

$$\left(\frac{\partial \mathbf{p}}{\partial z}\right)_{ij}^{k+1/2} = \frac{1}{h} av\left(\mathbf{p}_{ij}^{k+1/2} - \mathbf{p}_{ij-1}^{k+1/2}, \mathbf{p}_{ij+1}^{k+1/2} - \mathbf{p}_{ij}^{k+1/2}\right), \tag{4.11}$$

where i, j correspond to the indices for the radial and axial cells and h is the cell width. Here $av(a, b)$ is a non-linear averaging function. It has the effect of reducing

the numerical scheme to first order in the region of discontinuities. This is necessary as Godunov showed that a second order scheme is not monotonic near discontinuities [41]. The averaging function is given by [45]

$$av(a,b) = \frac{a^2 b + ab^2}{a^2 + b^2}. \tag{4.12}$$

With the gradients determined the left and right states in the Riemann problem at the half time-step are

$$\begin{aligned} \mathbf{p}_L &= \mathbf{p}_{ij}^{k+1/2} + \frac{h}{2}\left(\frac{\partial \mathbf{p}}{\partial z}\right)_{ij}^{k+1/2}, \\ \mathbf{p}_R &= \mathbf{p}_{ij+1}^{k+1/2} - \frac{h}{2}\left(\frac{\partial \mathbf{p}}{\partial z}\right)_{ij+1}^{k+1/2}, \end{aligned} \tag{4.13}$$

with the corresponding flux given by

$$\mathbf{f}_{ij+1/2}^{k+1/2} = \mathbf{f}\left(\mathbf{p}_L, \mathbf{p}_r\right). \tag{4.14}$$

The solution is advanced to the complete time-step t_{k+1} using these fluxes in equation 4.5. The resulting numerical scheme is upwind, explicit and second order in smooth regions. A more complete discussion of the second order scheme, applied to the axisymmetric Euler equations, is given by Falle [46].

4.5.3 Additional Solution Parameters

Implementing the CREST model into MG required the addition of an equation of state sub-routine and some additional advected scalars. The additional advected scalars required were $\rho_s, e_s, \lambda_1, \lambda_2, \lambda_t, \delta_e$. To prevent the confiner reacting an additional scalar was used to determine whether a given cell was explosive or the confiner. Here δ_e indicates whether a given cell was explosive material or confiner. It took on the values

of

$$\delta_e = \begin{cases} 1 & \text{if explosive,} \\ 0 & \text{if confiner.} \end{cases} \tag{4.15}$$

The confiner was modelled with the CREST equation of state at a lower initial density than that of the explosive. The initial pressure was matched to that of the explosive.

4.5.4 Reaction Source Term

To ensure that the reaction occurred in the shocked explosive only, criteria were placed on the initiation of the chemical reaction source terms. In this thesis the reaction source term refers to the term appearing on the RHS of the reactive Euler equations (see equation 2.6), which is given by the density times the reaction rate equation W. The criteria for reaction were based upon the pressure in the cell and whether the cell was explosive/confiner material i.e.

$$\begin{array}{ll} p > p_c \,; \delta_e > \delta_c & \text{add reaction terms,} \\ \text{otherwise} & \text{ignore reaction terms.} \end{array}$$

These criteria ensured that the chemical reaction source terms were added in shocked explosive material only. The values $p_c = 0.05\, Mbar$ and $\delta_c = 0.99$ were used throughout. The choice of p_c was based upon 10% of the CJ pressure for the EDC37 explosive.

In CREST the reaction rate is strongly dependent upon the entropy of the shocked solid. It is therefore important that the numerical scheme calculates the correct entropy for the solid. If there was a mixture of solid and gas in the shock it is not clear how that would change the entropy of the solid phase. If the entropy of the shocked solid were incorrectly calculated this would have an impact upon the time for the reaction to complete and effectively change the length scales in the problem.

To prevent the gas phase being present in the shock the mixture model can be switched on after a delay by requiring $\lambda > \epsilon$ (here $\lambda = \times 10^{-2}$). For $\lambda < \epsilon$ the density and specific internal energy are given by the solid equation of state only. This will ensure that the shock for the solid phase is captured correctly. As MG uses shock-capturing it is important that only the solid phase is present in the shock - this is necessary to ensure the shock relations are satisfied within the numerical scheme. If significant amounts of gas phase were introduced then there internal structure of the shock could have a large impact on the reaction dynamics behind it. In addition the steady state models assume the shock occurs in the solid only ($\lambda = 0$) and we want to get as close to that as possible. Previous calculations with CREST [36] prevented reaction occurring in the shock structure using an alternative method termed 'q-switching'. The magnitude of the artificial viscosity would increase at the shock and reduce immediately behind it. It was only after the reduction in the artificial viscosity that the reaction was initiated, thus preventing reaction inside the shock structure.

4.5.5 Equation of State - Pressure

When implementing an equation of state into a hydrodynamic code the equation of state is necessary to compute the pressure from the conserved variables. At each new time step the conserved variables give (e, ρ, λ). For a simple equation of state, such as the polytropic equation given by 2.37 the pressure can be computed explicitly from the conserved variables.

In the case where only the solid phase is present the code computes the pressure by using the analytic expression $p = p_s(\rho, e)$ which can be obtained from 3.1. When the solid/gas mixture is switched on computing the pressure involves solving the mixture equations 3.11-3.14 iteratively. The procedure is as follows, we begin by making an

initial guess for the new solid phase density ρ_s^1 (a superscript 1 indicates the next time step, a superscript 0 indicates the previous step) and apply the isentropic expansion of the solid to obtain

$$e_s^1 = e_s^0 + p^0 \left(\frac{1}{\rho_s^1} - \frac{1}{\rho_s^0} \right).$$

The gas phase density and specific internal energy are obtained from the mixture equations

$$\rho_g^1 = \frac{\lambda^1}{\frac{1}{\rho^1} - \frac{(1-\lambda^1)}{\rho_s^1}},$$

and

$$e_g^1 = \frac{e^1 - (1-\lambda^1)e_s^1}{\lambda^1}$$

With the solid and gas phase parameters determined the mechanical equilibrium condition is

$$p_s(\rho_s^1, e_s^1) - p_g(e_g^1, \rho_g^1) = 0.$$

A secant routine was used to iterate on the solid density, terminating when the pressure difference was smaller than $10^{-3}\, MBar$. The advected scalars corresponding to the solid phase density and specific internal energy were updated with the new values. These values are then used as the initial state of the solid phase in subsequent calls of the equation of state routine.

4.5.6 Solid Phase Equation of State

Previous calculations [36] using CREST employed the snowplough model for the unreacted equation of state. The snowplough model assumes that the unreacted explosive is shocked at zero pressure up to the theoretical maximum density ρ_{0s} (maximum here implies zero porosity), above which a finite pressure is present in the explosive. Practically, this means that for $\rho < \rho_{0s}$ an equation of state call will return $p = 0$. For

the unreacted equation of state, as described by equation 3.1, for densities $\rho < \rho_{0s}$ and a small specific internal energy the equation of state returns $p < 0$. This behaviour is problematic as complex sound speeds can be obtained and causes problems in the numerical code. One option to prevent negative pressures being returned is to use a numerical cut-off, such that for $\rho < \rho_{0s}$ the EOS returns $p = 0$. However, it would be preferable to have $p \to 0$ as $\rho \to 0$. To achieve this behaviour in the EOS a blending function was applied to the reference pressure curve centred at the reference density ρ_{0s}. The form of the new pressure reference curve is

$$p_i(\rho) = \alpha \; p_{i-old} + (1 - \alpha) \; p_{i-new}, \tag{4.16}$$

where p_{i-old} is the first equation in 3.2. Here α is determined by a *tanh* function

$$\alpha = \frac{1}{2}\left(1 + \tanh\left[\frac{\rho - \rho_{ref}}{k}\right]\right), \tag{4.17}$$

which for small k has similar properties to a heaviside function centered at $\rho = \rho_{ref}$. The modified pressure reference curve was given by simple polynomial in ρ.

$$p_{i-new} = \frac{1}{5}\left(2\left(\frac{\rho}{\rho_0}\right)^{10} + 3\left(\frac{\rho}{\rho_0}\right)^{12}\right) p_{i-old}(\rho_{ref}). \tag{4.18}$$

This ensures that $p_i(\rho)$ is always positive and that $p \to 0$ as $\rho \to 0$. For all CREST calculations $\rho_{ref} = 1.03\rho_{0s}$ and $k = 0.2\, gcm^{-3}$ were used. The exponents in 4.18 were chosen to give a smooth pressure profile between $\rho = 0$ and $\rho = \rho_0$. Figure 4.4 shows how the use of the blending function modifies the unreacted EOS compared to the original EOS. Within the detonation driving zone (i.e. where the flow is subsonic relative to the shock) $\rho_s > \rho_{0s}$ and thus the change to the equation of state is not expected to have an affect on the results compared to using the original pressure reference curve. Indeed the minimum solid phase density in the one-dimensional solution is $\rho_s = 2.75\, gcm^{-3}$. Inspection of figure 4.4 indicates that at this density the blended EOS matches the

original EOS well. The regions where the low densities are observed in 2D calculations are downstream of the shock near the explosive-confiner interface where unreacted solid undergoes a transonic Prandtl-Meyer expansion. As the flow is supersonic here this region will have no influence on the shock and thus not affect the detonation solution.

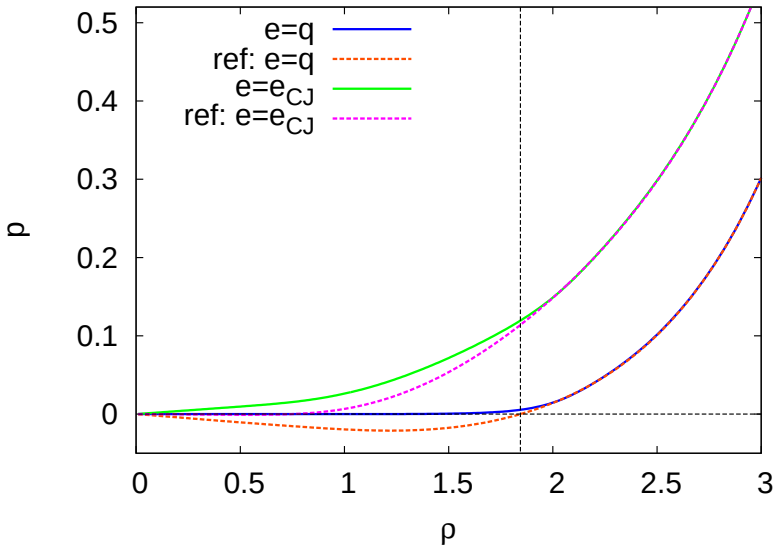

Figure 4.4: Pressure as a function of density (at fixed specific internal energy) showing how the blended EOS modifies the original EOS (labelled *ref* curves for the unreacted explosive. The legend indicates different values of specific internal energy: e_{CJ} is the post-shock internal energy from the shock relations for $D = D_{CJ}$; $e = q$ is effectively zero specific internal energy where the internal energy is comprised of the detonation specific energy only. The vertical dashed line indicates where the blending function is centred.

4.5.7 Artificial Dissipation

In Godunov-type numerical schemes the shock is spread over a finite number of computational cells. As the shock propagates across the domain the internal structure of the shock will vary depending upon the alignment of the shock with the grid. These variations in structure generate numerical noise that can be transported downstream and can affect the accuracy of results. For a fast moving shock short-wavelength noise is produced that is rapidly dissipated by the numerical scheme and thus does not affect the solution. However, for stationary or slowly moving shocks, long wavelength perturbations are generated that are not sufficiently dissipated by the numerical scheme and, in some cases, can produce unphysical results [47]. Notable examples of these include expansion shocks resulting from corners and the carbuncle phenomena, which occurs when a static bow shock is closely aligned with the grid [48].

One method of avoiding these phenomena is to introduce some artificial dissipation into the numerical scheme [49]. In this case the artificial dissipation is added directly to the approximate Riemann solver and this method has been used in previous calculations using the MG software for Magnetohydrodynamic calculations and explosive rate-stick calculations [30][35][45]. Two forms of artificial dissipation were used; one based upon a dynamic viscous stress and a heat conduction term. The artificial viscosity terms spread the shock over a greater number of cells. The artificial heat conduction was included to prevent the specific internal energy becoming negative, this was observed in 2D calculations with the PBX9502 CREST model. This problem has been previously observed in the literature in regions where the kinetic energy is much larger than the thermal energy [48].

The artificial viscosity terms were added to the momentum and energy flux and the artificial heat conduction was added to the energy flux in the approximate Riemann

solver. Each of the terms was computed based upon the left and right states in the Riemann solver, represented by L and R subscripts in the following equations. The viscous momentum flux vector was given by

$$\mathbf{f_v} = \alpha_v c_{vis} \left(v_L - v_R \right), \tag{4.19}$$

which is only applied to the velocity component normal to the interface. For each component in 4.19 there is a viscous energy flux term of the form

$$F_v = \frac{\alpha_v c_{vis}}{2} \left(v_L - v_R \right) \left(v_L + v_R \right), \tag{4.20}$$

where there is a contribution from the radial and axial components of the viscous flux vector. The artificial heat conduction term was

$$F_e = \alpha_e c_{vis} \left(\beta_L - \beta_R \right), \tag{4.21}$$

where β was chosen based upon the expression for the solid phase entropy 3.9

$$\beta = e_s - e_i. \tag{4.22}$$

Here α_v and α_e are dimensionless constants, c_{vis} is a weighted average of the sound speed and densities in the left and right states of the Riemann problem

$$c_{vis} = \frac{2}{\frac{1}{\rho_L c_L} + \frac{1}{\rho_R c_R}}, \tag{4.23}$$

where ρ_L, c_L and ρ_R, c_R are the density and sound speeds of the left-state and right states respectively. Away from the shock the artificial dissipation terms are $O(\Delta x^2)$ and thus do not affect the order of the scheme in smooth regions [45].

Chapter 5

DNS Calculations

5.1 Introduction

In the following chapter one and two-dimensional DNS calculations with CREST are described and results presented. The one-dimensional simulations are verified via a direct comparison with results from the steady state ZND model.

5.2 One-dimensional Simulations

5.2.1 Introduction

One-dimensional calculations are used as an important test bed when developing any detonation model for a number of reasons. Firstly, they are computationally cheaper to run - when compared with two-dimensional calculations - which reduces lead times on studies for determining explosive model parameters. Secondly simple numerical convergence studies can be performed which can inform on the minimum resolutions required for two-dimensional calculations. Finally, one can make a direct comparison

between the DNS solution and the steady-state ZND model of detonation. In the limit of steady state detonation these solutions should be identical. Verification between DNS and the ZND model is important to ensure that the implementation of the equation of state and reaction rate is correct.

A number of one-dimensional studies were performed for the CREST EDC37 and PBX9502 models: a numerical convergence study; a comparison between the DNS solution obtained in different frames of reference; and the solution from the DNS is compared to the steady state ZND model.

5.2.2 Numerical details for 1D calculations

Details of the numerical domain used for the laboratory frame calculations are given in table 5.1. A high pressure region, at the left-hand-side of the explosive domain initiates a detonation wave that propagates from left-to-right. The wave was allowed to propagate until $z > 0$ (approximately $O(100)$ reaction zone lengths) to ensure a steady state solution was obtained. The solution was then transformed to the shock-attached frame by applying a velocity shift across the entire domain. The detonation wave would then propagate either left or right dependent upon the magnitude of the shift. The magnitude of the velocity shift was varied until the detonation wave became static on the grid. The magnitude of the velocity shift corresponds exactly to the detonation wave speed. For the stationary calculations the shock front was maintained at $z = 0$. This procedure was repeated for resolutions of $[20, 40, 80, 160, 320, 640]\, cells/mm$ for the EDC37 and PBX9502 explosive models. In these calculations no AMR was utilised.

When comparing the DNS solution and the result from the steady state ZND solution the stationary shock solution was used.

The artificial dissipation parameters (see equations 4.19 and 4.21) used in the

Coordinate / cm	Boundary Condition	Initial State
$z = -2.0$	Free	CJ
$-2.0 < z < -1.9$	N/A	CJ
$-1.9 < z < 0.2$	N/A	Unreacted
$z = 0.2$	Fixed	Unreacted

Table 5.1: Details of the initial setup of the laboratory frame 1D calculations. The term 'CJ' refers to post-shock state of the explosive determined by the shock relations. 'Unreacted' is the quiescent state of the explosive.

laboratory frame calculations were:

$$\alpha_v = 0.2,\ \alpha_e = 0.2.$$

For the stationary shocks the parameters were:

$$\alpha_v = 0.6,\ \alpha_e = 0.2.$$

It was necessary to increase the magnitude of the artificial viscosity for the stationary shock calculations to produce a stable shock structure. When working in the shock attacked frame the shock is spread over fewer grid cells compared to a moving shock and can produce unwanted numerical noise. Increasing the magnitude of the artificial viscosity spreads the shock over a greater number of grid cells and allows for a stable shock structure to be formed.

To enable the number of a cells in the reaction zone a simple routine was developed that would compute the reaction source term in each cell. A cell was defined to be in the reaction zone if the source term $\rho W > 0.1$ (where W is the reaction rate).

5.2.3 DNS Convergence

EDC37

Cells/mm.	Cells in reaction zone	Reaction in shock?
20	6	Yes
40	14	Yes
80	27	No
160	52	No
320	104	No
640	204	No

Table 5.2: Number of grid cells in the reaction zone for various resolutions for EDC37. The data was obtained from stationary shock solutions. Also indicated is whether reaction (i.e. mixture EOS) occurred inside the shock structure.

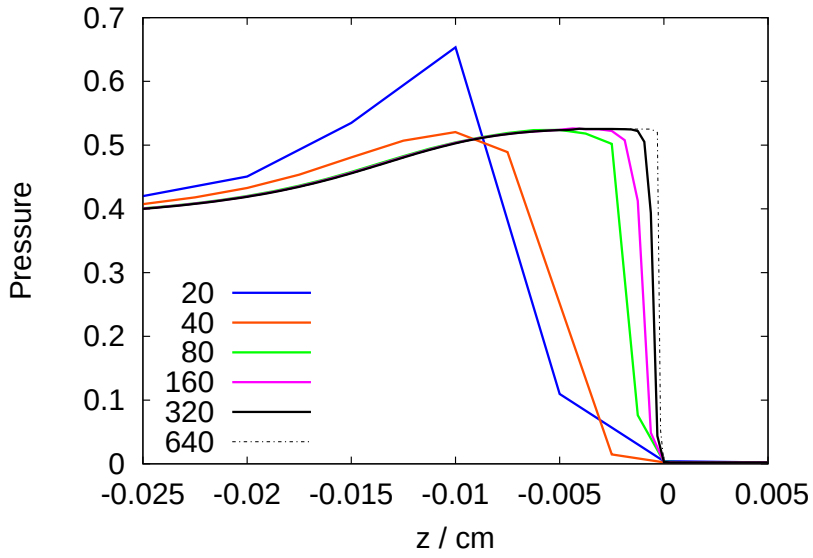

(a) Pressure.

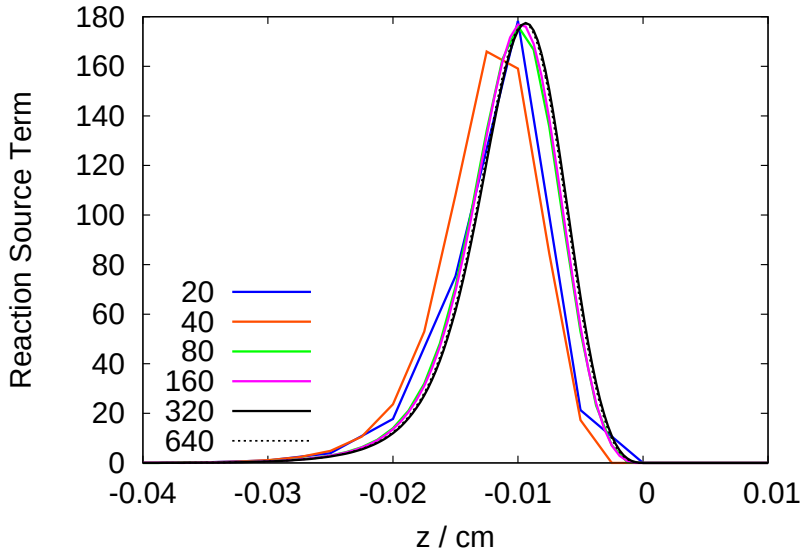

(b) Reaction source term.

Figure 5.1: One-dimensional simulations of EDC37 - legend indicates resolution in cells/mm. The solution is in the shock-attached frame.

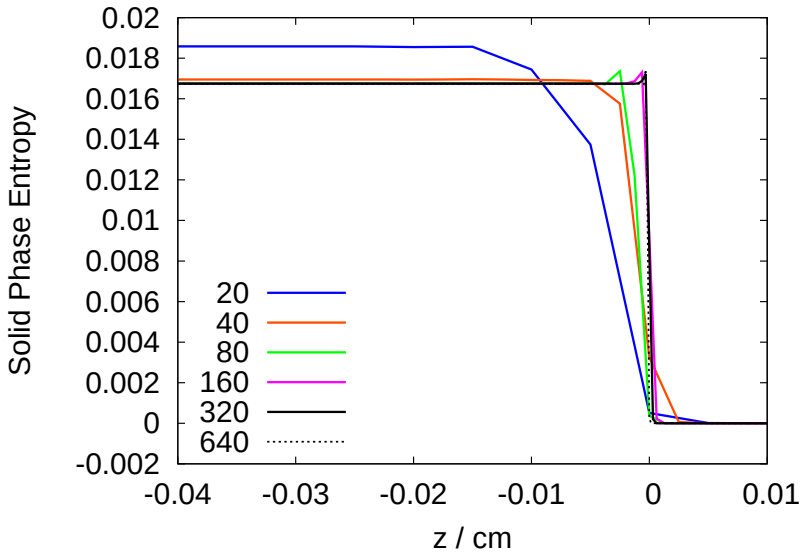

(a) Solid phase entropy.

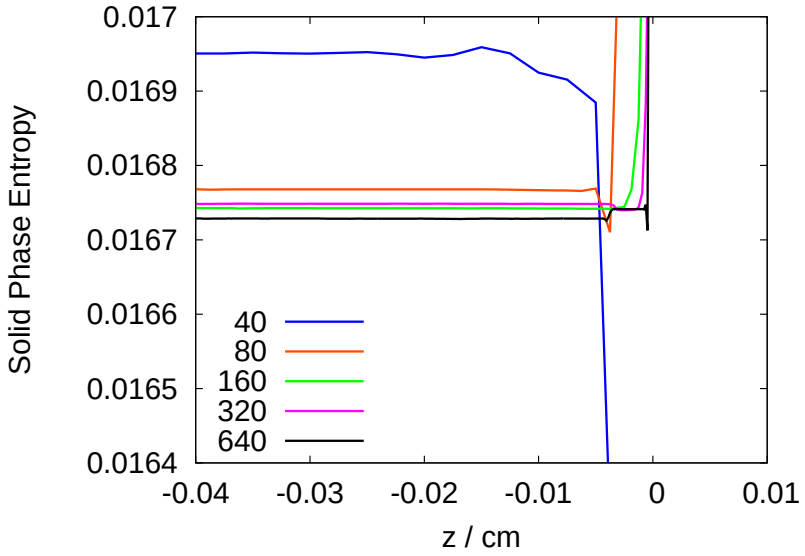

(b) Solid phase entropy with the y-axis zoomed in.

Figure 5.2: One-dimensional simulations of EDC37 - legend indicates resolution in cells/mm. The solution is in the shock-attached frame.

PBX9502

Cells/mm	Cells in reaction zone	Reaction in shock?
20	4	Yes
40	8	Yes
80	9	Yes
160	27	Yes
320	63	No
640	122	No

Table 5.3: Number of cells in the reaction zone as a function of resolution for PBX9502. The data was obtained from stationary shock solutions.

Table 5.2 shows that for EDC37 at least 80 cells/mm are required to ensure there is no reaction in the shock, which corresponds to 27 cells in the reaction zone. Moreover, for PBX9502, table 5.3 shows that at least 320 cells/mm are required to obtain no reaction in the shock, which corresponds to 63 cells in the reaction zone. The difference in resolution requirements can be understood by comparing figures 5.1(b) and 5.3(b). There is a significant induction zone behind the shock for EDC whereas for PBX9502 the reaction rate increases more rapidly behind the shock. It should be noted that the reaction source curve for PBX9502 is not a smooth bell shaped curve, this is due to the reaction rate limiters [50], which results in the reaction rate being clipped and producing a kink. For EDC37 this is not evident and the reaction rate follows a smooth bell shaped curve.

Resolution studies of 2D calculations have shown that at least 50 numerical cells, in the reaction zone, are required to obtain converged results [28]. However, this study was performed using a polytropic EOS and power law reaction rate where the reaction

rate is maximal at the shock. The CREST reaction rate has an induction zone, as shown in figure 5.1(b), which may affect the number of cells required inside the reaction zone to obtain converged results. The resolution study here indicates that for > 50 cells in the reaction zone requires 160 cells/mm for EDC37 and 320 cells/mm for PBX.

Figure 5.2(a) shows that the solid phase entropy does not monotonically increase through the shock, at higher resolutions. The entropy reaches a maximal value through the shock and then reduces in magnitude by a small amount. This feature occurs before the mixture equations are initiated (i.e. $\lambda < \epsilon$) and hence only the unreacted equation of state is used here. This feature is an artefact of the numerical scheme and is not physical. It arises from the averaging function used to achieve second order time-integration discussed in section 4.5.2. For a second order scheme one cannot guarantee monotonicity through the shock [41]. As the over-calculation of entropy appears to occur in one numerical cell it will have a negligible impact on the calculations.

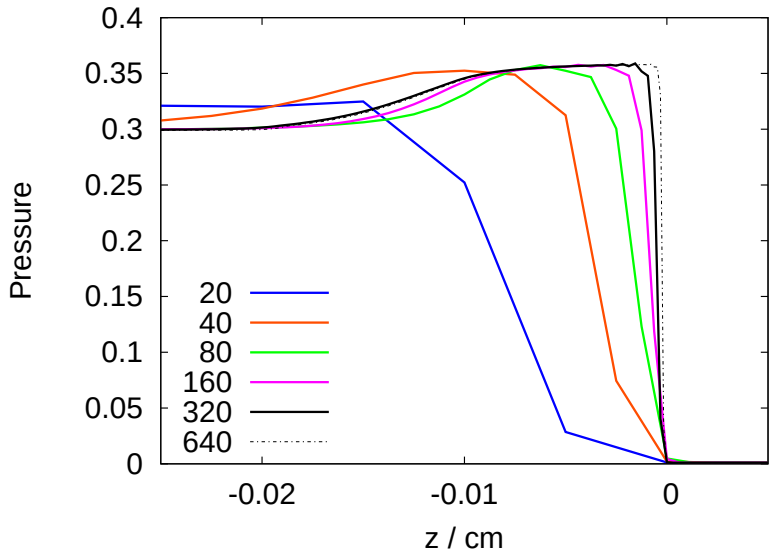

(a) Pressure.

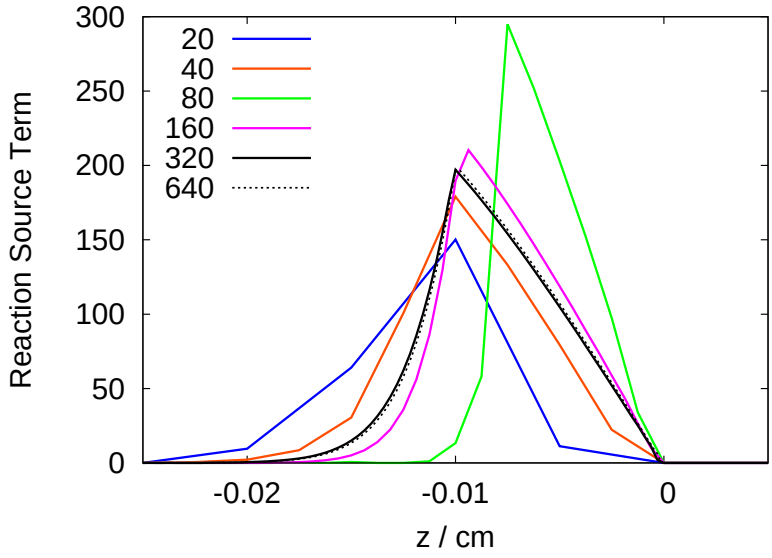

(b) Reaction Source Term.

Figure 5.3: One-dimensional simulations of PBX9502 - legend indicates resolution in cells/mm. The solution is in the shock-attached frame.

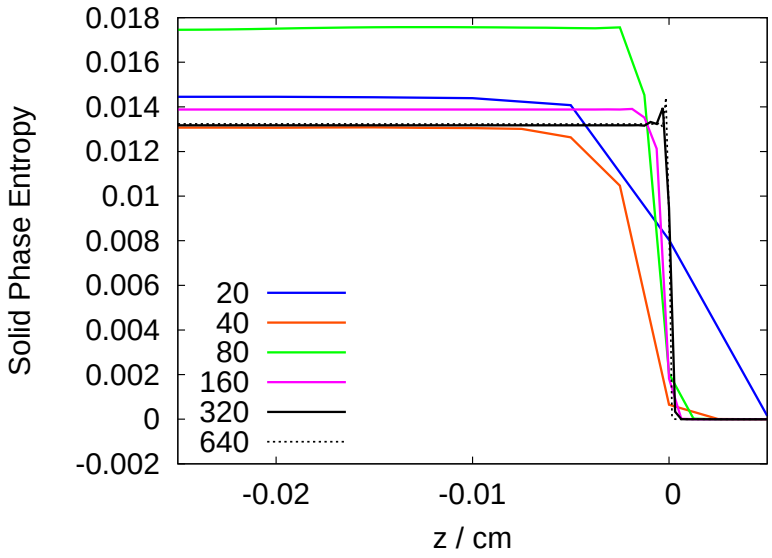

(a) Solid Phase Entropy.

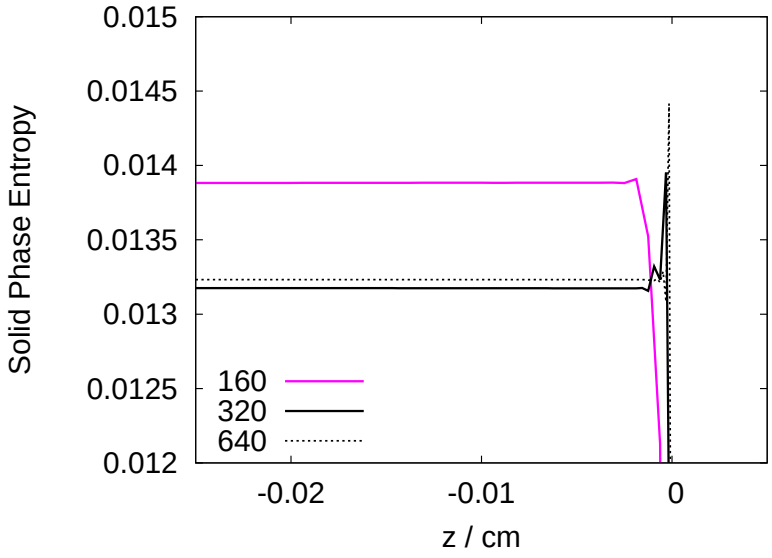

(b) Solid phase entropy with y-axis zoomed in.

Figure 5.4: One-dimensional simulations of PBX9502 - legend indicates resolution in cells/mm. The solution is in the shock-attached frame.

5.2.4 Stationary and Laboratory Frame Calculations

Using the EDC37 model a comparison between the stationary and laboratory frame DNS solutions were made. The finest resolutions of $[320, 640]$ $cells/mm$ were considered for these calculations.

It is clear from figure 5.5 that for the laboratory frame calculations the shock structure is spread over a greater number of cells compared to the stationary frame calculations. This is due to the numerical scheme being more diffuse when the shock propagates across the grid. Figure 5.6 shows that the moving calculations obtain a fractionally higher post-shock solid phase entropy, but the difference is negligible. The oscillations observed in the moving solutions are due to the numerical scheme and were discussed in section 4.5.7. As the shock moves across the grid the shock structure changes and generates numerical noise, resulting in the oscillations. Their impact on the solution is negligible.

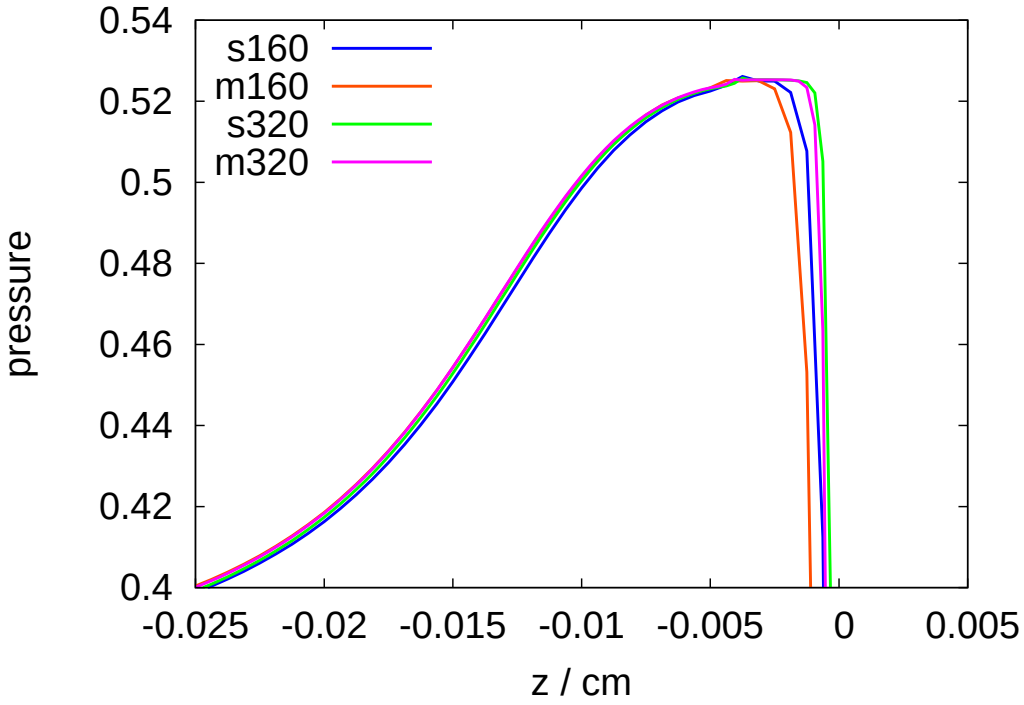

Figure 5.5: Pressure for stationary and lab frame shocks for different resolutions for EDC37. The legend indicates the reference frame of the solution (s: static, m: moving) and the resolution in cells/mm.

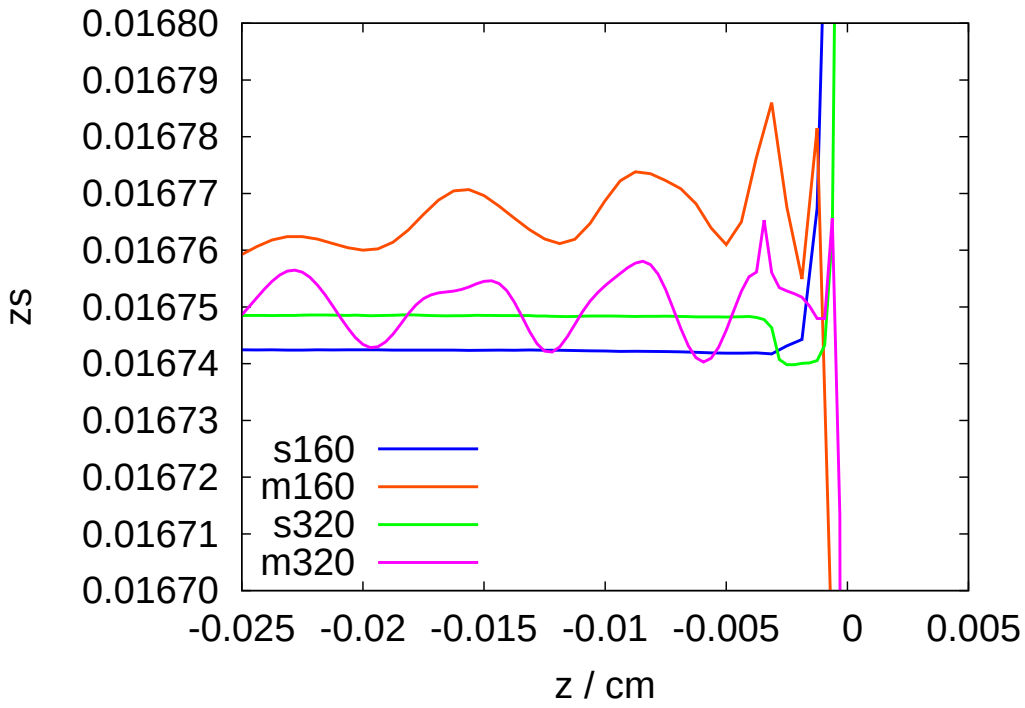

Figure 5.6: Entropy for stationary and lab frame shocks for different resolutions for EDC37. The legend indicates the reference frame of the solution (s: static, m: moving) and the resolution in cells/mm.

5.2.5 DNS compared with Steady State ZND Model

A direct comparison between the solutions from the high resolution DNS and the steady ZND model were made. Moreover a comparison between the DNS solutions with and without AMR was made for EDC37.

The detonation speeds obtained via the DNS and steady state model are summarised in table 5.4 which shows that the detonation velocities obtained from the steady state ZND code are in excellent agreement. It was found that the same detonation velocity was obtained in the DNS calculations, independent of the choice of resolution. This is because the scheme is strictly conservative in this case, which means that the final state is independent of the solution between the shock and the end of the reaction zone.

Explosive	ZND / $cm\,\mu s^{-1}$	DNS /$cm\,\mu s^{-1}$
EDC37	0.87693	0.87695
PBX9502	0.75974	0.75970

Table 5.4: Comparison between the detonation velocity obtained from the steady state ZND model and DNS for two CREST explosive models.

Figures 5.7 and 5.8 show that the structure through the reaction zone from the DNS calculations are in excellent agreement with those from the steady state code for EDC37. Figures 5.9(a) and 5.9(b) show that when using AMR the solution structure is unaffected and near identical solutions are obtained.

EDC37

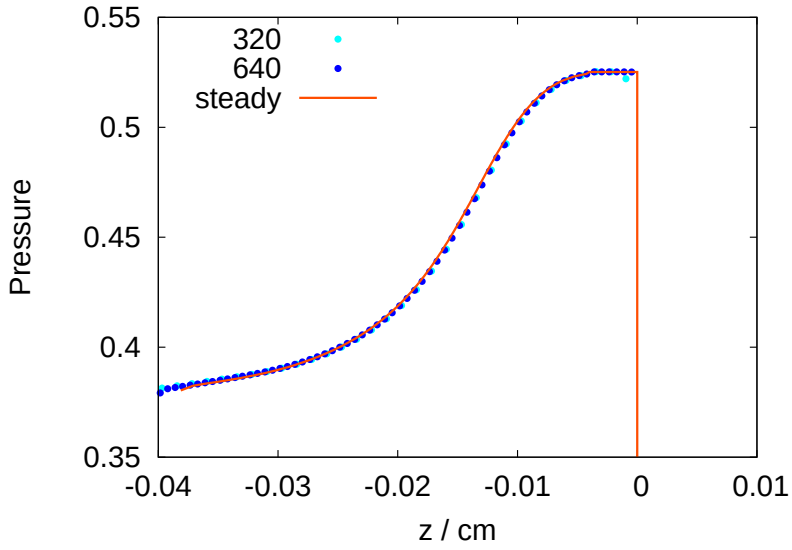

(a) Pressure.

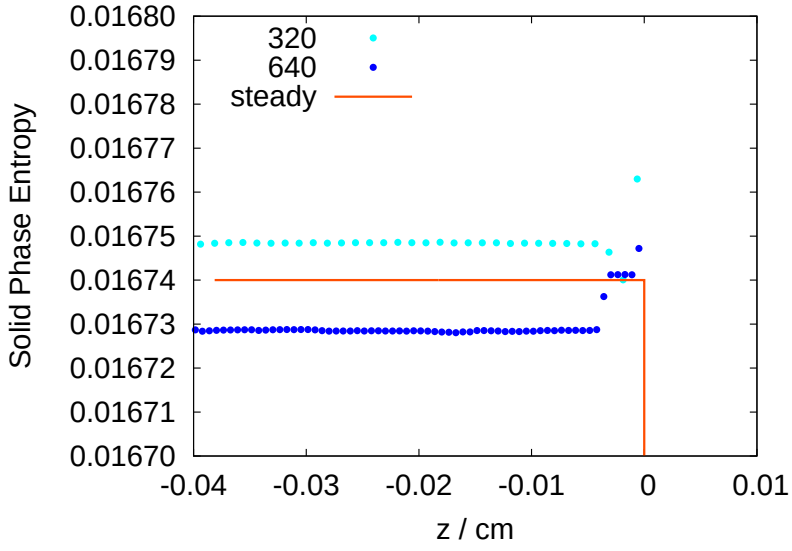

(b) Solid Phase Entropy.

Figure 5.7: One-dimensional simulations of EDC37 comparing DNS with steady state ZND model. Legend indicates resolution in cells/mm and steady state solution.

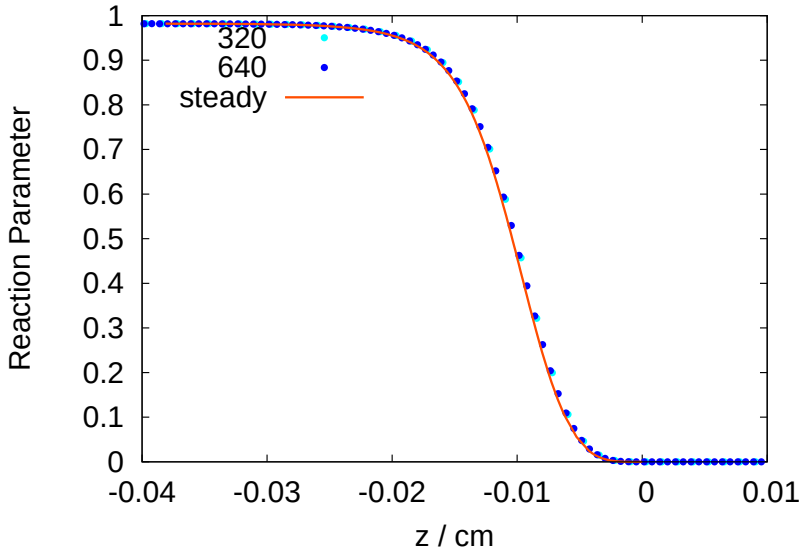

(a) Reaction Parameter.

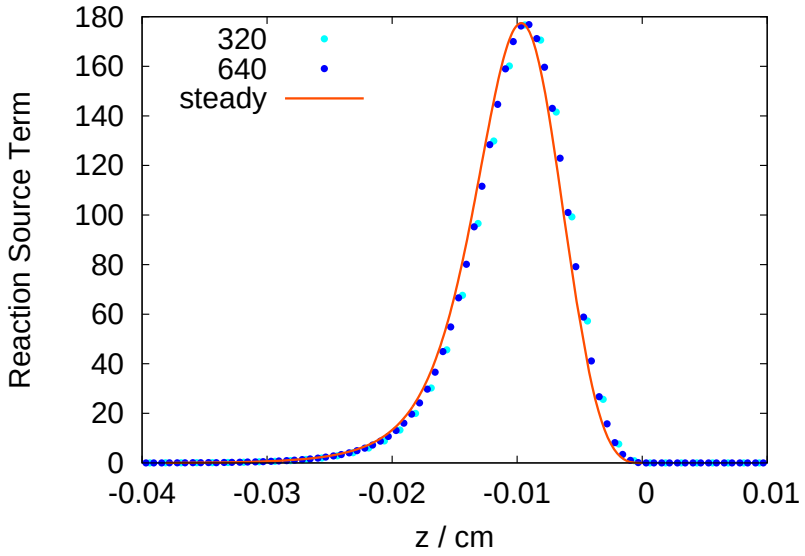

(b) Reaction Source Term.

Figure 5.8: One-dimensional simulations of EDC37 comparing DNS with steady state ZND model. Legend indicates resolution in cells/mm and steady state solution.

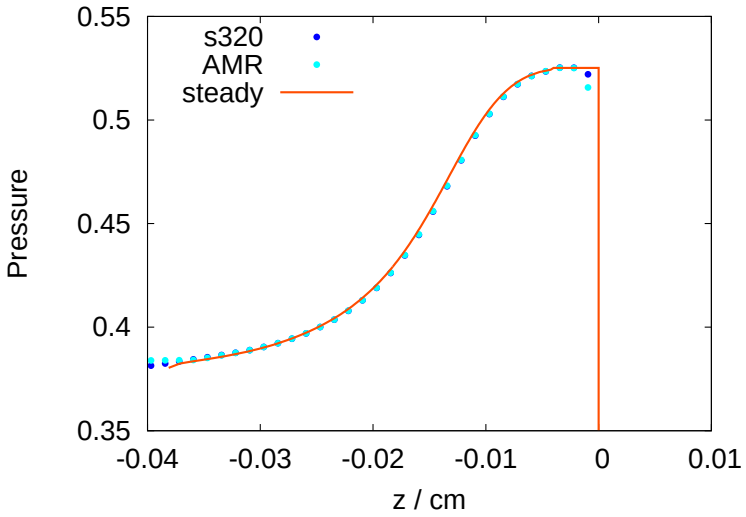

(a) Pressure.

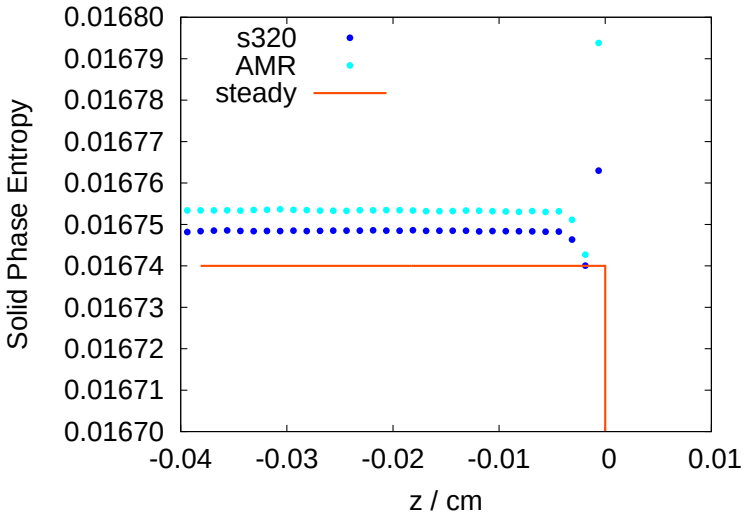

(b) Solid Phase Entropy.

Figure 5.9: One-dimensional simulations of EDC37 comparing DNS with uniform grid ($s320$) and adaptive mesh refinement (AMR) at a resolution of $320\,cells/mm$. The solution from the ZND model ($steady$) is included for reference.

PBX9502

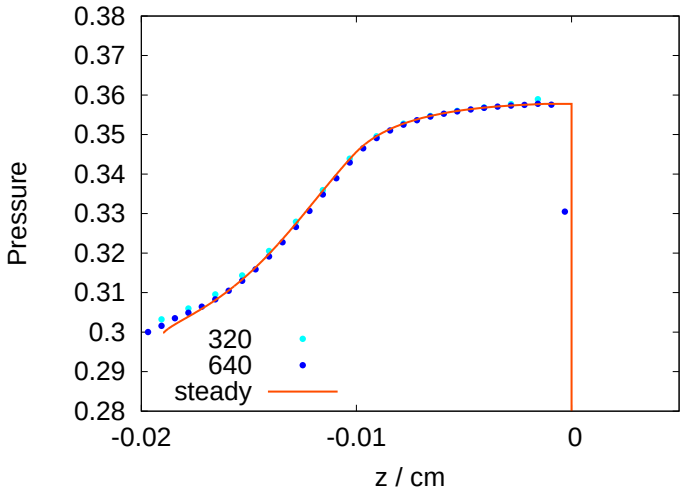

(a) Pressure.

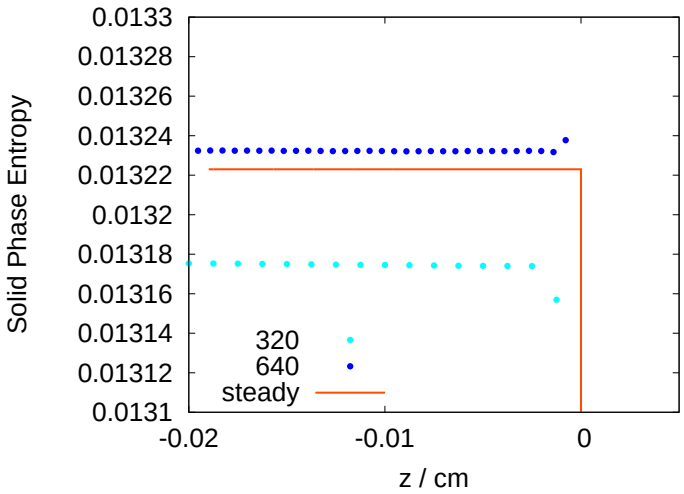

(b) Solid Phase Entropy.

Figure 5.10: One-dimensional simulations of PBX9502 comparing DNS with steady state ZND model. Legend indicates resolution in cells/mm and steady state solution.

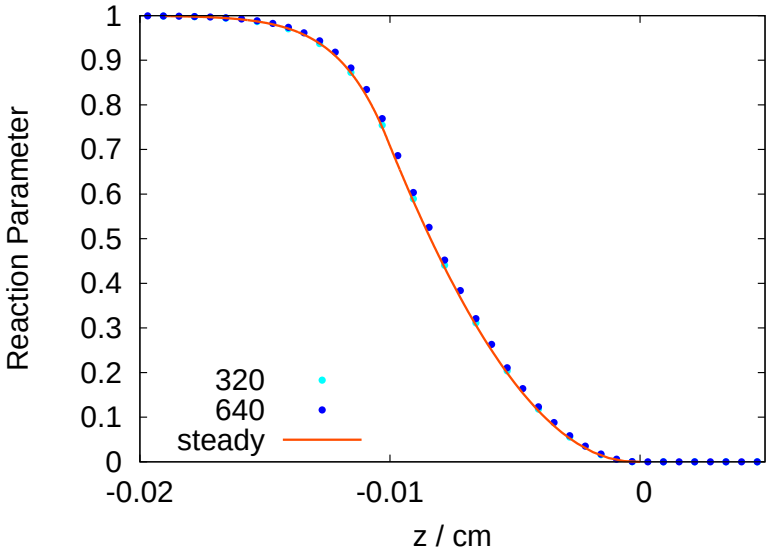

(a) Reaction Parameter.

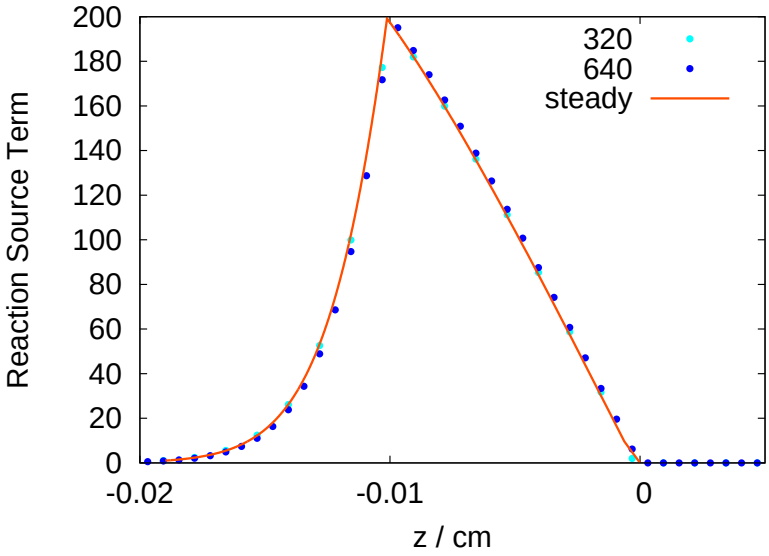

(b) Reaction Source Term.

Figure 5.11: One-dimensional simulations of PBX9502 comparing DNS with steady state ZND model. Legend indicates resolution in cells/mm and steady state solution.

5.3 Two-Dimension Rate-Stick Calculations

5.3.1 Introduction

As discussed in chapter 1 size effect curves (the relationship between detonation velocity and the radius of the rate-stick) are used to calibrate the empirical constants in the reaction rate equations. DNS calculations are performed and compared to experimental data and the reaction rate coefficients are then adjusted until the calculations match the data to a desired accuracy.

High resolution calculations are computationally expensive (order of hours for a single rate-stick simulations) and obtaining accurate fits to experimental data can require thousands of simulations. It is therefore desirable to find a more computationally efficient way of computing accurate diameter effect curves.

Approximate 2D detonation models, such as DSD and SSA, offer dramatic reductions in computational expense (diameter effect curves can be obtained in minutes). However, DSD has been shown to systematically underpredict the detonation velocity [30]. The SSA has been shown to be able to accurately match DNS calculations for a power law reaction rate with a polytropic equation of state. However, it has yet to be tested with a real explosive equation of state and a reaction rate that is not maximal at the shock, as in the case of CREST.

Unconfined rate-stick calculations were performed for both EDC37 and PBX9502 explosives using the axisymmetric Euler equations. The numerical domain was rectangular in (r, z) coordinates with the explosive in $0 < r < 1$ and a non-reacting, low density, confiner in $1 < r < 2$. The reaction in the confiner was switched off using an advected scalar that was set to unity in the reacting explosive and zero in the confiner. It has been shown that with low density inert confiner the explosive propagates effectively

unconfined [51]. The confiner density for the EDC37 calculations was $\rho_c = 0.9\, g/cm^3$ and for PBX9502 $\rho_c = 1.5\, g/cm^3$. The boundary conditions were symmetric on $r = 0$, free at the base of the explosive and at the edge of the confiner, and a fixed inflow boundary at the top of the explosive was implemented such that solutions could be transformed from the laboratory frame if desired.

The radius of the explosive was varied via a rate-constant multiplying the reaction source terms. Varying the magnitude of the rate-constant would vary the physical radius of the rate-stick but retain $R = 1$ in the simulation.

The detonation was initiated using a high pressure region at the base of the explosive at $0 < z < 2$. The detonation was allowed to propagate for a long time (at least $z >= 10$) until a steady state was obtained.

The z coordinate of the shock front, on axis, was tracked as a function of time. A linear fit of the $z - t$ data was used to compute the detonation velocity.

5.3.2 Resolution Study

As in the resolution study for the one-dimensional simulations, a similar resolution study was performed for a rate-stick of EDC37 with $r = 0.67$cm. The results of the study are summarised in table 5.5 and show that a resolution of 320 cells/mm is required to obtain well converged results for solid phase entropy and the detonation velocity. This corresponds to 69 cells in the reaction zone which agrees with previous studies where it was found that 50 cells were required in the reaction zone to obtain converged results [28].

There is a transition, between 80 cells/mm and 160 cells/mm at which there is no reaction (i.e. solid and gas mixture) inside the shock structure. Recall the explosive is treated as solid phase only for $\lambda < 0.02$ and hence the shock is well captured, in

terms of post-shock entropy, for resolutions at which the shock is solid phase only. This highlights the importance of ensuring there is no reaction through the shock so that the entropy of the shocked solid is captured accurately.

It is interesting to note that λ_{max} varies with resolution for the lower resolution calculations. This is because the extent of the reaction is dependent upon the magnitude of the solid phase entropy and there is no guarantee that there will be a complete reaction (i.e. $\lambda = 1$). This is not a feature observed in power law type reaction rates where the reaction will always go to completion.

Resolution	Entropy $/10^{-2} Mbar\, g/cm^3$	λ_{max}	$D/cm\mu s^{-1}$	CIRZ	λ_{shk}
20	0.85	0.856	0.768	6	0.65
40	1.23	0.907	0.810	9	0.40
80	1.33	0.928	0.809	17	0.05
160	1.27	0.912	0.801	34	0.005
320	1.25	0.911	0.798	69	0.002
640	1.24	0.910	0.797	140	0.001

Table 5.5: Properties of axial solution as a function of numerical resolution (cells/mm) for EDC37 with $r = 0.67$cm. Entropy refers to the unreacted equation of state, λ_{max} is the maximal value of the reaction progress variable, D is the detonation velocity, CIRZ is the Cells in Reaction Zone and is the number of cells on the finest level where reaction rate is significant (as defined by AMR criteria), λ_{shk} is the value of λ at the downstream end of the shock structure.

5.3.3 Galilean Invariance

The reactive Euler equations 2.1-2.4, on page 10, are Galilean invariant and thus it may be expected that the detonation velocity would be invariant, also. Using the EDC37 model and rate-stick of radius $r = 0.67cm$ the inflow velocity at the top of the domain, V_{in}, was varied from $0.0 - 0.7\,cm\,\mu s^{-1}$. The detonation velocity was computed by calculating the propagation speed, on axis, and adding the inflow velocity.

The results are summarized in table 5.6, which shows that for moderately low inflow velocities ($V_{in} < D/2$) the results obtained are Galilean invariant when considering the detonation velocity alone. However, for $V_{in} > D/2$ the computed detonation velocity increases. This may be due to λ_{max} increasing as the inflow velocity increases. The quantitative difference in the solutions for low inflow velocity and high inflow velocity is shown in figure 5.12. For the laboratory frame calculation ($V_{in} = 0$ in the figure) the profile of the solid phase entropy is monotonically increasing at the shock and is essentially constant behind it. There are some low amplitude oscillations in the reaction zone, which are an artefact of the shock-capturing scheme. For the calculation with a significant Galilean shift ($V_{in} = 0.5$) there is a significant spike in the entropy inside the shock structure, which then decreases to the same approximate magnitude as that of the laboratory calculation. There is a also a kink in the entropy, slightly downstream of the shock, which occurs at the point where the mixture of solid and gas phase is first initialised. This higher magnitude entropy then remains constant throughout the reaction zone. The higher magnitude entropy results in λ_{max} increasing and more energy to support the detonation wave being released. This is also evident in figure 5.13 where the reaction source term is significantly higher where maximal reaction occurs when an inflow velocity is used. The second kink in the entropy profile may be due to the numerical interpolation scheme in the second order calculations.

Figure 5.14 shows that the pressure profiles are very similar in both reference frames, although the pressure at the shock is marginally higher for $V_{in} = 0.5$.

The results of this investigation suggest that applying a small Galilean shift to the axial velocity does not affect the calculated detonation wave speed. This could reduce the computational time of DNS calculations as one would require a smaller domain. However, care must be taken as increasing the magnitude of the Galilean shift can introduce errors.

Inflow Velocity / $cm\mu s^{-1}$	λ_{max}	D / $cm\mu s^{-1}$
0	0.913	0.8012
0.1	0.913	0.8005
0.2	0.913	0.8003
0.3	0.914	0.8011
0.4	0.920	0.8037
0.5	0.925	0.8059
0.6	0.927	0.8067
0.7	0.929	0.8077

Table 5.6: Table indicating how the computed detonation velocity varies as a function of inflow velocity for EDC37 at a resolution of 160 cells/mm. The extent of reaction is also indicated.

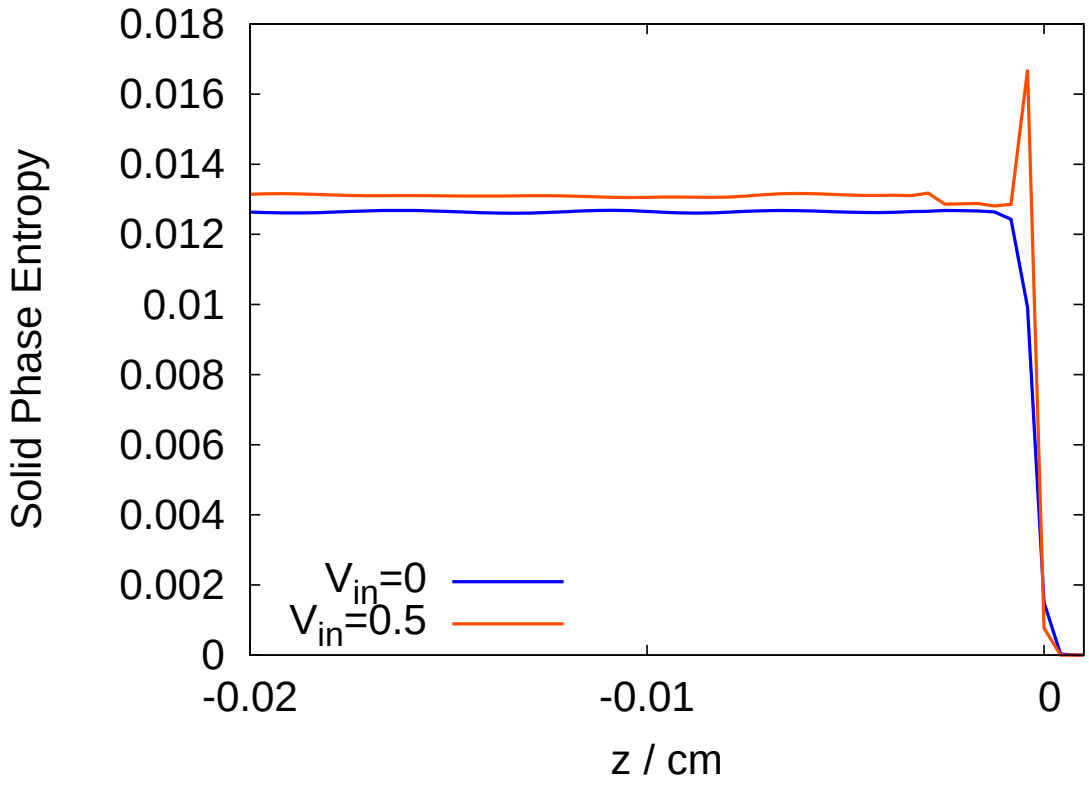

Figure 5.12: Solid Phase Entropy on axis for EDC37 with different inflow velocities. The resolution was 160 cells/mm and $r = 0.67$cm.

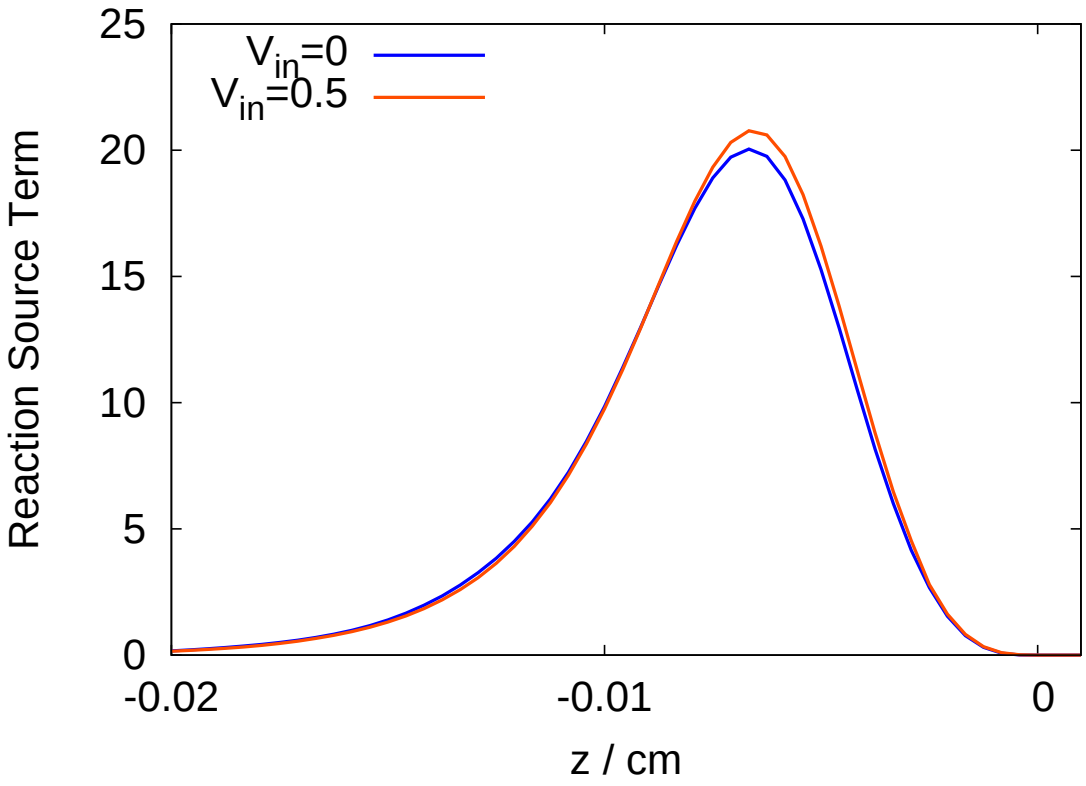

Figure 5.13: Reaction Source term on axis for EDC37 with different inflow velocities. The resolution was 160 cells/mm and $r = 0.67$cm.

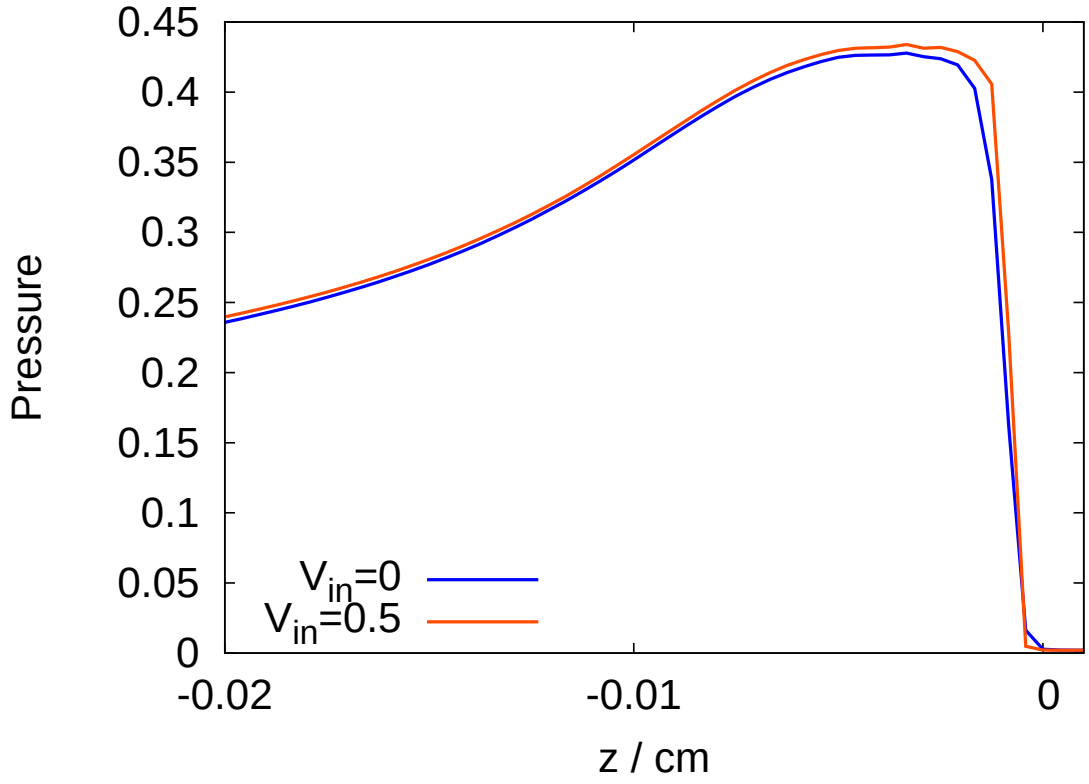

Figure 5.14: Pressure on axis for EDC37 with different inflow velocities. The resolution was 160 cells/mm and $r = 0.67$cm.

5.3.4 Comparison to previous data

Figure 5.15 shows the diameter effect curve calculated for PBX9502 at a resolution of 20 cells/mm. The results are compared with the previously published data at the same resolution [36]. The detonation velocities computed using the HLLC numerical scheme are less than those from previously published data. It should be noted that from the one-dimensional study in section 5.2.3 that for a resolution of 20 cells/mm there is significant reaction in the shock. For these calculations $\lambda >= 0.5$ immediately behind the shock and thus the shock and reaction zone length scales will be similar. This will affect the accuracy of the diameter effect curve. It was shown in table 5.5 that at least 160 cells/mm were required for converged results for a 2D calculation hence the reliability of comparing calculations at 20 cells/mm is questionable.

Diameter effect curves at higher resolutions are considered later in the thesis and are compared with the SSA and DSD models.

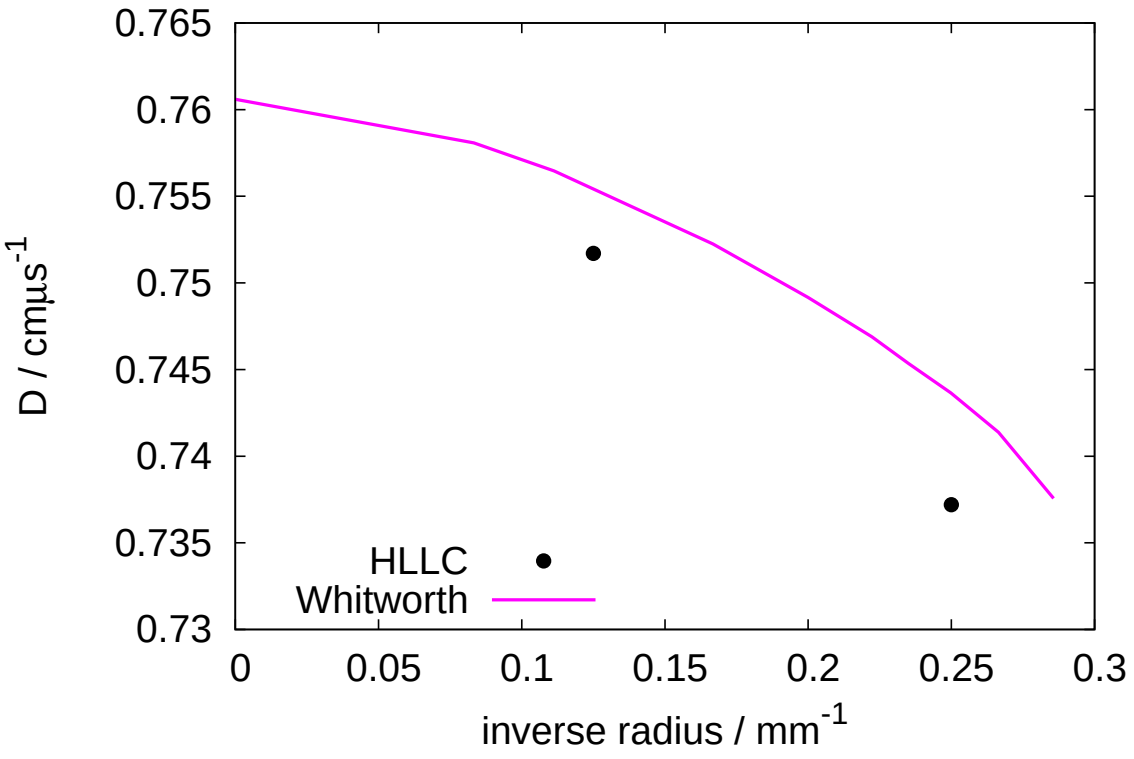

Figure 5.15: Diameter effect curve for PBX9502 with resolution of 20 cells/mm. The CJ velocity is $D_{CJ} = 0.760\, cm\, \mu s^{-1}$ for the HLLC data.

Chapter 6

Streamline Detonation Model - Straight Streamline Approximation

6.1 Introduction

A recent development in the modelling of steady state rate-stick detonations is the streamline model proposed by Watt et al [30]. The model uses a streamline based approach in which the solution along individual streamlines are combined to produce a complete solution to the detonation problem. This requires an assumption for the shape of the streamlines. As a first approximation the streamlines were assumed to be straight (Straight Streamline Approximation, SSA) and diverging. For the case of a polytropic EOS and a power law reaction rate the SSA model accurately calculated the diameter effect curves for both confined and unconfined rate-stick detonations (when compared to high resolution DNS calculations). Moreover, the failure diameter predicted by the SSA for ideal and non-ideal explosives closely matched those predicted by the DNS calculations, which is something the commonly used DSD model fails to capture

accurately [30].

Although the SSA worked well for the polytropic EOS and power law reaction rate it is unknown whether the SSA is an accurate model for a different EOS and reaction rates. In this chapter we investigate this for different forms of the EOS and reaction rate.

6.2 Governing Equations in Streamline Coordinates

6.2.1 Streamline Function

The starting point for deriving the flow equations is to define the compressible streamline function. In axisymmetric (r, z) coordinates the compressible streamline function ψ satisfies

$$\left(\frac{\partial \psi}{\partial z}\right)_r = r\rho u, \tag{6.1}$$

$$\left(\frac{\partial \psi}{\partial r}\right)_z = -r\rho v, \tag{6.2}$$

where u and v are the material velocities in the r and z directions respectively. Curves of constant ψ are streamlines. Dividing equation 6.1 by equation 6.2 we obtain

$$\left(\frac{\partial r}{\partial z}\right)_\psi = \frac{u}{v}, \tag{6.3}$$

which implies that the flow direction is everywhere tangent to the flow velocity, as expected for a stream function. Using the definition of the streamline function, the reactive Euler equations will be transformed from the axisymmetric coordinates (r, z) to a streamline based coordinates system (ψ, z) where the radial coordinate is now a function of the streamline function such that $r = r(\psi, z)$.

6.2.2 Material Derivative

We first consider the material derivative, defined in section 2.2, of a test function $f = f(r, z)$. In the shock-attached frame the partial time derivative vanishes and the advective term can be expanded in (r, z) coordinates to give

$$\frac{Df}{Dt} = \boldsymbol{u} \cdot \nabla = u \left(\frac{\partial f}{\partial r} \right)_z + v \left(\frac{\partial f}{\partial z} \right)_r .$$

Expanding the partial derivatives in terms of ψ and z, gives

$$\begin{aligned} \frac{Df}{Dt} =& u \left[\left(\frac{\partial f}{\partial \psi} \right)_z \left(\frac{\partial \psi}{\partial r} \right)_z + \left(\frac{\partial f}{\partial z} \right)_\psi \left(\frac{\partial z}{\partial r} \right)_z \right] \\ &+ v \left[\left(\frac{\partial f}{\partial \psi} \right)_z \left(\frac{\partial \psi}{\partial z} \right)_r + \left(\frac{\partial f}{\partial z} \right)_\psi \left(\frac{\partial z}{\partial z} \right)_r \right]. \end{aligned}$$

Here $\left(\frac{\partial z}{\partial r}\right)_z = 0$ as z is held constant, substituting for $\left(\frac{\partial \psi}{\partial z}\right)_r$ using 6.1 and for $\left(\frac{\partial \psi}{\partial r}\right)_z$ using 6.2 yields

$$\frac{Df}{Dt} = -\rho v u r \left(\frac{\partial f}{\partial \psi} \right)_z + \rho v u r \left(\frac{\partial f}{\partial \psi} \right)_z + v \left(\frac{\partial f}{\partial z} \right)_\psi .$$

Cancelling terms and dropping the test function f gives

$$\frac{D}{Dt} = v \left(\frac{\partial}{\partial z} \right)_\psi . \tag{6.4}$$

Following the same approach used to transform the material derivative to streamline based coordinates, the Euler equations can be transformed into (ψ, z) coordinate.

6.2.3 Continuity Equation

In axisymmetric coordinates the continuity equation 2.1 is

$$\frac{D\rho}{Dt} + \rho \left[\frac{u}{r} + \left(\frac{\partial u}{\partial r} \right)_z + \left(\frac{\partial v}{\partial z} \right)_r \right] = 0.$$

Substituting for the material derivative using 6.4 and expanding the partial derivatives in (ψ, z)

$$v\left(\frac{\partial \rho}{\partial z}\right)_{\psi} + \frac{\rho u}{r} + \rho\left[\left(\frac{\partial u}{\partial z}\right)_{\psi}\left(\frac{\partial z}{\partial r}\right)_{z} + \left(\frac{\partial u}{\partial \psi}\right)_{z}\left(\frac{\partial \psi}{\partial r}\right)_{z}\right] + \rho\left[\left(\frac{\partial v}{\partial \psi}\right)_{z}\left(\frac{\partial \psi}{\partial z}\right)_{r} + \left(\frac{\partial v}{\partial z}\right)_{\psi}\left(\frac{\partial z}{\partial z}\right)_{r}\right] = 0.$$

Substituting for $\left(\frac{\partial \psi}{\partial z}\right)_r$ and $\left(\frac{\partial \psi}{\partial r}\right)_z$ using 6.1 and 6.2

$$v\left(\frac{\partial \rho}{\partial z}\right)_{\psi} + \frac{\rho u}{r} - \rho^2 r v\left(\frac{\partial u}{\partial \psi}\right)_{z} + \rho^2 r u\left(\frac{\partial v}{\partial \psi}\right)_{z} + \rho\left(\frac{\partial v}{\partial z}\right)_{\psi} = 0.$$

Dividing by $-\rho^2 v^2$

$$-\frac{1}{\rho^2 v}\left(\frac{\partial \rho}{\partial z}\right)_{\psi} - \frac{u}{\rho v^2 r} + \frac{r}{v}\left(\frac{\partial u}{\partial \psi}\right)_{z} - \frac{r u}{v^2}\left(\frac{\partial v}{\partial \psi}\right)_{z} - \frac{1}{\rho v^2}\left(\frac{\partial v}{\partial z}\right)_{\psi} = 0.$$

Combining the first and last, and the third and fourth terms gives,

$$\frac{\partial}{\partial z}\left(\frac{1}{\rho v}\right)_{\psi} + r\frac{\partial}{\partial \psi}\left(\frac{u}{v}\right)_{z} = \frac{u}{\rho v^2 r}. \tag{6.5}$$

This gives the continuity equation in the streamline coordinate system.

6.2.4 r-Momentum

The radial component of the momentum equation 2.2 is

$$\rho\frac{Du}{Dt} + \left(\frac{\partial p}{\partial r}\right)_{z} = 0.$$

Applying the material derivative and expanding the partial derivative in r

$$\rho v\left(\frac{\partial u}{\partial z}\right)_{\psi} + \left[\left(\frac{\partial p}{\partial \psi}\right)_{z}\left(\frac{\partial \psi}{\partial r}\right)_{z} + \left(\frac{\partial p}{\partial z}\right)_{\psi}\left(\frac{\partial z}{\partial r}\right)_{z}\right] = 0.$$

Substituting for $\left(\frac{\partial\psi}{\partial r}\right)_z$ using 6.2 and noting that $\left(\frac{\partial z}{\partial r}\right)_z = 0$ gives

$$\rho v \left(\frac{\partial u}{\partial z}\right)_\psi - r\rho v \left(\frac{\partial p}{\partial \psi}\right)_z = 0,$$

which can be simplified to

$$\left(\frac{\partial u}{\partial z}\right)_\psi - r \left(\frac{\partial p}{\partial \psi}\right)_z = 0. \tag{6.6}$$

6.2.5 z-Momentum

We now consider the $z-$component of the momentum equation 2.2

$$\rho \frac{Du}{Dt} + \left(\frac{\partial p}{\partial z}\right)_r = 0.$$

Substituting for the material derivative and expanding the partial differential in z gives

$$\rho v \left(\frac{\partial v}{\partial z}\right)_\psi + \left[\left(\frac{\partial p}{\partial \psi}\right)_z \left(\frac{\partial \psi}{\partial z}\right)_r + \left(\frac{\partial p}{\partial z}\right)_\psi \left(\frac{\partial z}{\partial z}\right)_r\right] = 0,$$

and substituting for $\left(\frac{\partial\psi}{\partial z}\right)_r$ using 6.1 which can be rearranged to give

$$\rho v \left(\frac{\partial v}{\partial z}\right)_\psi + r\rho u \left(\frac{\partial p}{\partial \psi}\right)_z + \left(\frac{\partial p}{\partial z}\right)_\psi = 0. \tag{6.7}$$

6.2.6 Energy and Reaction Rate Equation

The energy equation 2.3 and reaction rate equation 2.4 are transformed via a trivial application of the material derivative. The resulting equations are

$$\left(\frac{\partial e}{\partial z}\right)_\psi = \frac{p}{\rho^2}\left(\frac{\partial \rho}{\partial z}\right)_\psi \tag{6.8}$$

$$\left(\frac{\partial \lambda}{\partial z}\right)_\psi = \frac{W}{v}. \tag{6.9}$$

6.2.7 Governing Equations

Combining the transformed equations for mass, r-momentum, z-momentum, energy and reaction rate yields set of governing equations in streamline coordinates

$$\frac{\partial}{\partial z}\left(\frac{1}{\rho v}\right)_{\psi} + r\frac{\partial}{\partial \psi}\left(\frac{u}{v}\right)_{z} = \frac{u}{\rho v^2 r}. \tag{6.10}$$

$$\left(\frac{\partial u}{\partial z}\right)_{\psi} = r\left(\frac{\partial p}{\partial \psi}\right)_{z}. \tag{6.11}$$

$$\left(\frac{\partial p}{\partial z}\right)_{\psi} + \rho v\left(\frac{\partial v}{\partial z}\right)_{\psi} + r\rho u\left(\frac{\partial p}{\partial \psi}\right)_{z} = 0. \tag{6.12}$$

$$\left(\frac{\partial e}{\partial z}\right)_{\psi} - \frac{p}{\rho^2}\left(\frac{\partial \rho}{\partial z}\right)_{\psi} = 0, \tag{6.13}$$

$$\left(\frac{\partial \lambda}{\partial z}\right)_{\psi} = \frac{W}{v}. \tag{6.14}$$

In present form equations 6.10-6.14 are not straightforward to integrate and must be manipulated into a suitable form to solve. Using an approach similar to that of section 2.4.2 the equations will be reduced down to a single master equation in the axial flow velocity v - coupled to the reaction rate equation.

6.2.8 Master equation in v

Reducing the governing equations into a master in the flow velocity involves successive substitutions of the energy and momenta equations into the continuity equation. Initially we begin with the energy equation 6.13. In section 3.3.1 it was shown that the energy equation can be coupled to the reaction rate equation 6.14 to obtain an expression relating the differentials in ρ, p and λ of the form

$$c^2 d\rho = dp + Q d\lambda\,, \tag{6.15}$$

where Q depends upon the equation of state. Next we consider the continuity equation 6.10, expanding the partial differential in z

$$r\frac{\partial}{\partial\psi}\left(\frac{u}{v}\right)_z - \frac{1}{\rho^2 v}\left(\frac{\partial\rho}{\partial z}\right)_\psi - \frac{1}{\rho v^2}\left(\frac{\partial v}{\partial z}\right)_\psi = \frac{u}{\rho v^2 r}.$$

Substituting for u/v using 6.3

$$r\frac{\partial}{\partial\psi}\left(\left(\frac{\partial r}{\partial z}\right)_\psi\right)_y - \frac{1}{\rho^2 v}\left(\frac{\partial\rho}{\partial z}\right)_\psi - \frac{1}{\rho v^2}\left(\frac{\partial v}{\partial z}\right)_\psi = \frac{1}{\rho v r}\left(\frac{\partial r}{\partial z}\right)_\psi.$$

This expression can be rearranged for $\left(\frac{\partial\rho}{\partial z}\right)_\psi$

$$\left(\frac{\partial\rho}{\partial z}\right)_\psi = \rho^2 v r\left(\frac{\partial^2 r}{\partial\psi\partial z}\right) - \frac{\rho}{v}\left(\frac{\partial v}{\partial z}\right)_\psi - \frac{\rho}{r}\left(\frac{\partial r}{\partial z}\right)_\psi, \tag{6.16}$$

which gives us an equation in ρ. Next the the momenta equations are considered, direct substitution of 6.11 into 6.12 gives

$$\rho v\left(\frac{\partial v}{\partial z}\right)_\psi + \left(\frac{\partial p}{\partial z}\right)_\psi + \rho u\left(\frac{\partial u}{\partial z}\right)_\psi = 0,$$

substituting for u using 6.3

$$\rho v\left(\frac{\partial v}{\partial z}\right)_\psi + \left(\frac{\partial p}{\partial z}\right)_\psi + \rho v\left(\frac{\partial r}{\partial z}\right)_\psi \frac{\partial}{\partial z}\left(v\left(\frac{\partial r}{\partial z}\right)_\psi\right)_\psi = 0,$$

expanding the final term by use of the product rule

$$\rho v\left(\frac{\partial v}{\partial z}\right)_\psi + \left(\frac{\partial p}{\partial z}\right)_\psi + \rho v\left(\frac{\partial r}{\partial z}\right)_\psi\left[v\left(\frac{\partial^2 r}{\partial z^2}\right)_\psi + \left(\frac{\partial r}{\partial z}\right)_\psi\left(\frac{\partial v}{\partial z}\right)_\psi\right] = 0,$$

rearranging for $\left(\frac{\partial p}{\partial z}\right)_\psi$

$$\left(\frac{\partial p}{\partial z}\right)_\psi = -\rho v\left[1 + \left(\frac{\partial r}{\partial z}\right)_\psi^2\right]\left(\frac{\partial v}{\partial z}\right)_\psi - \rho v^2\left(\frac{\partial r}{\partial z}\right)_\psi\left(\frac{\partial^2 r}{\partial z^2}\right)_\psi, \tag{6.17}$$

which gives an equation in p. We can now proceed to substitute for the differentials in ρ and p using 6.16 and 6.17 into the energy equation 6.15

$$c^2\left(\rho^2 vr\left(\frac{\partial^2 r}{\partial\psi\partial z}\right)-\frac{\rho}{v}\left(\frac{\partial v}{\partial z}\right)_\psi-\frac{\rho}{r}\left(\frac{\partial r}{\partial z}\right)_\psi\right)=-\rho v\left[1+\left(\frac{\partial r}{\partial z}\right)_\psi^2\right]\left(\frac{\partial v}{\partial z}\right)_\psi - \rho v^2\left(\frac{\partial r}{\partial z}\right)_\psi\left(\frac{\partial^2 r}{\partial z^2}\right)_\psi + Q\left(\frac{\partial\lambda}{\partial z}\right)_\psi .$$

Moving terms in $\left(\frac{\partial v}{\partial z}\right)_\psi$ to the LHS

$$\left[-\frac{c^2\rho}{v}+\rho v\left(1+\left(\frac{\partial r}{\partial z}\right)_\psi^2\right)\right]\left(\frac{\partial v}{\partial z}\right)_\psi=\rho c^2\left[\frac{1}{r}\left(\frac{\partial r}{\partial z}\right)_\psi-\rho vr\left(\frac{\partial^2 r}{\partial\psi\partial z}\right)\right] - \rho v^2\left(\frac{\partial r}{\partial z}\right)_\psi\left(\frac{\partial^2 r}{\partial z^2}\right)_\psi+Q\left(\frac{\partial\lambda}{\partial z}\right)_\psi$$

then multiplying by $\frac{v}{\rho}$

$$\left[v^2\left(1+\left(\frac{\partial r}{\partial z}\right)_\psi^2\right)-c^2\right]\left(\frac{\partial v}{\partial z}\right)_\psi=c^2 v\left[\frac{1}{r}\left(\frac{\partial r}{\partial z}\right)_\psi-\rho vr\left(\frac{\partial^2 r}{\partial\psi\partial z}\right)\right] - v^3\left(\frac{\partial r}{\partial z}\right)_\psi\left(\frac{\partial^2 r}{\partial z^2}\right)_\psi+\frac{Qv}{\rho}\left(\frac{\partial\lambda}{\partial z}\right)_\psi . \quad (6.18)$$

We can substitute for ρvr using 6.2 to get an alternative reduced equation

$$\left[v^2\left(1+\left(\frac{\partial r}{\partial z}\right)_\psi^2\right)-c^2\right]\left(\frac{\partial v}{\partial z}\right)_\psi=c^2 v\left[\frac{1}{r}\left(\frac{\partial r}{\partial z}\right)_\psi+\left(\frac{\partial r}{\partial\psi}\right)_z^{-1}\left(\frac{\partial^2 r}{\partial\psi\partial z}\right)\right] -v^3\left(\frac{\partial r}{\partial z}\right)_\psi\left(\frac{\partial^2 r}{\partial z^2}\right)_\psi-\left(\frac{\partial r}{\partial\psi}\right)_z^{-1}Qv^2\left(\frac{\partial\lambda}{\partial z}\right)_\psi . \quad (6.19)$$

Equation 6.18 is a partial differential equation for v which is coupled to the differential equation in λ. It can be used with 6.16 and 6.17 to obtain differential equations for ρ

and p. If the streamline shapes $r(\psi, z)$ were known *a priori* then the master equation could be solved, subject to boundary appropriate boundary conditions. However, as the streamlines shapes are not known an ansatz must be made on their shape.

6.3 Straight Streamline Approximation

6.3.1 Streamline Ansatz

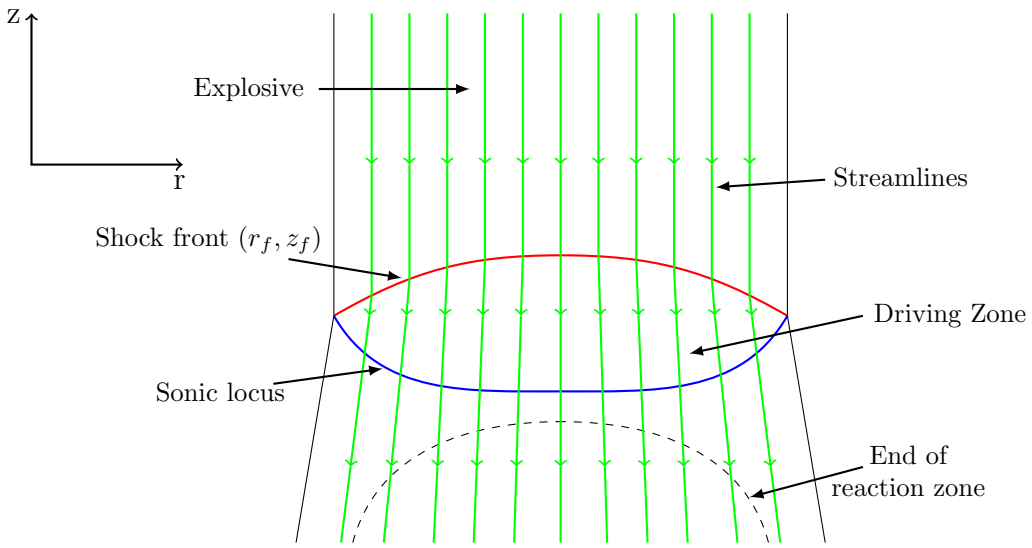

Figure 6.1: Schematic of a steady-state detonation. In the shock attached frame the unreacted explosive flows into the shock wave in the z-direction. The SSA assumes that the flow behind the shock has straight but diverging streamlines. The streamlines intersect the shock at the point (r_f, z_f). The flow speed in the shock frame increases as the chemical reaction proceeds and goes sonic at the sonic locus.

The simplest assumption one can make of the streamlines shapes is that they are

straight as shown in figure 6.1. In the shock-attached frame the streamlines propagate toward the shock front with the detonation velocity, D_0. At the streamline-shock intersection point (r_f, z_f) the streamline is deflected by the curved shock. The streamline is then assumed to remain straight through the detonation driving zone and beyond the sonic locus.

To determine the streamline function equation 6.2 is integrated to give

$$\psi = \frac{1}{2} r_f^2 \rho_0 D_0, \tag{6.20}$$

A streamline at radius r_f intersects the shock front at $z = z_f$ as shown in figure 6.1. From the streamline function 6.20 we have

$$\left(\frac{\partial r_f}{\partial \psi}\right)_{z_f} = \frac{1}{\rho_0 D_0 r_f}. \tag{6.21}$$

With this we can write the streamline shape, behind the shock, as

$$r = r_f + F(\psi)\,(z - z_f)\,, \tag{6.22}$$

where $F(\psi)$ is the slope of the streamline and is defined

$$F(\psi) = \left(\frac{\partial r}{\partial z}\right)_{\psi} = \frac{u_f}{v_f}, \tag{6.23}$$

where u_f and v_f are the radial and axial flow velocities immediately behind the shock. From equation 6.22 we also have

$$\left(\frac{\partial^2 r}{\partial z^2}\right)_{\psi} = 0, \tag{6.24}$$

which is a direct result of the assumption that the streamlines are straight. With the streamline function determined we can compute the partial derivatives $\left(\frac{\partial r}{\partial \psi}\right)_z$ and $\left(\frac{\partial^2 r}{\partial \psi \partial z}\right)$ required to solve the governing equations along each streamline. They are

related to the streamline function by use of the chain rule. Taking the derivative of the streamline shape 6.22 with respect to ψ

$$\left(\frac{\partial r}{\partial \psi}\right)_z = \left(\frac{\partial r_f}{\partial \psi}\right)_z + \left(\frac{\partial F}{\partial \psi}\right)_z (z - z_f) - F(\psi)\left(\frac{\partial z_f}{\partial \psi}\right)_z. \tag{6.25}$$

Parameterising the shock such that $z_f = z_f(r_f)$, the derivative $\left(\frac{\partial z_f}{\partial \psi}\right)_z$ can be related to shock parameterisation using the chain rule such that

$$\left(\frac{\partial r}{\partial \psi}\right)_z = \frac{dr_f}{d\psi} + \frac{dF}{d\psi}(z - z_f) - F(\psi) z_f' \frac{dr_f}{d\psi}, \tag{6.26}$$

where the partial derivatives are replaced by total derivatives as r_f, z_f and $F(\psi)$ depend only upon ψ. Here z_f' is the slope of the shock where it intersects with the streamline. Taking the derivative of 6.26 we have

$$\left(\frac{\partial^2 r}{\partial \psi \partial z}\right) = \frac{dF}{d\psi}. \tag{6.27}$$

As the streamline slope F is a function of the shock slope z_f' we can apply the chain rule to obtain

$$\frac{dF}{d\psi} = \left(\frac{\partial F}{\partial z_f'}\right) z_f'' \frac{dr_f}{d\psi}.$$

Using this expression and substituting for $\frac{dr_f}{d\psi}$ using equation 6.21 gives

$$\left(\frac{\partial r}{\partial \psi}\right)_z = \frac{1}{\rho_0 D_0 r_f}\left[1 + \frac{dF}{dz_f'} z_f''(z - z_f) - F z_f'\right]. \tag{6.28}$$

It immediately follows from equation 6.26 that

$$\left(\frac{\partial^2 r}{\partial \psi \partial z}\right) = \frac{dF}{d\psi} = \frac{\frac{dF}{dz_f'} z_f''}{\rho_0 D_0 r_f}. \tag{6.29}$$

Here $\left(\frac{\partial F}{\partial z_f'}\right)$ must be determined from the shock relations for each streamline. Equations 6.26 and 6.29 show that the governing equations along the streamline will depend upon

the shock via the point intersection with streamline (r_f, z_f), the shock slope z'_f and the second derivative of the shock position z''_f, which is related to the shock front curvature. Thus, if the shock slope z'_f and location (z_f, r_f) are known then the unknown parameter is the shock front curvature z''_f. There will be a unique value of z''_f that solves the eigenvalue problem given by the master equation 6.19. With z''_f known this enables integration out along the shock surface to determine the complete detonation solution.

6.3.2 Equations on $r = 0$

Special care needs to be taken when integrating the master equation 6.19 on the axis $(r = 0)$. The first term on the RHS is

$$\frac{1}{r}\left(\frac{\partial r}{\partial z}\right)_\psi .$$

This is ill-defined and must be treated with care. There is no mention of how this is dealt with in the published literature [30]. However, we can consider the the behaviour of this term in the limit of $r \to 0$. Using L'Hopital's rule we have

$$\begin{aligned}
\lim_{r\to 0}\frac{1}{r}\left(\frac{\partial r}{\partial z}\right)_\psi &= \frac{\partial}{\partial r}\left(\frac{\partial r}{\partial z}\right)_\psi , \\
&= \frac{\partial}{\partial r}\left(F(\psi)\right)_z , \\
&= \left(\frac{\partial F}{\partial \psi}\right)_z \left(\frac{\partial \psi}{\partial r}\right)_z + \left(\frac{\partial F}{\partial z}\right)_\psi \left(\frac{\partial z}{\partial r}\right)_z , \\
&= \frac{dF}{d\psi}\left(\frac{\partial r}{\partial \psi}\right)_z^{-1} \\
&= \left(\frac{\partial^2 r}{\partial \psi \partial z}\right)\left(\frac{\partial r}{\partial \psi}\right)_z^{-1} . \qquad (6.30)
\end{aligned}$$

This term is identical to the second term appearing on the RHS of the master equation 6.19. This is the result we would expect due to having the extra dimensional curvature resulting from the axisymmetric equations.

6.4 Boundary Conditions

6.4.1 Charge centre and charge edge boundaries

We define the centre of the rate-stick to be at $r = 0$ as shown in figure 6.2. The slope of the shock front along the centre is then $z'_f = 0$ by symmetry and the streamline along the centre must be straight also ($F = 0$).

The boundary condition at the edge of the explosive is defined in terms of the shock slope. For an unconfined charge the post-shock flow velocity must be exactly sonic in shock-attached frame. This is because there is a transonic Prandtl-Meyer expansion attached to the shock at the charge edge [26]. As the post-shock flow conditions depend only upon z'_f there is a unique shock slope at which the post-shock streamline velocity will be exactly sonic. This gives a boundary condition for the edge of the charge based upon the shock slope.

For confined detonations the boundary condition is that the post-shock pressure and streamline deflection angle must match between the explosive and the confining material. The shock slope at which this occurs can be determined via a shock polar analysis [11]. For a given detonation velocity the post-shock pressure versus deflection angle is plotted for the explosive/confiner pair. Points of intersection indicate the shock slope at the boundary for the explosive.

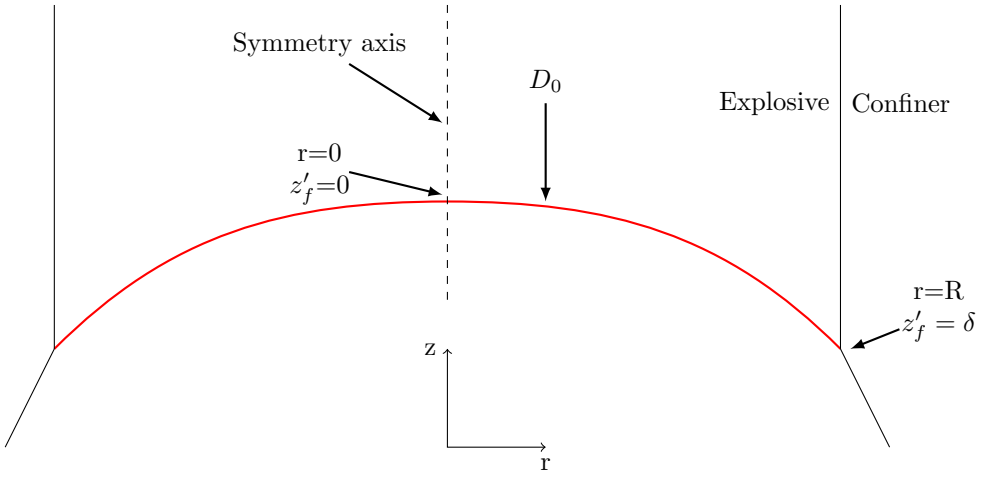

Figure 6.2: Schematic of shock front boundary conditions. The boundary conditions are based upon the shock slope z'_f. Along the centre-line ($r = 0$) the shock slope is zero ($z'_f = 0$) by symmetry. The shock slope δ at the explosive-confiner interface ($r = R$) is determined by a shock polar analysis.

6.4.2 Oblique Shock Relations

To determine the post-shock state for each streamline the oblique shock relations are utilised. The oblique shock relations are derived by considering the normal one-dimensional shock relations with an additional velocity component which is transverse to the shock front. This is shown in figure 6.3 where v_t is the transverse velocity and is perpendicular to the normal component of the initial velocity v_{n_0}. The oblique shock relations are [52]

$$\rho_1 v_{n_1} = \rho_0 v_{n_0}, \tag{6.31}$$

$$p_1 + \rho_1 v_{n_1}^2 = p_0 + \rho_0 v_{n_0}^2, \tag{6.32}$$

$$e_1(\rho_1, p_1) + \frac{p_1}{\rho_1} + \frac{1}{2} v_{n_1}^2 = e_0(\rho_0, p_0) + \frac{p_0}{\rho_0} + \frac{1}{2} v_{n_0}^2, \tag{6.33}$$

Here v_{n1} is the post-shock flow velocity normal to the shock front. Subscript 0 refers to the quiescent state and subscript 1 refers to the shock state. With the pre-shocked state of the explosive known equations 6.31-6.33 can be solved to determine the post-shock density, pressure and normal velocity.

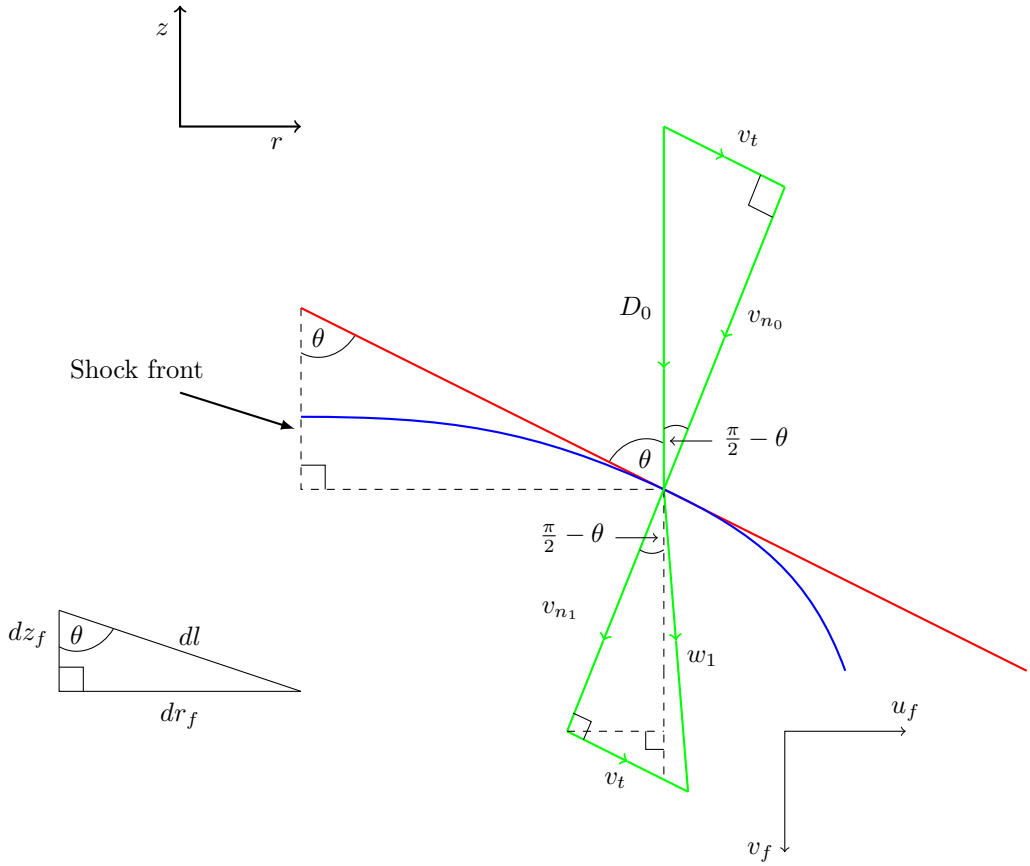

Figure 6.3: Schematic of an oblique shock. The flow has initial velocity D_0 in the axial direction with a component normal to the shock of speed v_{n0}. The shock is inclined at an angle θ relative to the incoming streamline. The post-shock flow velocity w_1 can be split into radial and axial components which determine the post-shock conditions for the flow in the governing equations.

The post-shock normal velocity can be combined with the transverse velocity to determine the velocity components in the r and z directions. First we relate the pre-shock velocities to the shock velocity D_0. From figure 6.3 it is clear that

$$v_{n_0} = D_0 \cos\left(\frac{\pi}{2} - \theta\right) = D_0 \sin\theta, \tag{6.34}$$

and

$$v_{n_1} = f(v_{n_0}) = f(D_0 \sin\theta), \tag{6.35}$$

where $f(v_{n_0})$ is the post-shock velocity normal to the shock.

The transverse velocity is given by

$$v_t = D_0 \sin\left(\frac{\pi}{2} - \theta\right) = D_0 \cos\theta. \tag{6.36}$$

To determine the post-shock flow velocities in the r and z directions, u_f and v_f. We have

$$v_f = v_{n_1} \sin\theta + v_t \cos\theta, \tag{6.37}$$

$$u_f = -v_{n_1} \cos\theta + v_t \sin\theta. \tag{6.38}$$

Next expressions for $\sin\theta$ and $\cos\theta$ are required in terms of the shock slope. This angle, which determines the obliqueness of the shock can be related to local shock slope at the streamline intersection. Consider the triangle on the left hand side of figure 6.3. The length dl is a differential increment along the shock surface whose slope is given by $\frac{dz_f}{dr_f}$. From this right-angled triangle we have

$$\sin\theta = \frac{dr_f}{dl},$$

substituting for dl in terms of dr_f and dz_f using Pythagoras' formula

$$\sin\theta = \frac{dr_f}{\left(dr_f^2 + dz_f^2\right)^{\frac{1}{2}}},$$

removing a factor of dr_f

$$\sin\theta = \frac{1}{\left(1+\left(\frac{dz_f}{dr_f}\right)^2\right)^{\frac{1}{2}}}. \tag{6.39}$$

Following a similar procedure we can determine an expression for $\cos\theta$ which is

$$\cos\theta = \frac{\frac{dz_f}{dr_f}}{\left(1+\left(\frac{dz_f}{dr_f}\right)^2\right)^{\frac{1}{2}}}. \tag{6.40}$$

Denoting the derivative $\frac{dz_f}{dr_f}$ as z'_f equations 6.39 and 6.40 become

$$\sin\theta = \frac{1}{\left(1+\left(z'_f\right)^2\right)^{\frac{1}{2}}}, \tag{6.41}$$

and

$$\cos\theta = \frac{z'_f}{\left(1+\left(z'_f\right)^2\right)^{\frac{1}{2}}}. \tag{6.42}$$

We can substitute the results from equations 6.41 and 6.42 into the flow velocities behind the shock given by 6.37 and 6.38. For the axial velocity equation 6.37 becomes

$$v_f = \frac{v_{n_1}}{\left(1+\left(z'_f\right)^2\right)^{\frac{1}{2}}} + \frac{v_t z'_f}{\left(1+\left(z'_f\right)^2\right)^{\frac{1}{2}}},$$

Substituting for v_t using equation 6.36 and writing with a common denominator gives

$$v_f = \frac{v_{n_1}\left(1+\left(z'_f\right)^2\right)^{\frac{1}{2}} + D_0\left(z'_f\right)^2}{\left(1+\left(z'_f\right)^2\right)}. \tag{6.43}$$

An similar expression can be deduced for the radial velocity given by

$$u_f = \frac{-v_{n_1} z'_f\left(1+\left(z'_f\right)^2\right)^{\frac{1}{2}} + D_0 z'_f}{\left(1+\left(z'_f\right)^2\right)}. \tag{6.44}$$

It is clear from equations 6.43 and 6.44 that the post-shock flow variables only depend upon the shock slope z'_f for a given upstream state. The pressure and density post-shock are determined as part of the solution to the normal shock relations, the transverse velocity has no affect on their magnitude.

6.5 Numerical Implementation

6.5.1 Solution Procedure

With an equation of state and reaction rate model specified, there is a relation between the detonation velocity D_0 and the charge radius R. If the charge radius is specified then an initial guess for D_0 can be made. The SSA equations are then solved for each streamline as we integrate from the charge edge (at $r = R$) along the shock surface until $r = 0$. If the detonation velocity is correct, then at $r = 0$ we will satisfy the boundary condition on the axis that $z'_f = 0$. If the boundary condition is not satisfied, the procedure can be repeated for a different value of D_0 until a value is found for which the boundary condition is satisfied. It should be noted that this method requires multiple integrations along the shock.

Alternatively, by specifying D_0, we can integrate from the charge axis ($r = 0$) along the shock surface until the post-shock flow becomes sonic. The charge radius is then given by the radius of the shock front $R = r_f$. This method requires integration along the shock surface once.

The second method, specifying D_0 and integrating out along the shock is preferred as the method of specifying R and calculating D requires multiple integrations along the shock surface. This will make the model more computationally expensive with no gain in accuracy. All computations were performed in this way.

For a given detonation velocity D_0 we have $(r_f = 0, z_f = 0, r = 0, z'_f = 0)$ on the central streamline. We can then determine the shock curvature z''_f for the central streamline by solving the master equation 6.18, coupled with equations 6.14, 6.16 and 6.17. With the shock curvature for that streamline determined we can integrate out along the shock using a Taylor expansion about the point (r_f, z_f) to determine the shock slope and location of the next streamline via

$$z_f^{n+1} = z_f^n + \frac{dz_f}{dr_f}^n \Delta r_f + \frac{1}{2}\frac{d^2 z_f}{dr_f^2}^n \Delta r_f^2, \tag{6.45}$$

$$\frac{dz_f}{dr_f}^{n+1} = \frac{dz_f}{dr_f}^n + \frac{d^2 z_f}{dr_f^2}^n \Delta r_f, \tag{6.46}$$

and

$$r_f^{n+1} = r_f^n + \Delta r_f. \tag{6.47}$$

The eigenvalue problem for z''_f is then solved again with the initial conditions given by the new coordinates and slope at the shock. The integration along the shock continues until the boundary shock slope is reached.

Computing the shock curvature z''_f requires solving the flow, along the streamline, between the shock and the sonic locus of the flow. At this point the generalised CJ conditions must be satisfied identically. An initial guess for z''_f is made (based on the previous streamline solution) and the numerical shooting method (as described in section 2.4.5 is used to vary z''_f until the generalised CJ conditions are satisfied.

Solving the detonation problem for different values of D_0, and thus different charge radii, gives a size-effect curve for a given explosive.

6.6 Polytropic EOS

To verify the implementation of the SSA diameter effect curves for unconfined rate-sticks were calculated for the polytropic equation of state and compared to previously published work. In this section the shock relations are presented and the boundary condition defining the charge edge is also derived.

6.6.1 Shock Relations, Boundary Conditions and Streamline Derivatives

The oblique shock relations can be solved analytically for the polytropic EOS. For a detonation velocity D_0, initial density $\rho_0 = 1$ and initial pressure $p_0 = 0$, the post-shock variables are

$$p_f = \frac{2D_0^2}{(\gamma+1)\left(1+\left(z_f'\right)^2\right)}, \tag{6.48}$$

$$\rho_f = \frac{\gamma+1}{\gamma-1}, \tag{6.49}$$

$$u_f = -\frac{2D_0 z_f'}{(\gamma+1)\left(1+\left(z_f'\right)^2\right)}, \tag{6.50}$$

$$v_f = -\frac{D_0\left(\gamma-1+(\gamma+1)\left(z_f'\right)^2\right)}{(\gamma+1)\left(1+\left(z_f'\right)^2\right)}. \tag{6.51}$$

The streamline function is given by u_f/v_f

$$F = \frac{2z_f'}{\gamma-1+(\gamma+1)(z_f')^2}. \tag{6.52}$$

We require the derivative of F with respect to z_f' to integrate the flow equations. Differentiating 6.52 with respect to z_f' gives

$$\left(\frac{\partial F}{\partial z_f'}\right) = \frac{2\left(\gamma-1-(\gamma+1)(z_f')^2\right)}{\left(\gamma-1+(\gamma+1)(z_f')^2\right)^2}. \tag{6.53}$$

With this result we are in a position to be able to integrate the model equations to obtain the shock curvature term z_f''. The Bernoulli equation can be used to determine expressions for the pressure, density and sound speed as a function of v and λ. The energy and momentum equations 6.11 - 6.13 can be combined to derive the Bernoulli equation for the polytropic EOS

$$\frac{\gamma p}{(\gamma-1)\rho} - \lambda q + \frac{1}{2}(u^2+v^2) = \frac{1}{2}D_0^2. \tag{6.54}$$

Substituting for u from equation 6.3 gives,

$$\frac{\gamma p}{(\gamma-1)\rho} - \lambda q + \frac{1}{2}\left(v^2\left(\frac{\partial r}{\partial z}\right)_\psi^2 + v^2\right) = \frac{1}{2}D_0^2,$$

which can be rearranged for the pressure such that

$$p = \frac{(\gamma-1)\rho}{2\gamma}\left[D_0^2 - v^2\left(1+\left(\frac{\partial r}{\partial z}\right)_\psi^2\right) + 2\lambda q\right].$$

Finally substituting for ρ using 6.2 gives,

$$p = -\frac{(\gamma-1)}{2\gamma v r}\left(\frac{\partial r}{\partial \psi}\right)_z^{-1}\left[D_0^2 - v^2\left(1+\left(\frac{\partial r}{\partial z}\right)_\psi^2\right) + 2\lambda q\right]. \tag{6.55}$$

This is an expression for p which is related to the streamline ansatz via $\left(\frac{\partial r}{\partial \psi}\right)_z^{-1}, \left(\frac{\partial r}{\partial z}\right)_\psi$ and to the two integrated variables v, λ. The pressure typically appears in power-law type reaction rates and thus is useful to compute along the streamline. For the polytropic EOS the adiabatic sound speed is

$$c^2 = \frac{\gamma p}{\rho}. \tag{6.56}$$

Substituting for p using 6.55 and ρ using 6.2 into this equation yields

$$c^2 = \frac{(\gamma-1)}{2}\left[D_0^2 - v^2\left(1+\left(\frac{\partial r}{\partial z}\right)_\psi^2\right) + 2\lambda q\right]. \tag{6.57}$$

With this the sound speed can be computed on a streamline for a given v and λ.

The boundary condition defining the charge edge is related to the shock slope z'_f. For an unconfined explosive the post-shock flow must be exactly sonic. We can write this condition as

$$u^2 + v^2 = c^2.$$

Substituting for the sound speed using 6.54 and 6.57 gives

$$u^2 + v^2 = \frac{(\gamma - 1)}{2}\left[D_0^2 - u^2 - v^2\right],$$

where $\lambda = 0$ is used as no reaction occurs through the shock. Moving the terms in u and v to the LHS gives

$$u^2 + v^2 = \frac{(\gamma - 1)}{(\gamma + 1)} D_0^2.$$

Substituting for u and v at the shock using 6.50 and 6.51 gives

$$\frac{D_0^2\left[(\gamma-1)^2 + (\gamma+1)^2\,(z'_f)^4 + 2\,(\gamma-1)\,(\gamma+1)\,(z'_f)^2 + 4(z'_f)^2\right]}{(\gamma+1)^2\left(1 + (z'_f)^2\right)^2} = \frac{(\gamma-1)}{(\gamma+1)} D_0^2,$$

which is a quadratic equation in $(z'_f)^2$. This equation can be solved to give

$$(z'_f)^2 = \frac{-1}{(\gamma+1)} \pm \frac{\gamma}{(\gamma-1)}.$$

The negative solution is rejected as this would yield complex values of z'_f. Using the positive solution and taking the square root of both sides yields the shock slope at the charge boundary

$$z'_f = -\sqrt{\frac{(\gamma+1)}{(\gamma-1)}}, \tag{6.58}$$

where the positive solution is rejected as the shock surface coordinate z_f is assumed to be decreasing.

If we consider the derivative of the streamline function $\frac{dF}{d\psi}$, given by equation 6.53, and set it equal to zero we have

$$\frac{2\left(\gamma - 1 - (\gamma+1)(z_f')^2\right)}{\left(\gamma - 1 + (\gamma+1)(z_f')^2\right)^2} = 0.$$

Solving this equation for z_f' gives

$$z_f' = -\sqrt{\frac{(\gamma+1)}{(\gamma-1)}}, \tag{6.59}$$

which is identical to the shock slope at which the flow is exactly sonic given by equation 6.58. This tells us that the shock slope boundary condition that determines the edge of the explosive coincides with the shock slope at which the streamline deflection is maximum. Integrating out further and decreasing shock slope beyond this point the streamlines would begin to converge and the assumptions of the SSA (i.e. diverging streamlines) would break down. It is therefore important to use a shock-polar analysis to determine where the maximal streamline deflection occurs. If the streamline deflection angle reaches a maximum, then the streamlines must curve to prevent them from converging.

6.6.2 Power Law Reaction Rate - Confirm Previous Results

Verification of the SSA numerical code was confirmed by replicating the results from previous calculations in [30] using a power law reaction rate of the form

$$\frac{d\lambda}{dt} = \alpha\, p^n\, (1-\lambda)^m\,, \tag{6.60}$$

where the rate constant m was set to 0.5 for all calculations; simulations were performed for $n = [0.5, 1.0, 1.7, 2.0]$ to match those from the previous calculations. Figure 6.4 shows that for $n = 0.0, 1.0$ the data previously published were reproduced accurately.

But for $n = 1.7, 2.0$ the detonation velocity was slighter larger than in Watt et al. However, the curves have the same trend, which suggests that the differences may be due to differences arising from the numerical methods used. Figures 6.5 and 6.6 show diameter effect curves obtained for different values of $\Delta z'_f$. Using a larger step in z'_f between streamlines both diameter effect curves shift to left and the results previously published can be recovered.

As the previously published data have been reproduced, the SSA code was verified and different EOS and reaction rates can be incorporated.

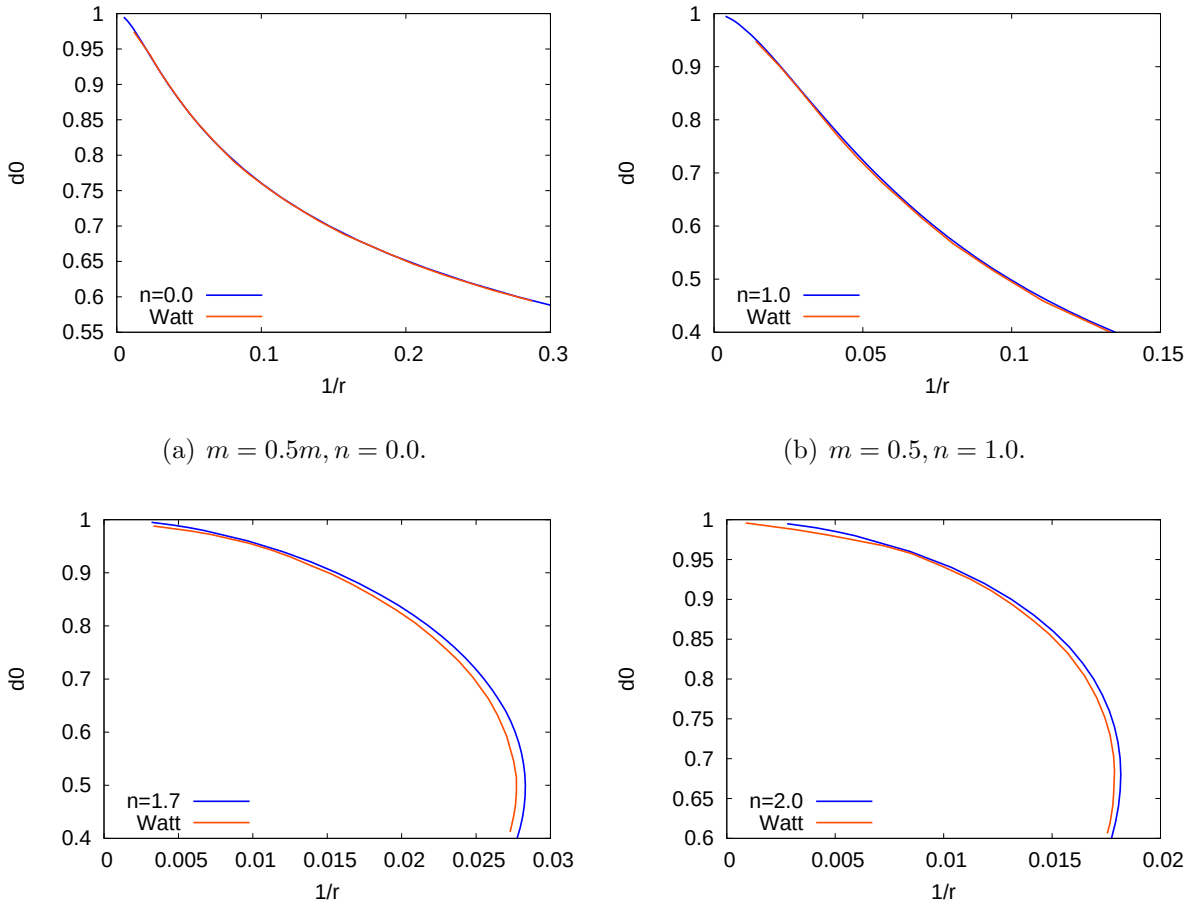

(a) $m = 0.5m, n = 0.0$.

(b) $m = 0.5, n = 1.0$.

(c) $m = 0.5, n = 1.7$.

(d) $m = 0.5, n = 2.0$.

Figure 6.4: Diameter effect curves comparing SSA calculations [$\Delta z'_f = 0.01$] with those previously published. The legend with $n = x$ indicates the parameters of the rate equation used for the calculation, 'Watt' indicates previously published data [30].

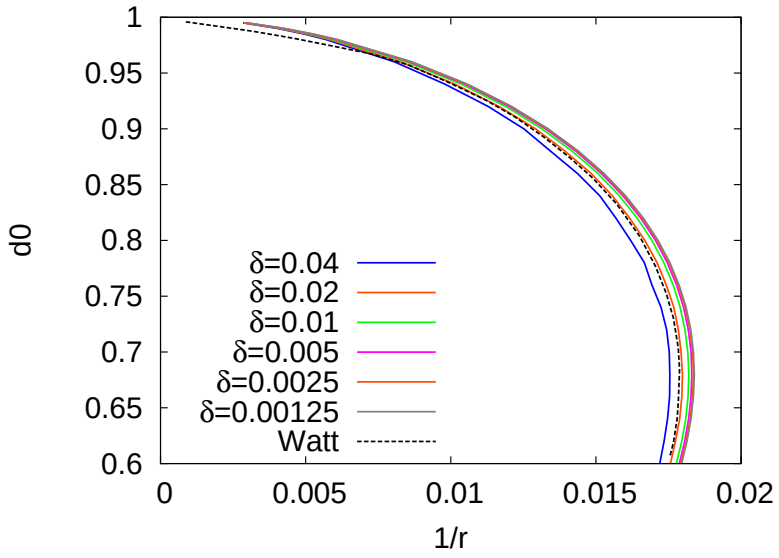

(a) $m = 0.5, n = 2.0$.

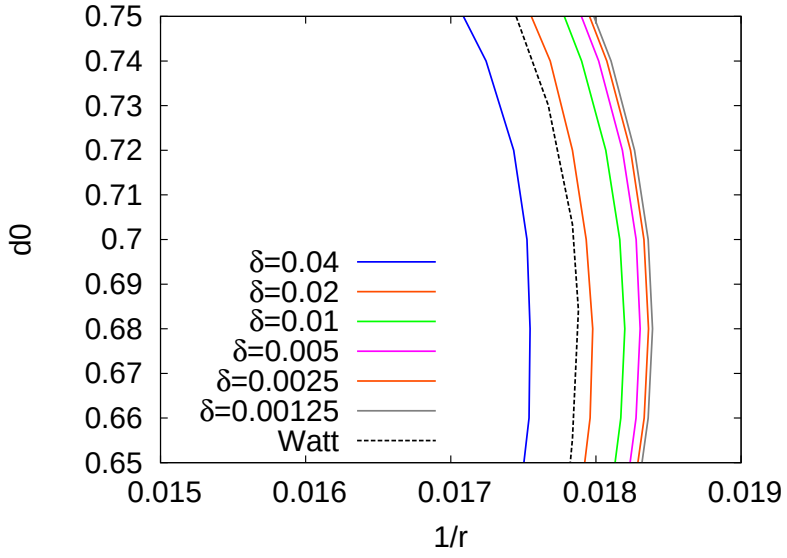

(b) Zoomed in section for $n = 2.0$.

Figure 6.5: Diameter effect curve for different step sizes $\Delta z'_f$ with $n = 2.0$. The legend indicates the minimum step in the shock slope, 'Watt' indicates previously published data [30].

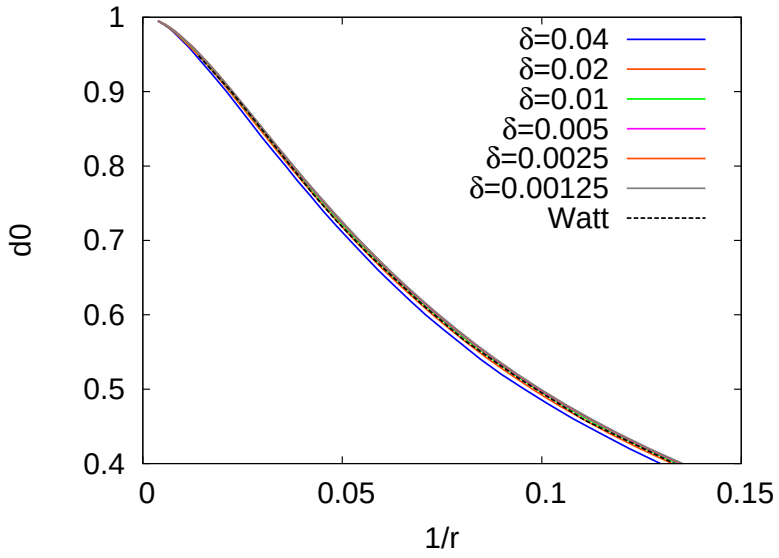

(a) $m = 0.5, n = 1.0$.

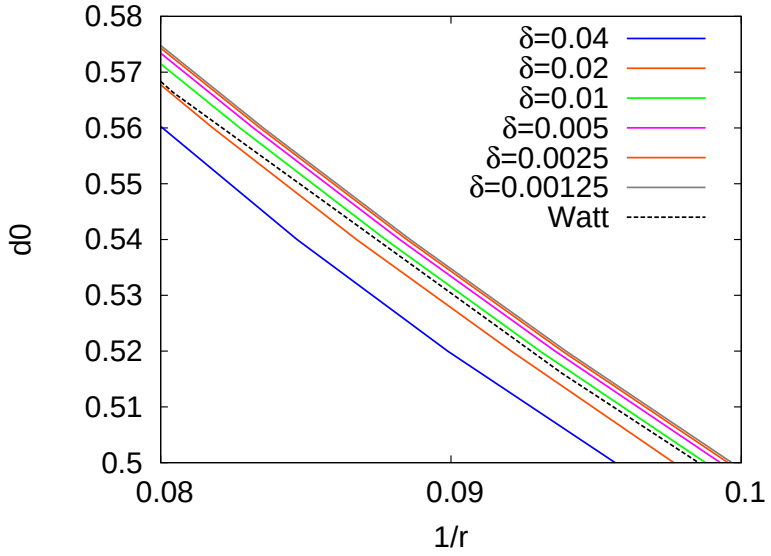

(b) Zoomed in section for $n = 1.0$.

Figure 6.6: Diameter effect curve for different step sizes $\Delta z'_f$ with $n = 1.0$. The legend indicates the minimum step in the shock slope, 'Watt' indicates previously published data [30].

6.7 Calculations with CREST Explosive Models

6.7.1 Boundary Conditions

Prior to solving the SSA equations for CREST a shock polar analysis was performed. This was required to determine the boundary condition for the edge of the explosive. For each shock slope z'_f there is a corresponding post-shock Mach number and streamline deflection angle. This results in a streamline-deflection shock polar as shown in figure 6.7. In the literature the pressure is often plotted instead of the Mach number [11][52]. However, for the discussion on boundary conditions, the Mach number is more relevant here. In figure 6.7 we begin by considering the Mach number for zero streamline deflection ($M \sim 0.6$) which corresponds to the post-shock flow state on the central streamline. For increasing z'_f, corresponding to integration along the surface towards the charge edge, the Mach number and streamline deflection both increase monotonically until the streamline deflection reaches a maximum. Thereafter, the streamlines will begin to converge behind the shock. The maximum streamline deflection angle is referred to as the Crocco point [53]. This poses a problem for the SSA model for which converging streamlines are not permissible since it requires a positive shock curvature to solve the eigenvalue problem. This is unphysical and thus places a limit on the maximum shock slope for which the SSA model can be applied. Crucially, for an unconfined calculation, we require that the flow is sonic at the charge edge. However, the inability to integrate beyond the Crocco point means that the SSA model cannot reach the shock slope where $M = 1$. This places a fundamental limitation on the SSA model in its application to any equation of state for which this feature exists.

For unconfined calculations with SSA and DSD, the Crocco point was used as the boundary condition for the charge edge.

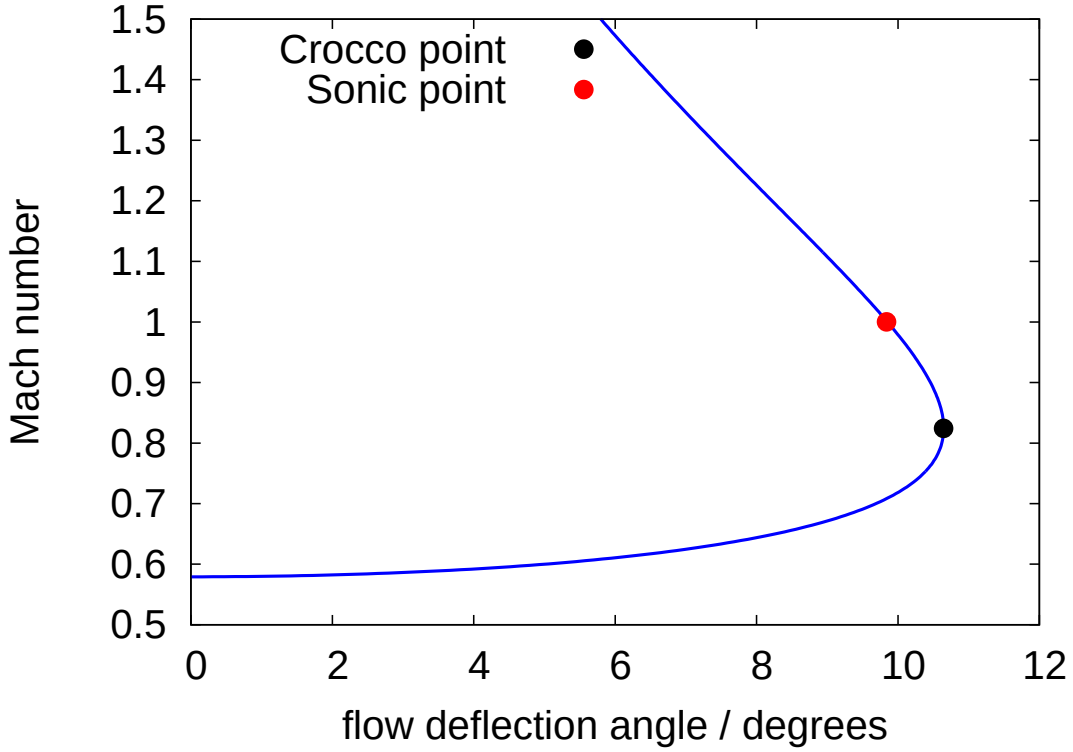

Figure 6.7: Post-shock Mach number versus streamline deflection angle for EDC37 EOS. The detonation velocity is $0.813\,cm\,\mu s^{-1}$.

6.7.2 DSD Model Comparison

Diameter effect curves were computed using the DSD model to provide an additional comparison between a different approximate detonation model and DNS.

At a given point along the shock front the normal shock velocity is related the shock slope, s, via

$$D_n = \frac{D}{(1+s^2)^{1/2}}.$$

It is now assumed that the solution to the quasi-one-dimensional detonation equations,

2.29-2.33, is valid such that for each D_n the shock curvature κ can obtained by solving those equations. For DSD the flow divergence term is given by

$$\frac{d\omega}{dr} = \frac{\kappa\,(D-u)}{1+z\kappa}, \tag{6.61}$$

where z is the distance behind the shock front. This is the form used in a previous DSD analysis [35]. The corresponding shock front curvature can then be related to the second derivative of the shock front via

$$\kappa = \frac{s'}{(1+s^2)^{\frac{3}{2}}} + \frac{s}{r\,(1+s^2)^{\frac{1}{2}}}. \tag{6.62}$$

for axisymmetric geometry [54]. Here $s = z'_f$ is the shock slope and $s' = z''_f$ is the shock slope derivative. With z''_f known we can integrate along the shock surface using a Taylor expansion.

$$z_s^{n+1} = z_s^n + \Delta r\, z'_f + \frac{1}{2}(\Delta r)^2 z''_f.$$

For a given detonation velocity the charge radius is determined by integrating along the shock front from the charge centre out to the edge. The charge edge condition is determined via a shock polar analysis. For an unconfined explosive the edge of the charge corresponds to the point at which the post-shock flow is exactly sonic.

6.7.3 Unconfined Calculations

Figure 6.8 shows the diameter effect curve for EDC37. The results from the DNS lie between those from the approximate DSD and SSA models. This is consistent with results previously published for a polytropic EOS with power law reaction rate [30]. The SSA model overpredicts the detonation velocity for a given charge radius. At small radii the disparity between the DNS results and the SSA is significant. The failure radius predicted by the SSA ($\sim 0.83\,mm$) is smaller than that predicted by the

DNS calculations ($\sim 1.25\,mm$). This difference is significant and is much greater than the differences between the DNS and SSA for previous calculations with a polytropic EOS where there was less than 5% difference between the failure radii. Figure 6.11 shows that qualitatively similar results are obtained for the PBX9502 model but SSA is much better than DSD in this case.

Figure 6.9 shows how the shock shape and sonic locus in the SSA model compares with the DNS for $D = 0.861\,cm\,\mu s^{-1}$, which is very close to the CJ velocity $D_{CJ} = 0.877\,cm\,\mu s^{-1}$ and the SSA closely matches the DNS data point on the diameter effect curve. The SSA model predicts that the shock curvature is smaller than the DNS calculation for $r < R/2$, (R is the radius of the rate-stick) however, close to where the SSA reaches the Crocco point the shock front curvature is larger than in the DNS. This would suggest that at this point in the flow streamline curvature effects are important. Moreover, the location of the sonic surface is in reasonable agreement with the DNS calculations.

Figure 6.10 shows how the SSA model compares with the DNS calculations for $D = 0.760\,cm\,\mu s^{-1}$, this detonation velocity corresponds to a rate-stick which is close to the failure diameter for the explosive. The SSA model accurately captures the shock surface for $r < R/2$. However, as the radius increases the SSA over-estimates the shock front curvature which results in a smaller total radius than the DNS calculation. Moreover it is clear that the distance between the shock surface and sonic surface is increasing rapidly towards the edge of the explosive for the SSA and fails to capture the behaviour at the edge where the two surfaces meet. This is a clear indication that the SSA model is failing to capture the complete physics at the edge of the explosive. In the previously published results for the polytropic EOS with power law reaction rate the shock front and sonic surface did meet at the edge for the SSA calculations[30].

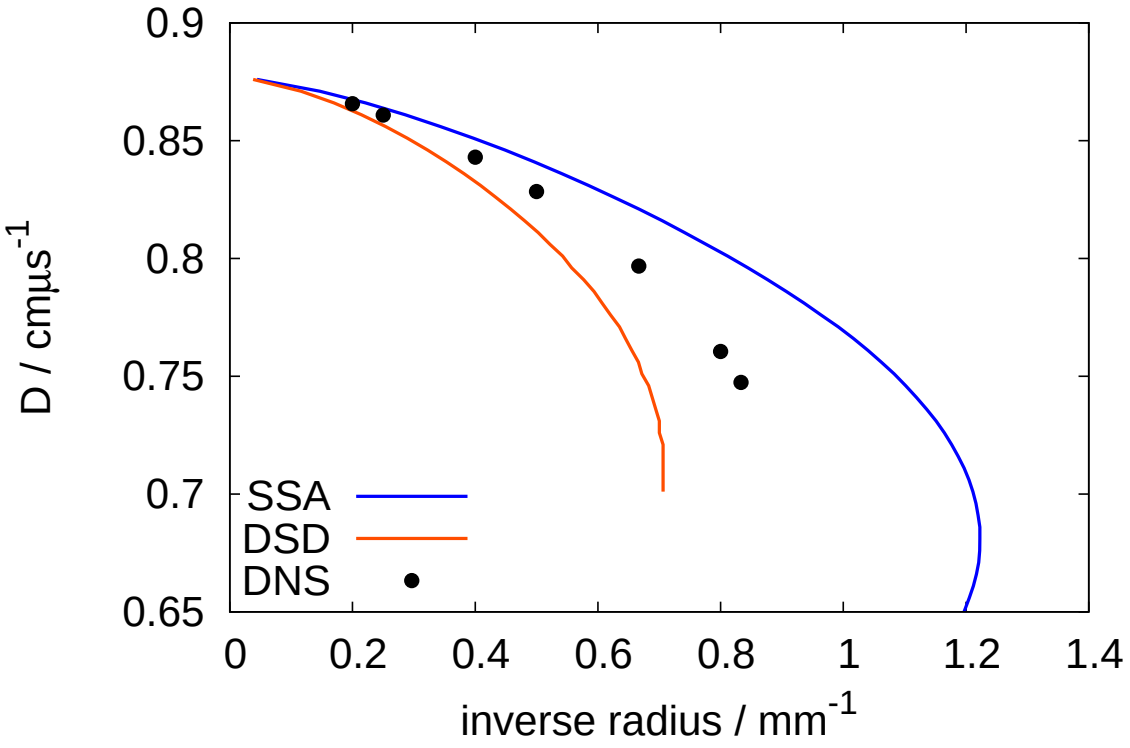

Figure 6.8: Diameter effect curve for EDC37. The CJ detonation speed is $D_{CJ} = 0.877\,cm\,\mu s^{-1}$.

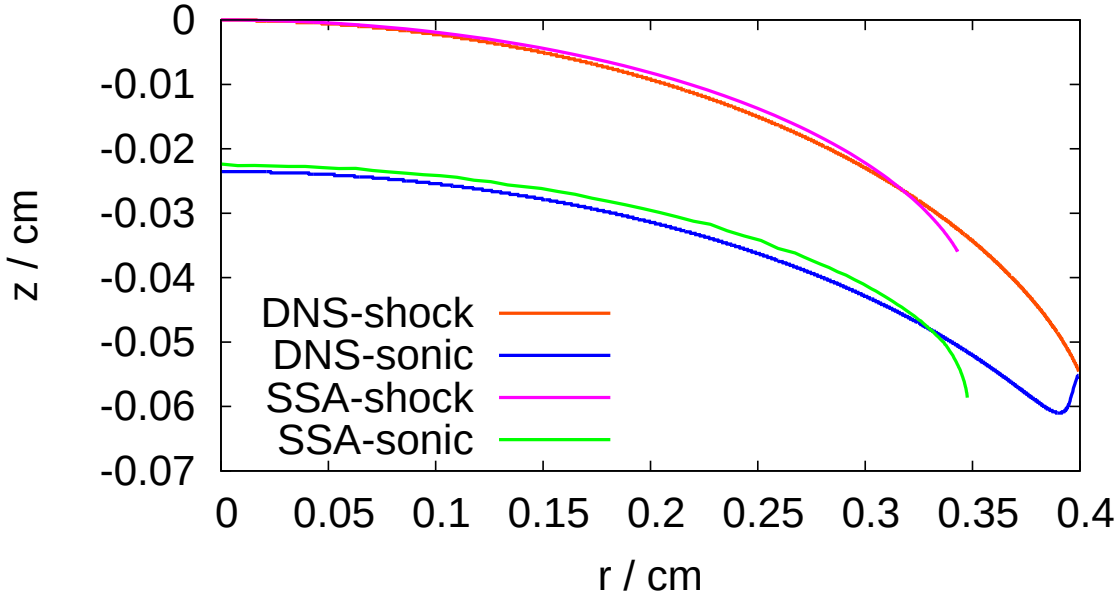

Figure 6.9: Shock front and sonic surface for EDC37 simulations with $D = 0.861\,cm\mu s^{-1}$, $r = 0.4\,cm$.

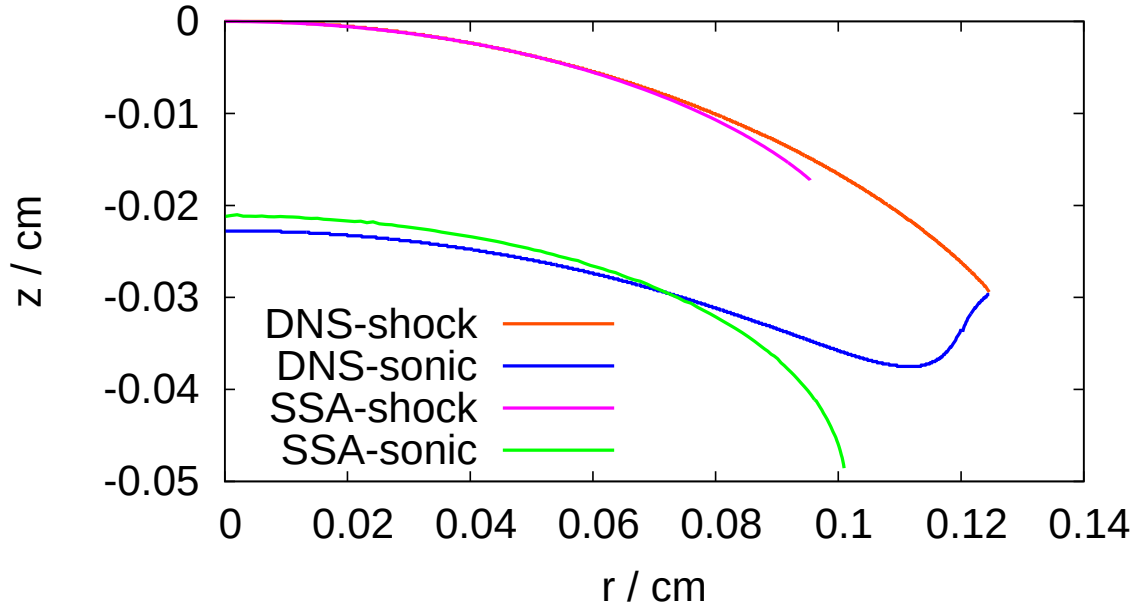

Figure 6.10: Shock surface and sonic surface for EDC37 simulations with $D = 0.760\,cm\mu s^{-1}$, $r = 0.125\,cm$.

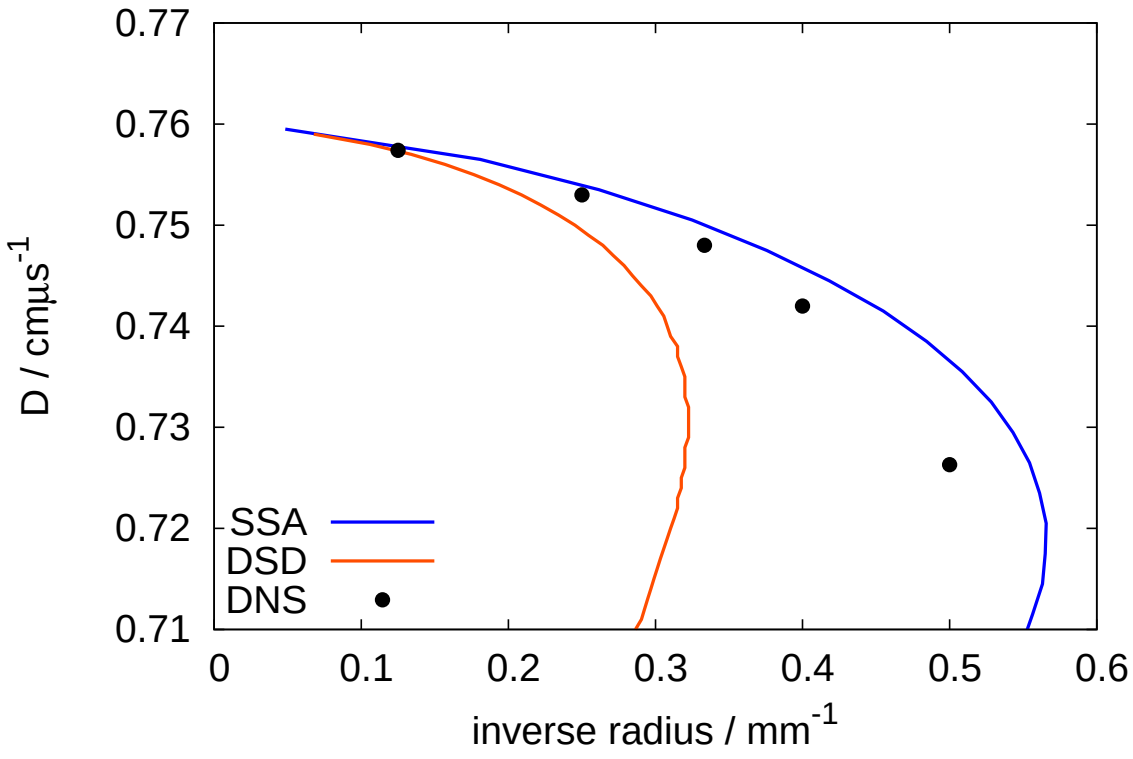

Figure 6.11: Diameter effect curve for PBX9502. The CJ detonation speed is $D_{CJ} = 0.760\, cm\, \mu s^{-1}$.

6.7.4 EDC37 EOS with Power law reaction rate

To separate the effects of the reaction rate from the EOS rate-stick calculations were performed for the CREST EDC37 EOS with a simple power law reaction rate of the form

$$\frac{d\lambda}{dt} = \alpha \left(1 - \lambda\right)^{1/2} . \tag{6.63}$$

Here $\alpha = 2.84 \mu s^{-1}$ was used. The magnitude of α was chosen for convenience with numerical calculations as we are only concerned with comparisons between numerical calculations and not experimental data. The dimensionality is retained to maintain consistency with the remaining equations in the model. The form of reaction rate was chosen as it is state insensitive and therefore the reaction rate at the charge edge would not be dependent upon shock strength. The main difference between this form of reaction rate and that of the CREST model is that the reaction rate is maximal at the shock and monotonically decreases, whereas for CREST the reaction has an induction zone immediately behind the shock before reaching its maximal value a significant distance behind the shock.

The DNS results were compared with the SSA model. The edge boundary condition for the SSA calculations was given by the Crocco point, which meant that the flow at the edge would not be sonic for the SSA calculations. This was discussed in section 6.7.1. Figure 6.12 shows that the SSA and DNS results are in excellent agreement for large charge radii. As the radius of the rate-stick decreases the SSA and DNS results diverge, with the SSA overpredicting the detonation velocity for a given charge size.

Comparing this diameter effect curve with that of the EDC37 reaction model (figure 6.8) it is clear that when the reaction rate is maximal at the shock the SSA and DNS results are in closer agreement than when there is an induction zone. This would suggest that streamline curvature effects inside the reaction zone are significant and the

SSA assumption is not valid for the CREST model.

Figure 6.13 shows how the shock shape and sonic locus in the SSA model compares with the DNS calculations for $D = 0.836\,cm\,\mu s^{-1}$. This detonation velocity corresponds to a rate-stick which is close to the CJ velocity ($D_{CJ} = 0.877\,cm\,\mu s^{-1}$). The SSA model underestimates the curvature of the shock surface until very close to the edge. The shape and location of the sonic surface is in reasonable agreement with the DNS calculation and the sonic locus does intersect the shock at the charge edge.

Figure 6.14 shows how the SSA model compares with the DNS calculations for $D = 0.694\,cm\,\mu s^{-1}$. This detonation velocity corresponds to a rate-stick which is significantly below the CJ velocity. Here the SSA model captures the shock surface accurately for $r < R/2$: it is only close to the edge of the explosive where the SSA and DNS results diverge. The sonic surface is captured accurately close to the centre. However, the SSA overpredicts the distance between the shock front and sonic surface close to the charge edge. This would suggest that, even for state insensitive reaction rates, the streamline curvature effects are important at the charge edge.

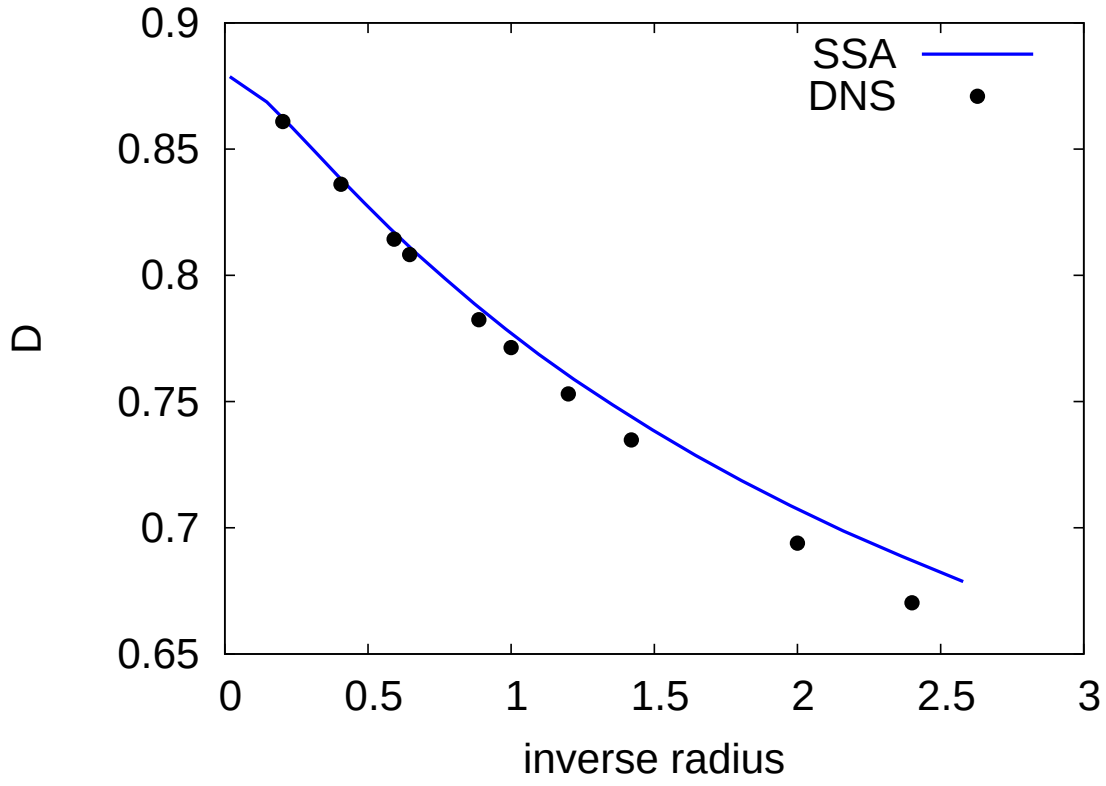

Figure 6.12: Diameter effect curve for EDC37 EOS with power law reaction rate. The CJ detonation speed is $D_{CJ} = 0.879\, cm\, \mu s^{-1}$.

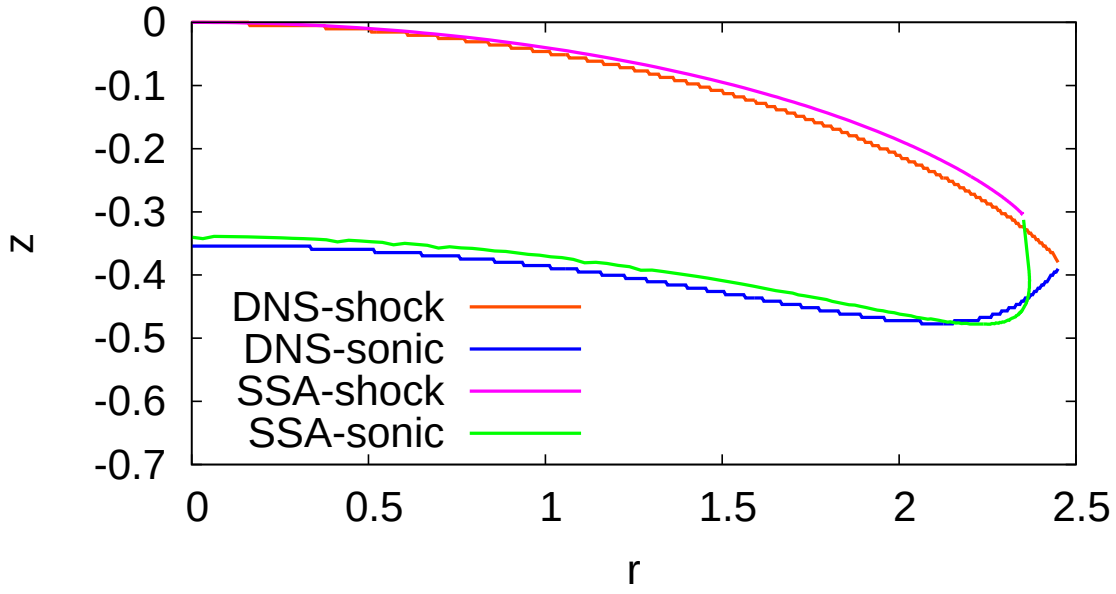

Figure 6.13: Shock front and sonic surface for EDC37 EOS with power law reaction rate with $D = 0.836\,cm\,\mu s^{-1}$, $r = 2.46\,cm$.

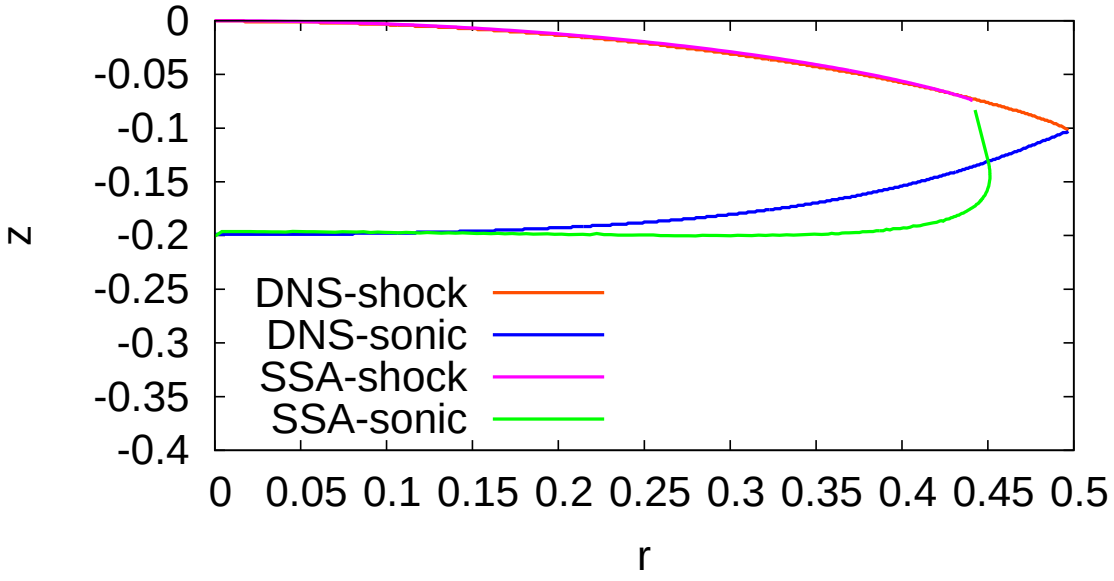

Figure 6.14: DDZ for EDC37 EOS with power law reaction rate with $D = 0.694\, cm\mu s^{-1}$, $r = 0.5\, cm$.

6.7.5 EDC37 Confined Calculation

Rate-stick calculations were performed for the CREST EDC37 (multiphase EOS and reaction rate) model with confinement. Confinement of the explosive provides lateral support to the high pressures generated inside the reaction zone, reducing shock curvature effects at the edge of the explosive. This enables detonation waves to propagate in charges with a much smaller radius than in the unconfined case [11]. With lateral confinement reducing the curvature effects at the charge edge the streamlines in the DDZ should be straighter and thus the SSA should be more accurate in this regime when compared to unconfined detonations.

The polytropic equation of state was used for the confiner with a stiffened polytropic gamma ($\gamma = 5$) and initial density of $\rho_0 = 7\, g/cm^3$, these parameters were chosen to ensure the correct shock-polar match. The explosive and confiner were initialised with the same pressure. The DNS results were compared with the DSD and SSA steady state models. The boundary angle used in the steady models was determined via a shock-polar match between the explosive and inert. Figure 6.15 shows the pressure streamline-deflection shock polar for the explosive and confiner. The match point occurs on the upper, subsonic branch of the explosive and the lower, supersonic, branch of the confiner. This type of match was observed for all detonation velocities. Moreover, the match point occurs before the Crocco point which ensures that the rate-stick edge boundary condition can be obtained with the SSA.

Figure 6.16 shows that the SSA underpredicts the detonation velocity for a given charge radius when compared with the DNS calculations. However, the difference is much smaller than for the unconfined case (figure 6.8). As the confiner provides support to the detonation driving zone the shock curvature effects at the edge of the explosive are likely to be reduced for the confined calculations and will result in the streamlines being

straighter, which is why the SSA agrees more closely with the DNS for the confined calculations. The DSD calculations significantly underpredict the detonation velocity when compared with the DNS.

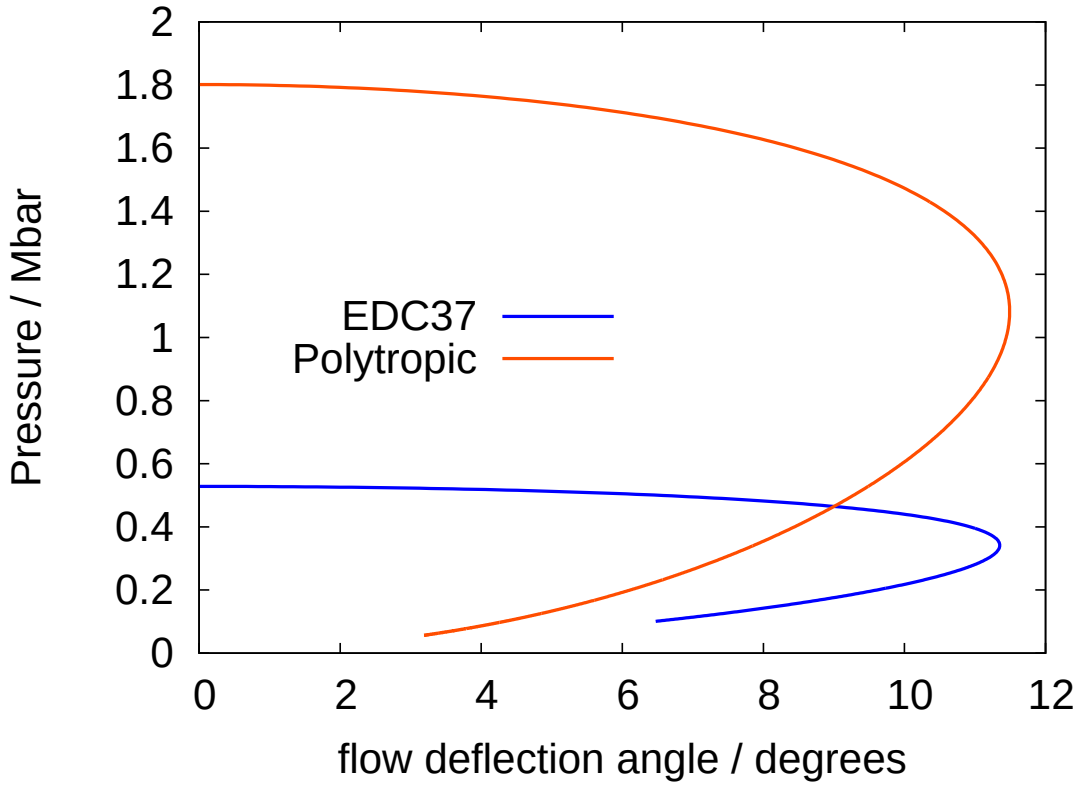

Figure 6.15: Pressure streamline-deflection shock polar for EDC37 and polytropic EOS ($\gamma = 5,\ \rho_0 = 7g\,cm^{-3}$) for $D = 0.879\,cm\,\mu s^{-1}$.

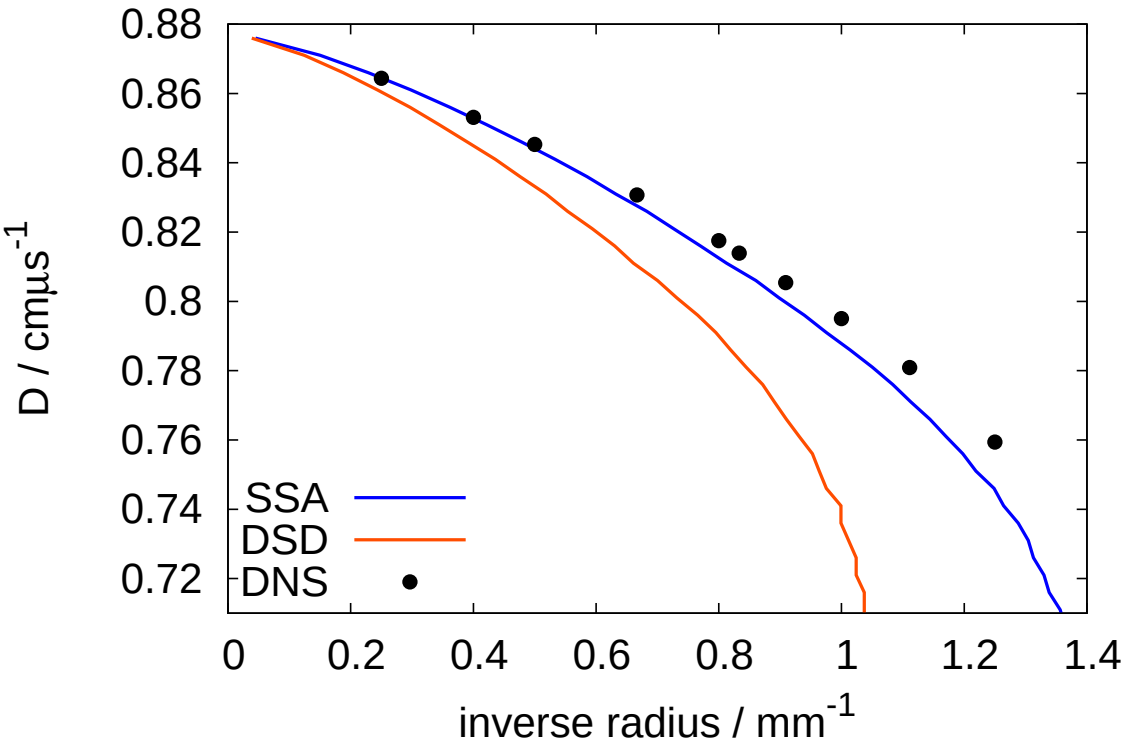

Figure 6.16: Diameter effect curve for EDC with polytropic confiner ($\gamma = 5$, $\rho_0 = 7g/cm^{-3}$). The CJ detonation speed is $D_{CJ} = 0.877\,cm\,\mu s^{-1}$.

6.8 Reaction Rate with Induction Zone

The simulations using the SSA model performed by Watt et al focused exclusively on a single step power law reaction rate for which the reaction rate is a maximum at the shock. Although this model is used widely in detonation modelling due to its convenience and simplicity [11][26][51], experimental evidence has suggested that there is an induction zone immediately behind the shock [13][55][56]. Other detonation models, such as Ignition and Growth and CREST have reaction rates where the maximum re-

action rate has an induction zone with maximal reaction rate occurring a finite time after being shocked.

6.8.1 Model Equations

The polytropic EOS was used with a reaction rate model with an induction zone. The induction zone was achieved using a two-step reaction model of the form

$$\begin{aligned} \frac{d\lambda_1}{dt} &= \alpha \left(1-\lambda_1\right)^{\frac{1}{2}}, \\ \frac{d\lambda_2}{dt} &= \beta\lambda_1 \left(1-\lambda_2\right)^{\frac{1}{2}}, \end{aligned} \tag{6.64}$$

where α and β are constants. This form of reaction rate was chosen as it is independent of the shock strength and thus reduces the coupling with the EOS. For simplicity $\beta = 1$ and α is chosen such that $\lambda_2 = \frac{1}{2}$ when the distance in the shock-attached frame $x = \frac{1}{2}$ in the one-dimensional ZND solution. The λ_1 reaction is analogous to a fast-burn reaction immediately behind the shock and λ_2 represents the bulk burn of the explosive. Multiplying the bulk burn reaction rate by λ_1 ensures that the reaction rate is zero immediately behind the shock and grows to a maximum a finite time behind the shock. These equations were coupled to the EOS and detonation model via λ_2 i.e. the polytropic EOS with

$$e = \frac{p}{\left(\gamma-1\right)\rho} - \lambda_2 q. \tag{6.65}$$

The behaviour of the reaction rates is shown in figure 6.17. The step-one reaction λ_1 has the typical power law form, maximal reaction rate at the shock and is monotonically decreasing behind the shock. The second-step reaction term λ_2 has a clear induction zone where the reaction rate is zero immediately behind the shock and increases to a maximal value a finite distance behind the shock.

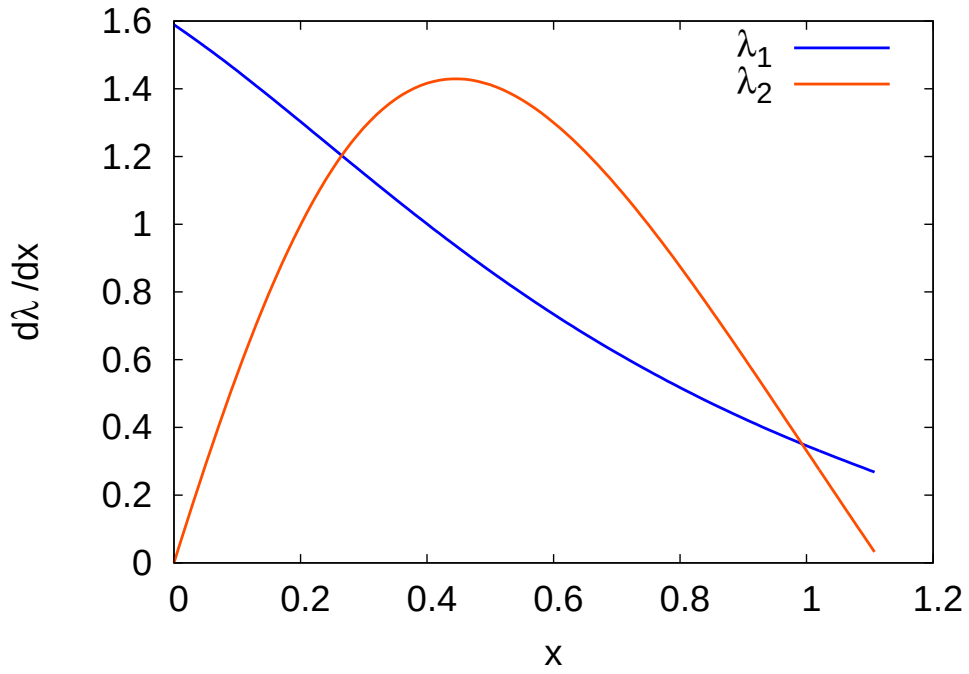

Figure 6.17: Reaction rate as a function of distance behind shock for ZND detonation with induction reaction rate. The legend indicates the fast reaction λ_1 and the bulk burn reaction λ_2.

6.8.2 Simulations

Implementation of the induction based reaction rate into the SSA, DSD and DNS calculations required the addition of an additional reaction scalar parameter to track the second step of the reaction. This was straightforward to implement in the relevant software. The same non-dimensional scalings were applied to this model as used by Watt et al. [30] and are described for the single term power law reaction rate in section 2.4.4. The boundary conditions for the SSA model were the same as those described in section 6.4 for the polytropic gas EOS.

The DNS calculations were performed using AMR. To reduce the computation time the detonation velocity was determined by varying the magnitude of the Galilean transformation applied to the domain until the shock remained static on the grid. This method was verified by performing laboratory frame calculations of a rate-stick with a length-to-diameter ratio of 15. The detonation velocity agreed to three significant figures for two different diameters.

6.8.3 Results and Discussion

A diameter effect curve for the induction based model was obtained for the SSA and DSD models. These results were compared with DNS calculations where each data point was converged to three significant figures in the detonation velocity.

Figure 6.18 shows that for large diameters the SSA overpredicts the detonation velocity when compared to DNS calculations. Here it should be noted that the reaction rate equations are state-insensitive and thus are only weakly coupled to the state of the explosive. With a single-step reaction rate the SSA and DNS calculations were in excellent agreement. However, when using a reaction rate where the reaction is not maximal at the shock, the SSA overpredicts the detonation velocity, suggesting that the cause of this is due to the induction zone in the reaction rate. Hence for any detonation model where the reaction rate is not maximal at the shock a streamline ansatz beyond straight lines would need to be considered to more accurately match the DNS calculations. Moreover, consistent with previous calculations performed with the polytropic equation of state, the DSD model underpredicts the detonation velocity.

Figure 6.19 compares the shock and surfaces obtained from the DNS and SSA calculations for $D = 0.889$ ($R = 20$). The SSA accurately matches the DNS calculations at the centre of the rate-stick. However, the surfaces begin to diverge as the radius

increases. For the SSA calculation the shock and sonic surfaces do not meet at the charge edge. For the polytropic EOS the flow is sonic at the charge boundary for the SSA but the shock and sonic surfaces do not meet. This feature was observed for the EDC37 model that also had an induction zone. This would suggest that unless the reaction rate is maximal at the shock the SSA is unable to capture the convergence of the shock and sonic surfaces at the charge edge. This again suggests that it is necessary to consider streamline curvature effects.

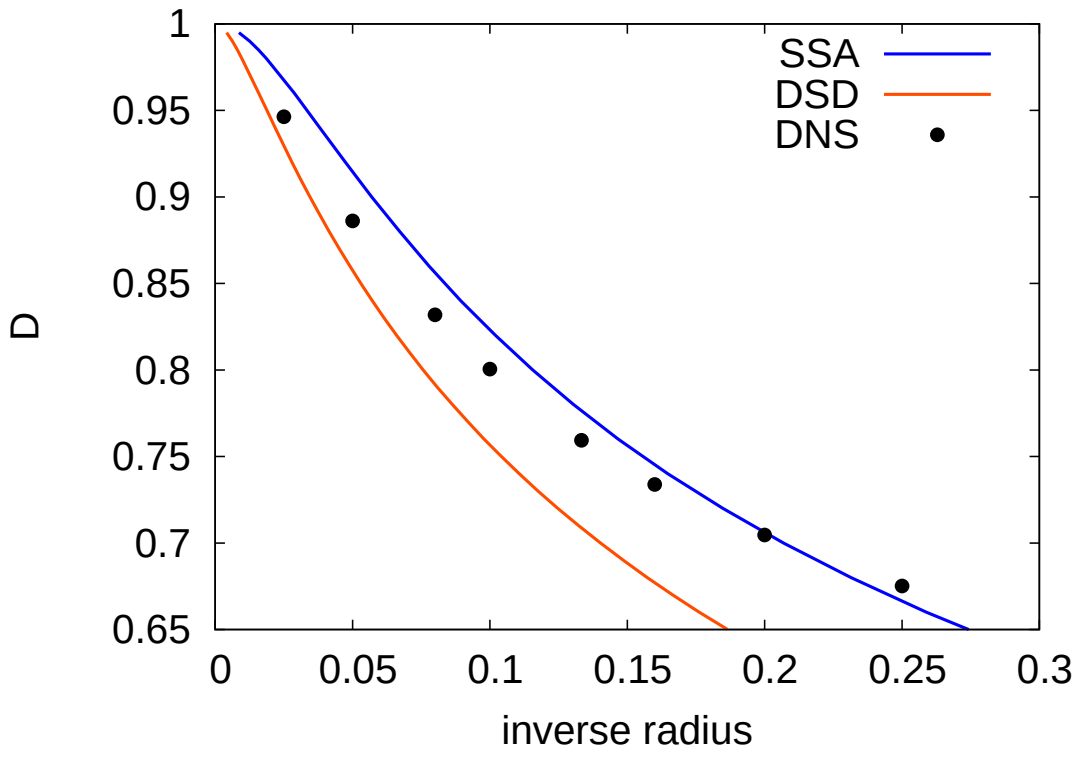

Figure 6.18: Diameter effect curve for polytropic EOS with induction type reaction rate. The SSA results are compared with DNS calculations and the DSD model. The CJ detonation speed is $D_{CJ} = 1$.

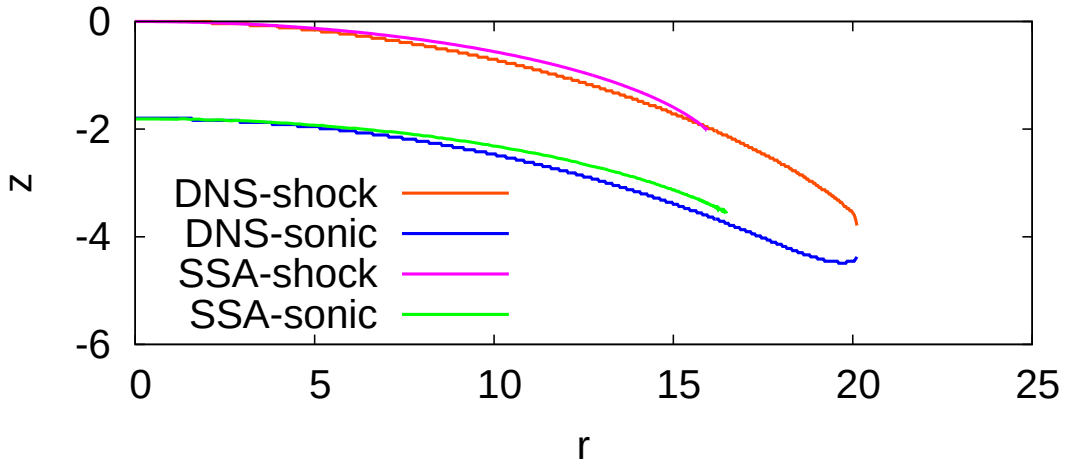

Figure 6.19: Shock front and sonic surface for polytropic EOS with induction type reaction rate for $D = 0.889$.

6.9 Non-Ideal Explosive EOS - ANFO

6.9.1 Model Equations

As a further test of the SSA model's predictive capability, a quadratic-gamma polytropic equation of state with a one-step power law reaction rate was considered. The equation of state and reaction rate were calibrated [35] to data for a non-ideal Ammonium-Nitrate Fuel Oil (ANFO) explosive typically used in the mining industry. The reaction

rate was

$$\frac{d\lambda}{dt} = \frac{1}{\tau}\left(\frac{p}{p_{ref}}\right)^{\frac{3}{2}}(1-\lambda)\,, \tag{6.66}$$

where τ and p_{ref} are constants. For this equation the reaction rate is maximal at the shock. The equation of state is the polytropic EOS with a gamma that is quadratic in the density

$$e = \frac{p}{(\gamma^* - 1)\,\rho} - \lambda q, \qquad \gamma^* = \gamma_0 + \gamma_1\frac{\rho}{\rho_0} + \gamma_2\left(\frac{\rho}{\rho_0}\right)^2. \tag{6.67}$$

The initial density of the explosive is ρ_0 and the initial pressure was $p_0 = 1 \times 10^5\, Pa$. The parameters for the model are given in table 6.1 and were taken from Sharpe & Braithwaite [35].

DNS calculations of unconfined rate-stick calculations were performed and compared with the SSA and DSD models. The boundary condition at the charge edge was given by the Crocco point, which occurs at a smaller shock slope than required for the post-shock flow to be sonic. The post-shock Mach number as a function of streamline deflection angle, for $D = 3.598\, km\, s^{-1}$, is shown in figure 6.20. The qualitative behaviour of the curve is the same as that of the EDC37 equation of state discussed in section 6.7.1.

Parameter	Value	Units
τ	28	μs
p_{ref}	1	GPa
ρ_0	0.8	g/cm^3
γ_0	1.3333	
γ_1	0.36264	
γ_2	0.076288	
q	3.822×10^6	J/Kg

Table 6.1: Parameters for ANFO explosive model[35].

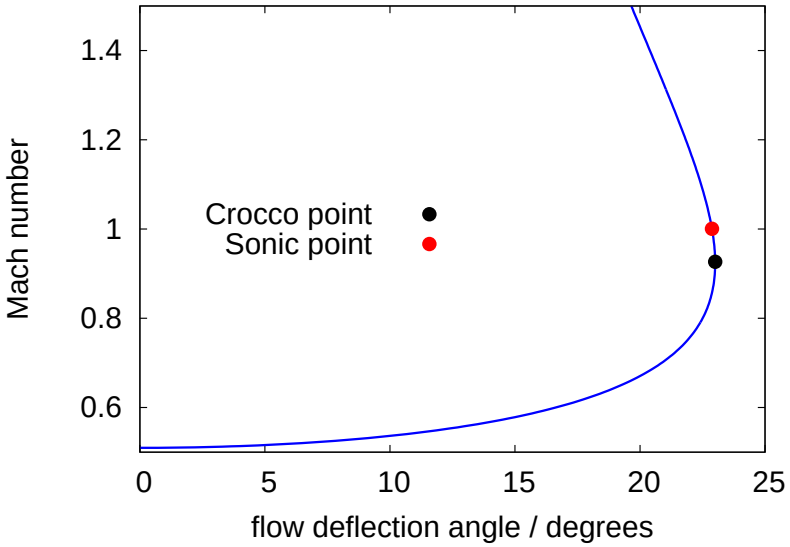

Figure 6.20: Streamline deflection shock polar for polytropic EOS with quadratic gamma for detonation velocity $D = 3598\,km\,s^{-1}$. Note that the exact form of this curve is independent of the detonation velocity.

6.9.2 Results and Discussion

The calculations were performed for an unconfined explosive. SSA and DSD calculations were also performed as comparison.

Figure 6.21 shows that the diameter effect curve calculated by the DNS lies between those predicted by the SSA and DSD models at large radii. However, both the SSA and DSD models fail to predict the behaviour of the diameter effect curve at small radii, where they both underpredict the detonation velocity.

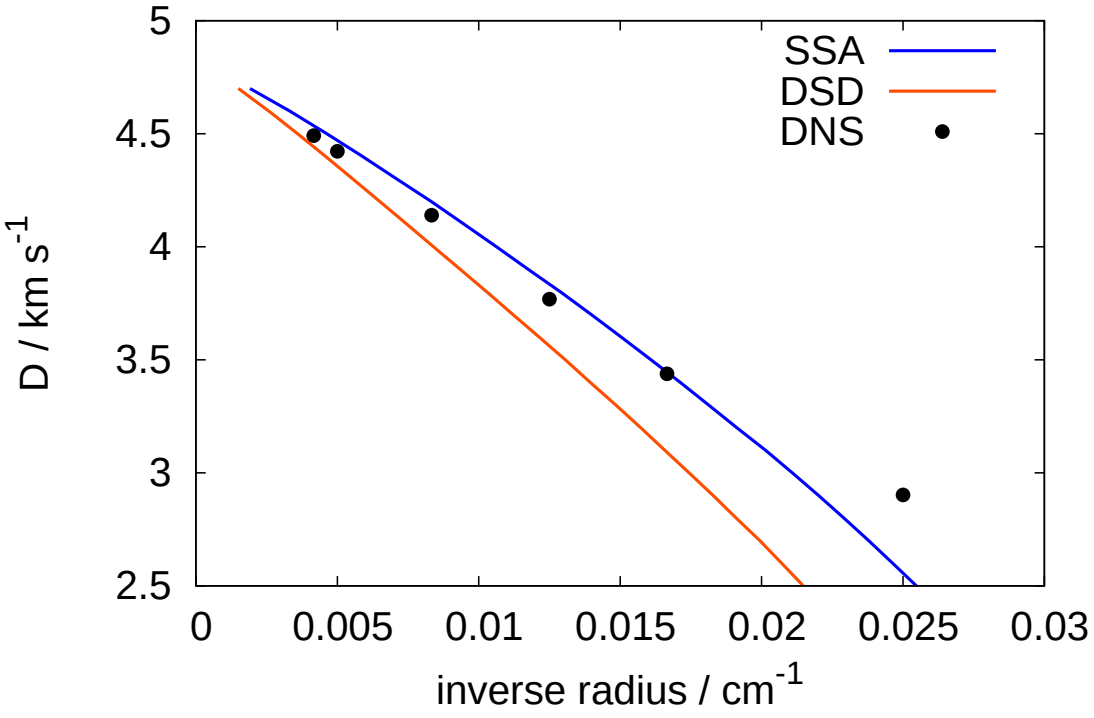

Figure 6.21: Diameter effect curve for an ANFO equation of state. The CJ detonation speed is $D_{CJ} = 4.794\,km\,s^{-1}$.

Chapter 7

Limitations of SSA Model

7.1 Introduction

In chapter 6 it was shown that there are many cases in which the SSA model is not able to capture diameter effect curves accurately when compared with DNS calculations. The greatest disparity between the SSA and DNS results was observed for reaction rate equations with a significant induction zone. Moreover, for some of the equations of state considered, the SSA model was unable to integrate to the charge boundary, due to the streamlines converging.

In the following chapter the unconfined SSA and DNS results are analysed to investigate these features. Moreover, the streamline curvature at the shock is calculated for the polytropic and CREST equations of state.

7.2 Failure to Reach Charge Edge

7.2.1 Shock Polar Analysis

In sections 6.7.1 and 6.9.1 it was shown that for the EDC37 (unreacted phase) and ANFO equations of state the SSA was unable to integrate to the boundary shock slope required for an unconfined rate-stick calculation. The Crocco point, where the streamline deflection is maximum, occurs before the post-shock flow is sonic for these equations of state. Figure 7.1 shows how the post-shock Mach number varies with streamline deflection for the EDC37, ANFO and polytropic equations of state. It is clear that the sonic point occurs after the Crocco point for EDC37 and ANFO. A similar result was also obtained for the PBX9502 equation of state, as well as the JWL equation corresponding to the fully reacted EOS. However, for the polytropic EOS the Crocco point coincides with the sonic point (see section 6.6.1). How significant is it that the SSA model fails to integrate beyond the Crocco point? The next section attempts to address this question.

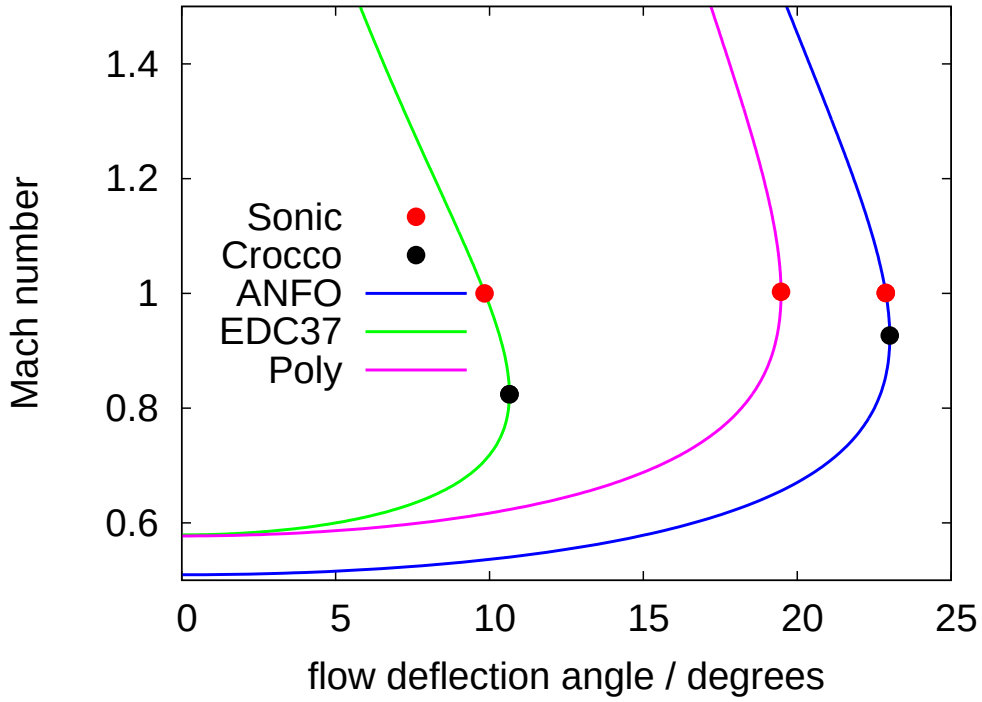

Figure 7.1: Mach number streamline-deflection shock polar for EDC37, polytropic (labelled Poly) and polytropic with quadratic gamma (labelled ANFO). $D = 0.813\,cm\,\mu s^{-1}$ was used for EDC37 and the remaining curves are independent of the detonation velocity. Note for the polytropic EOS the sonic and Crocco points coincide.

7.2.2 Shock Slope from SSA and DNS Calculations

The shock slope, as a function of radius, was calculated for the DNS calculations and compared to the results from the SSA model. The rate-stick calculations considered were those of the unconfined CREST EDC37 model and the EDC37 EOS with a power law reaction rate.

For the SSA model the shock slope is known as a function of r. To calculate the

shock slope from the DNS the shock surface coordinates were first obtained. Then the shock slope was calculated using a central difference approximation from the r, z data. Here no attempt was made to smooth the shock slopes computed from the DNS.

Figures 7.2 and 7.3 show how the shock slope varies as a function of radius for detonation velocities of $D = 0.861\, cm\, \mu s^{-1}$ and $D = 0.760\, cm\, \mu s^{-1}$. These detonation velocities correspond to near CJ and near failure. Both curves show the same general trend: the SSA model closely matches the DNS for $r < R/2$ and for increasing radius the shock slope increases more rapidly for the SSA than the DNS. Considering the DNS curves it is clear that the Crocco point, which corresponds to the minimum shock slope for the SSA, occurs extremely close to the charge edge for both the near CJ and near failure rate-stick calculations. This would suggest that, if the SSA could integrate to the Crocco point exactly, the effect on the diameter curve would be much smaller than that observed. This suggests that the streamline curvature is important.

Figures 7.4 and 7.5 show how the shock slope varies as a function of radius for $D = 0.836\, cm\mu s^{-1}$ and $D = 0.694\, cm\mu s^{-1}$ for the EDC37 EOS with a power law reaction rate. Figure 7.4 shows that the SSA and DNS are in reasonable agreement. However, for a detonation velocity much lower than D_{CJ}, the SSA shock slope decreases more rapidly than the DNS. This suggests that for a power law reaction rate curvature effects only become significant at lower detonation velocities. This would explain why the SSA and DNS results diverged in section 6.7.4.

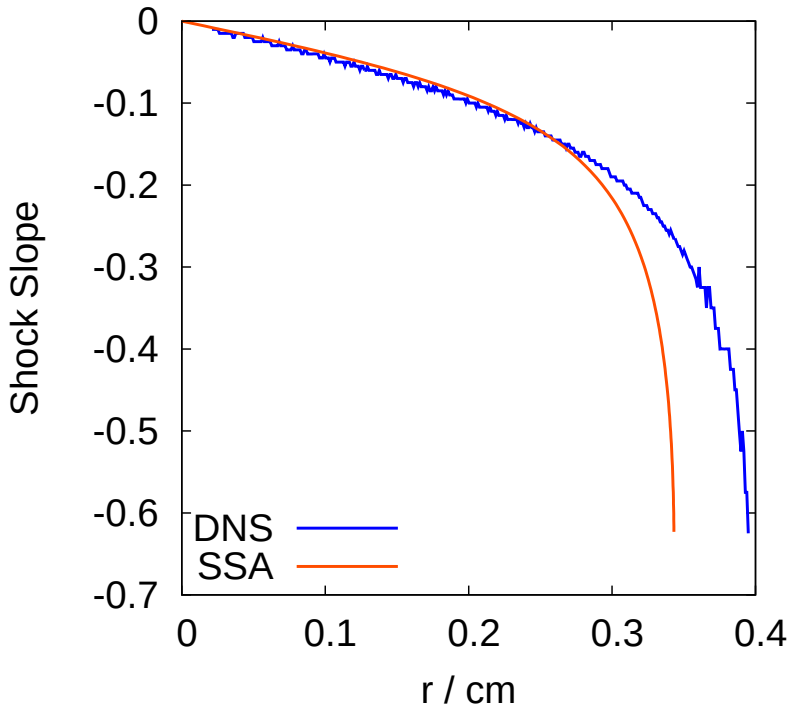

Figure 7.2: Shock slope as a function of charge radius for unconfined EDC37. The detonation velocity is $D = 0.861\,cm\,\mu s^{-1}$ and $D_{CJ} = 0.877\,cm\,\mu s^{-1}$.

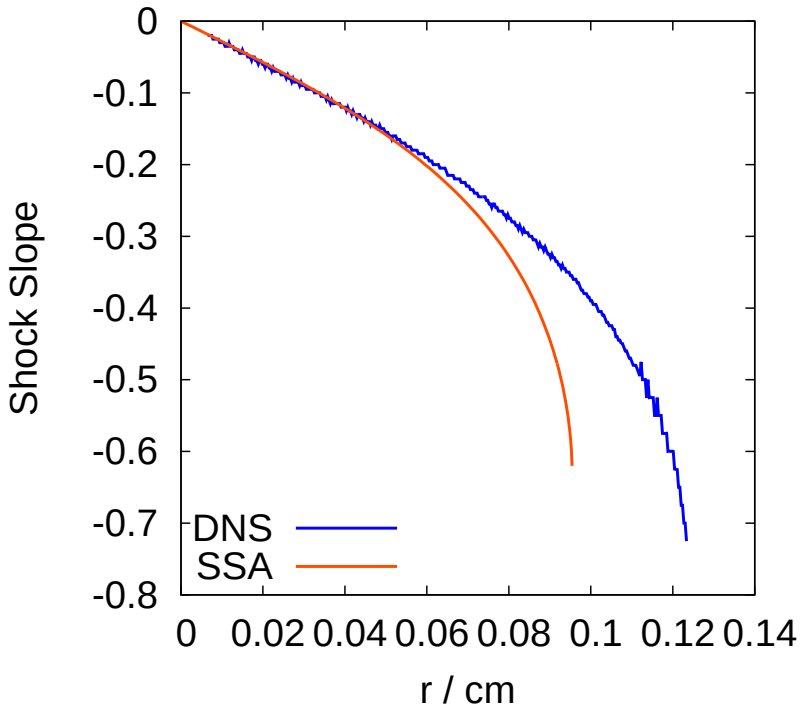

Figure 7.3: Shock slope as a function of charge radius for unconfined EDC37. The detonation velocity is $D = 0.760\,cm\,\mu s^{-1}$ and $D_{CJ} = 0.877\,cm\,\mu s^{-1}$.

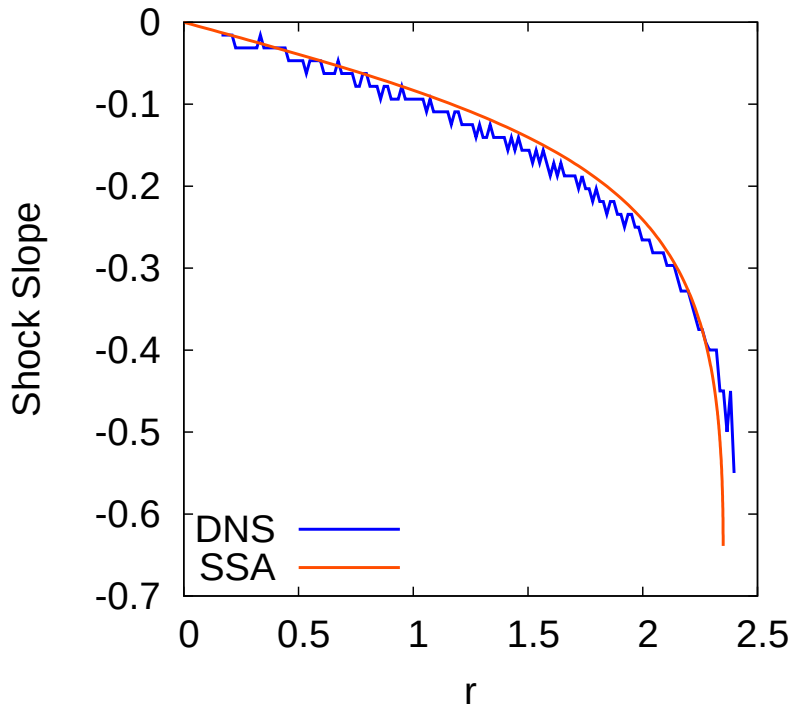

Figure 7.4: Shock slope as a function of charge radius for unconfined EDC37 EOS with power law reaction rate. The detonation velocity is $D = 0.836\, cm\, \mu s^{-1}$ and $D_{CJ} = 0.877\, cm\, \mu s^{-1}$

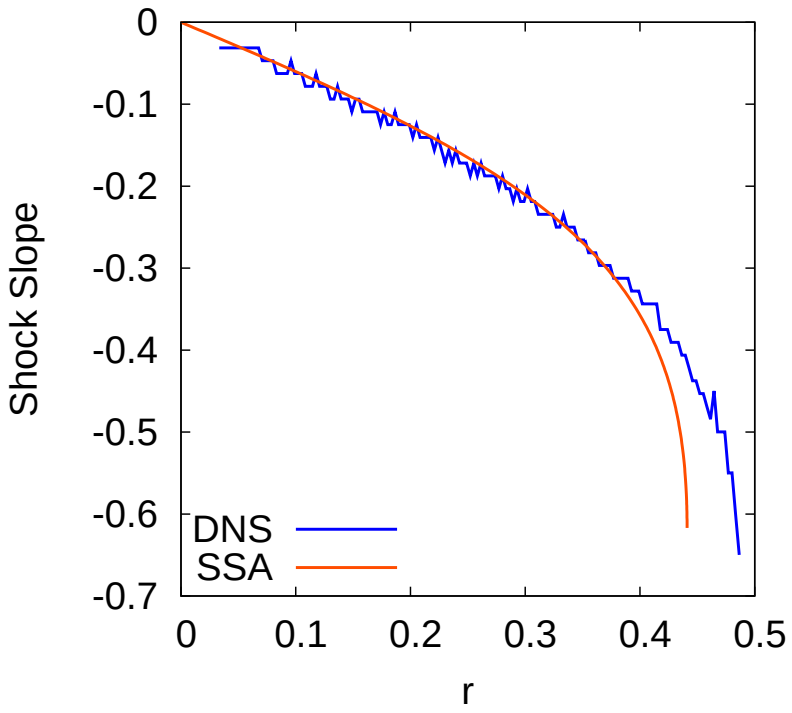

Figure 7.5: Shock slope as a function of charge radius for unconfined EDC37 EOS with power law reaction rate. The detonation velocity is $D = 0.694\,cm\,\mu s^{-1}$ and $D_{CJ} = 0.877\,cm\,\mu s^{-1}$.

7.2.3 Sonic Point in DNS Calculations

The shock polar analysis in section 7.2.1 showed that the sonic point, corresponding to the edge of the explosive, occurs after the maximal streamline deflection angle had been obtained. This would suggest that to get to the sonic point the streamlines, in the absence of curvature, would begin to converge at the edge of the explosive. Streamlines for the unconfined DNS calculation with CREST EDC37 were computed and overlaid onto the subsonic region as shown in figure 7.6. The rate-stick radius was $1.25\,mm$ and the detonation velocity was $D = 0.760\,cm\,\mu s^{-1}$. This was close to the failure radius of the explosive. The deflection angle of the streamlines was calculated at different radii close to the charge edge. In the region where the streamline deflection angles were calculated there was little, or no, reaction and hence the explosive is described by the solid EOS only in this region.

Table 7.1 shows that the streamline deflection angle reaches a maximum a small, but finite, distance from the edge of the rate-stick. This shows that in the DNS calculation the streamlines do converge near the charge edge and that the shock polar, figure 7.1 is followed smoothly from the Crocco point to the sonic point at the charge edge. At this point a transonic Prandtl-Meyer expansion fan matches the explosive to the inert confiner. A shock polar analysis in [11] implied that the streamlines converged at the edge of the rate-stick for the equation of state considered. However, there was no confirmation in any calculations that this was the case.

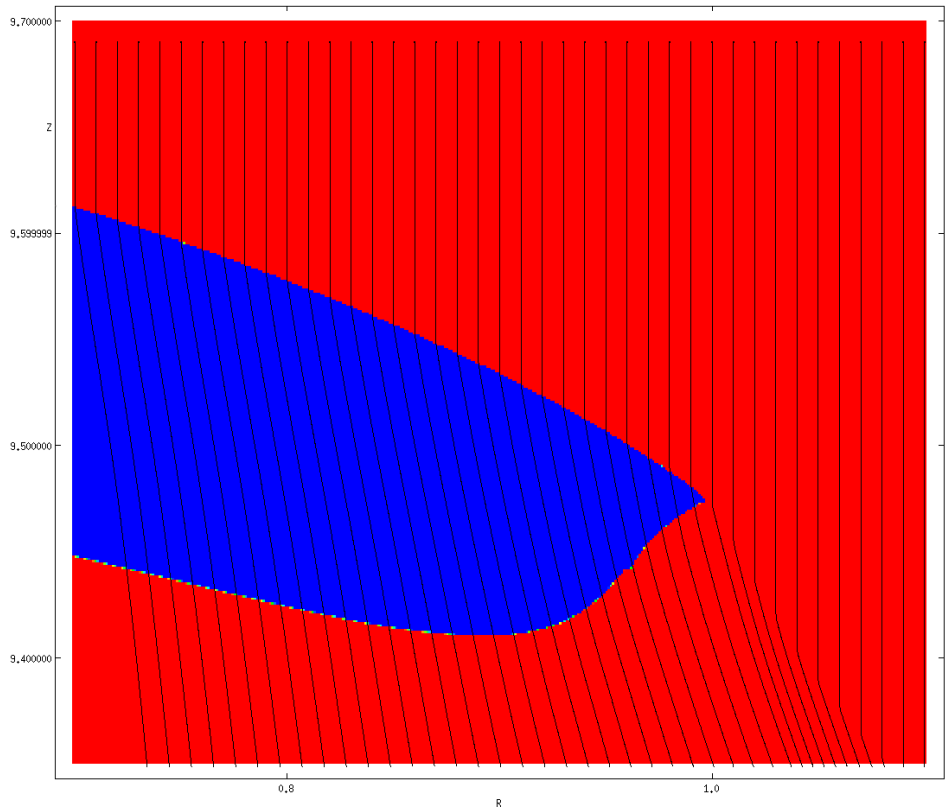

Figure 7.6: Subsonic region (blue) from DNS calculation with EDC37: $r = 1.25\,mm$ with streamlines superimposed for $0.7 < r/R < 1.1$. The detonation velocity is $D = 0.760\,cm\,\mu s^{-1}$ and $D_{CJ} = 0.877\,cm\,\mu s^{-1}$.

Streamline	Deflection Angle / Degrees	Radius
1	9.9	0.98
2	10.6	0.94
3	9.7	0.90
4	9.5	0.86

Table 7.1: Streamline deflection angle for different radii from DNS calculation of CREST EDC37 for $D = 0.760\,cm\,\mu s^{-1}$. The radius is given as a fraction of the total radius of the rate-stick. $D_{CJ} = 0.877\,cm\,\mu s^{-1}$.

7.3 Streamline Shapes From DNS

The SSA is based upon the assumption that the streamlines are straight throughout the reaction zone. But how straight are they? Streamlines were generated from the DNS calculations by applying a Galilean transformation to the axial velocity with the detonation velocity. The streamline shapes for different explosive models are compared.

7.3.1 CREST EDC37

Streamline data was obtained for the CREST EDC37 explosive for $r = 1.25\,mm$. Figure 7.7 shows that the streamlines in the subsonic region are weakly curved throughout the reaction zone across the rate-stick (a blow-up of the charge edge is shown in figure 7.6). The majority of the streamlines curve inwards towards the axis. However, close to the edge of the rate-stick, the streamlines curve away from the axis. Figure 7.8 shows the reaction source term for the same calculation. The maximum streamline curvature coincides with where the reaction source term is also a maximum. At the charge edge, where the streamlines curve away from the axis, the reaction source term is very small. This is to be expected since it has been shown that the chemical reaction has the effect of curving the streamlines towards the axis and that the shock curvature causes streamlines to curve away from the axis [26]. At the charge edge the Prandtl-Meyer rarefaction curves the streamlines outwards away from the axis. Moreover, figure 7.9 shows that where the pressure gradient is largest occurs at the charge edge, which coincides with the region of greater streamline curvature.

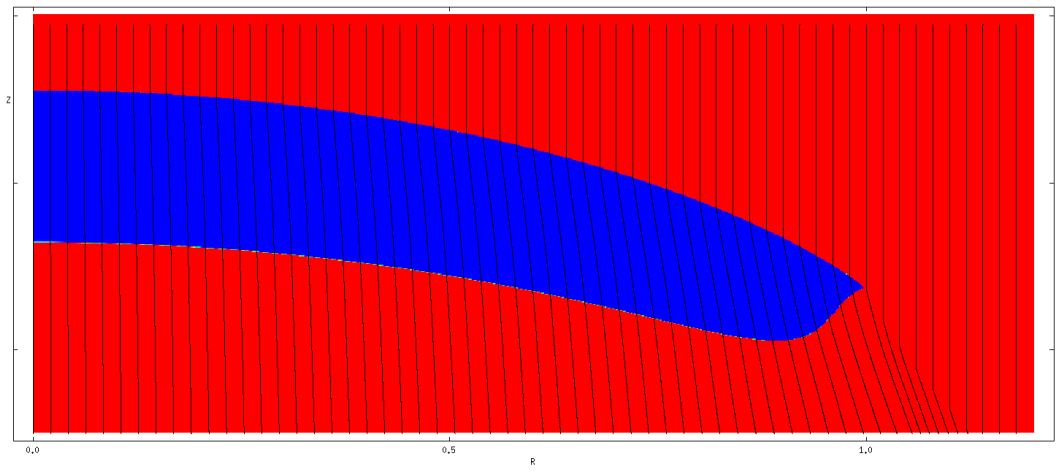

Figure 7.7: Subsonic region (blue) from DNS calculation with EDC37: $r = 1.25mm$ with streamlines superimposed. The detonation velocity is $D = 0.760\,cm\,\mu s^{-1}$ and $D_{CJ} = 0.877\,cm\,\mu s^{-1}$.

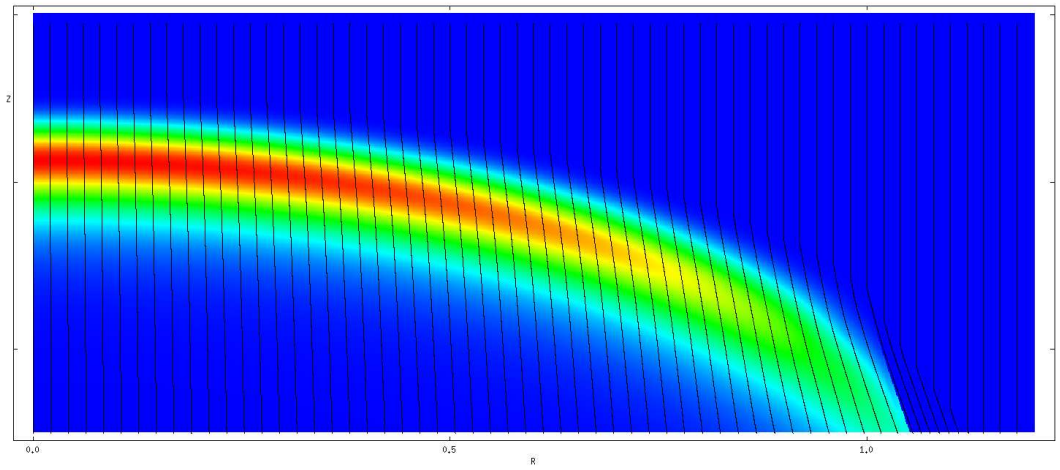

Figure 7.8: Reaction source term from DNS calculation with EDC37: $r = 8mm$ with streamlines superimposed. The detonation velocity is $D = 0.760\,cm\,\mu s^{-1}$ and $D_{CJ} = 0.877\,cm\,\mu s^{-1}$.

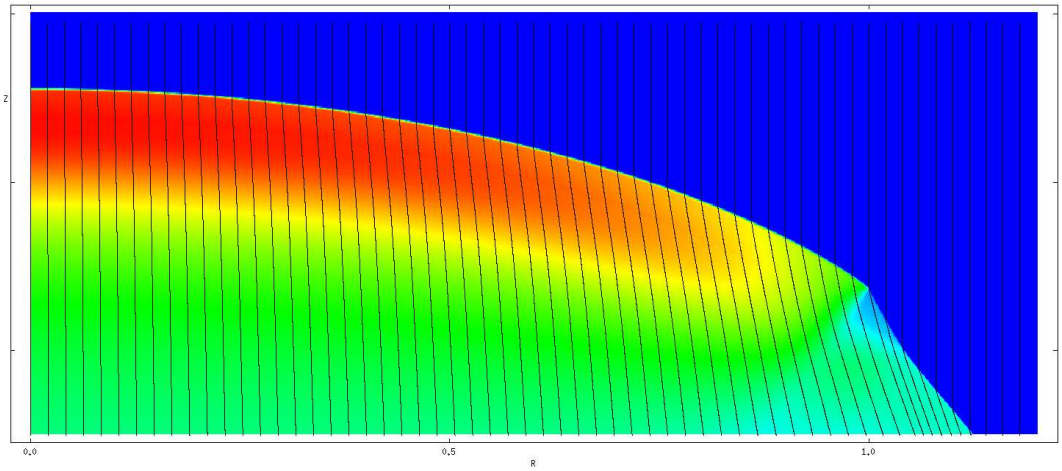

Figure 7.9: Pressure from DNS calculation with EDC37: $r = 1.25mm$ with streamlines superimposed. The shock in the confiner can be clearly seen. The detonation velocity is $D = 0.760\,cm\,\mu s^{-1}$ and $D_{CJ} = 0.877\,cm\,\mu s^{-1}$.

7.3.2 CREST EDC37 EOS with Power Law Reaction

Streamline data was obtained for the CREST EDC37 EOS with the power law reaction rate for $r = 0.5\,cm$ with $D = 0.836\,cm\,\mu s^{-1}$ ($D_{CJ} = 0.877\,cm\,\mu s^{-1}$). Details of the reaction rate can be found in section 6.7.4. Figure 7.10 shows that the streamlines in the subsonic region appear to be very straight. This is in stark contrast with figure 7.7 for the CREST reaction rate where the streamlines were more significantly curved. The straightness of the streamlines would explain why the diameter effect curves for the SSA and DNS calculations agreed more closely than those for the CREST reaction rate. Figure 7.11 shows that the reaction rate is maximum immediately behind the shock and, as the reaction is state-insensitive, has the same magnitude across the rate-stick.

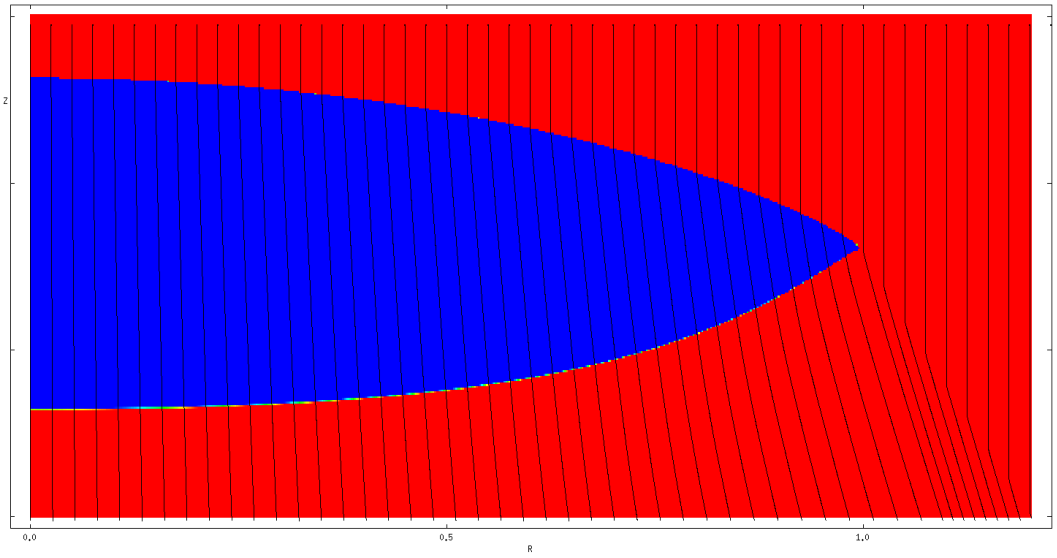

Figure 7.10: Subsonic region (blue) from DNS calculation with EDC37 EOS and single-term power law reaction rate: $r = 0.5\,cm$ with streamlines superimposed. The detonation velocity is $D = 0.836\,cm\,\mu s^{-1}$ and $D_{CJ} = 0.877\,cm\,\mu s^{-1}$.

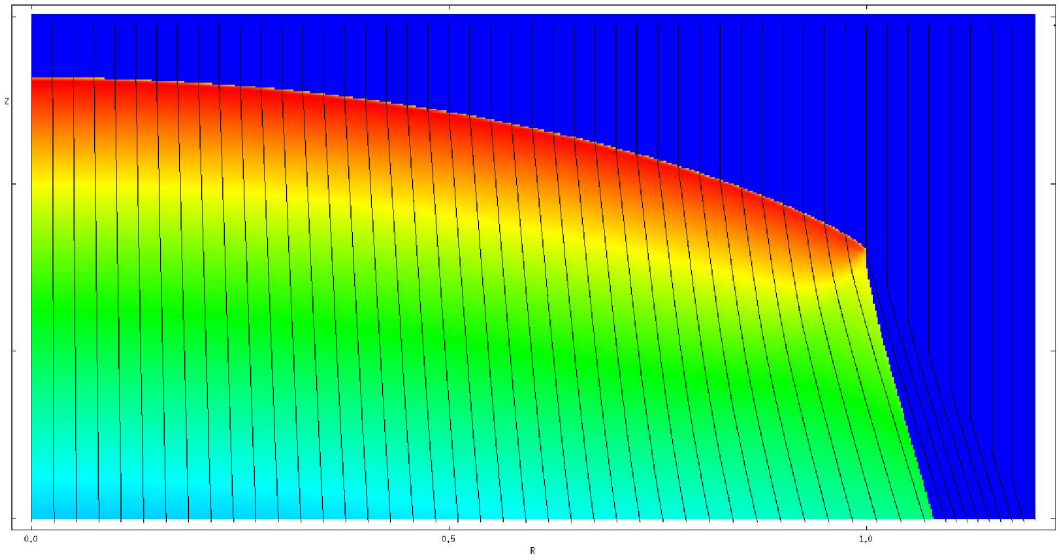

Figure 7.11: Reaction source term from DNS calculation with EDC37 EOS and single-term power law reaction rate: $r = 0.5\,cm$ with streamlines superimposed. The detonation velocity is $D = 0.836\,cm\,\mu s^{-1}$ and $D_{CJ} = 0.877\,cm\,\mu s^{-1}$.

7.3.3 Polytropic EOS with Induction Zone Reaction

Streamline data was obtained for the polytropic EOS with an induction zone for $r = 12.5$ and $D = 0.827$ (see section 6.8.1 for details on reaction equations). Figures 7.12 and 7.13 show that when an induction type reaction rate is used the streamlines have significant curvature in the region where the reaction rate is a maximum and thus the SSA will not capture the flow accurately in the subsonic region, evidence of this was discussed in section 6.8.3.

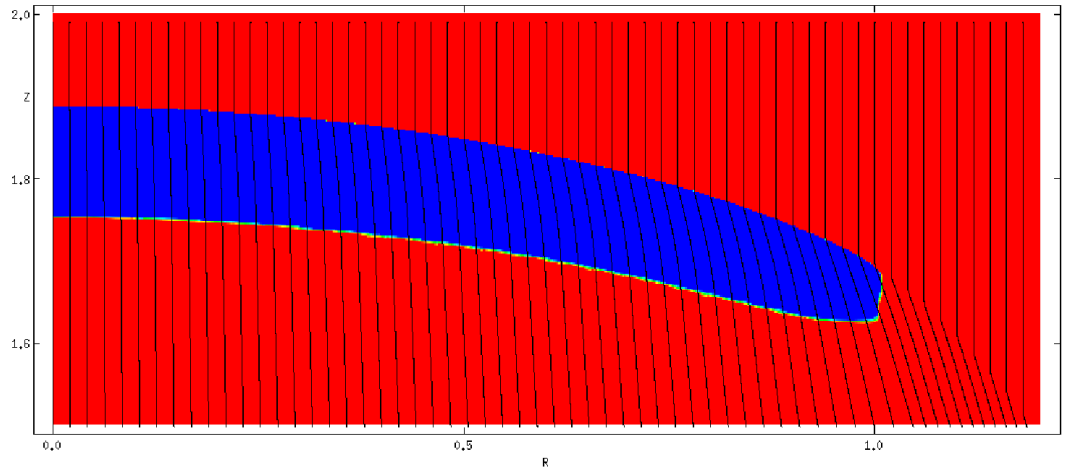

Figure 7.12: Subsonic region (blue) from DNS calculation with a polytropic EOS and induction reaction rate: $r = 12.5$. Streamlines superimposed. The detonation velocity is $D = 0.827$ and $D_{CJ} = 1$.

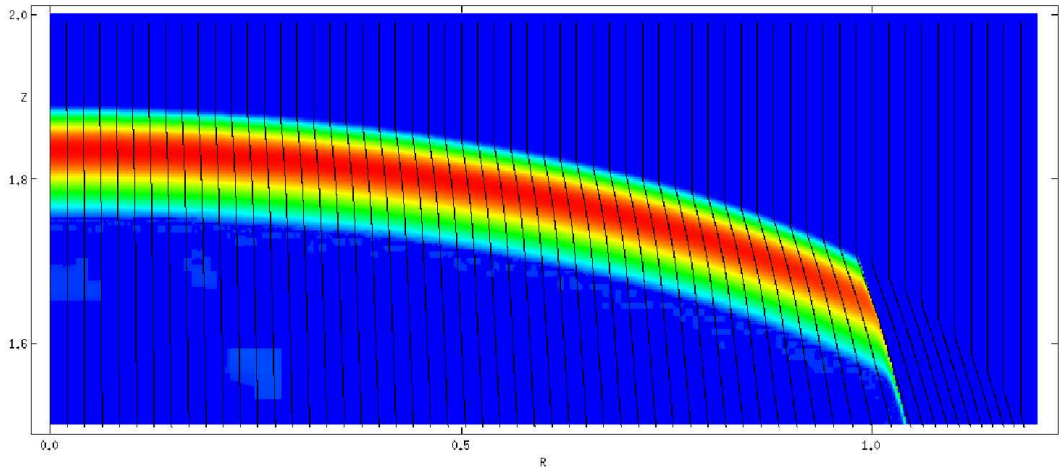

Figure 7.13: Reaction source term from DNS calculation with a polytropic EOS and induction reaction rate: $r = 12.5$ with streamlines superimposed. The detonation velocity is $D = 0.827$ and $D_{CJ} = 1$.

7.4 Post-shock Streamline Curvature

A derivation of the streamline curvature behind an oblique shock was first published by Thomas [57] for planar flow with a uniform upstream state. Rao [53] published equations for the streamline curvature behind an axisymmetric shock. This was also for a uniform upstream state. Molder has developed the theory further to consider a non-uniform flow upstream of the shock [58]. However, these calculations did not consider the effect of a chemical reaction at the shock. In the following section expressions for the post-shock streamline curvature are derived and calculations with the polytropic EOS and CREST EDC37 model are performed.

7.4.1 Derivation of Streamline Curvature

Since this is a local analysis, it is convenient to use Cartesian coordinates (x, y). We parameterise the streamline such that $x = x_s(y)$. We define the slope M and curvature K

$$M = \frac{dx_s}{dy}. \tag{7.1}$$

$$K = \frac{dM}{dy}. \tag{7.2}$$

Immediately behind the shock

$$M = \frac{u\,(x, y)}{v\,(x, y)}, \tag{7.3}$$

where u and v are the post-shock velocities in the x and y directions. Substituting for M into 7.2

$$\begin{aligned}
K =& \frac{d}{dy}\left(\frac{u}{v}\right), \\
=& \frac{1}{v}\frac{du}{dy} - \frac{u}{v^2}\frac{dv}{dy}, \\
=& \frac{1}{v}\left[\frac{\partial u}{\partial y} + \frac{dx_s}{dy}\frac{\partial u}{\partial x}\right] - \frac{u}{v^2}\left[\frac{\partial v}{\partial y} + \frac{dx_s}{dy}\frac{\partial v}{\partial x}\right], \\
K =& \frac{1}{v}\left[\frac{\partial u}{\partial y} + M\frac{\partial u}{\partial x} - M\frac{\partial v}{\partial y} - M^2\frac{\partial v}{\partial x}\right], \qquad (7.4)
\end{aligned}$$

where M has been substituted using 7.3. This is an expression for the streamline curvature, immediately behind the shock, in terms of partial derivatives of the flow velocity with respect to x and y. To determine the streamline curvature expressions for these will need to be determined. The procedure for obtaining the partial derivatives are described in the following sections.

7.4.2 Euler Equations

We first consider the steady reactive Euler equations 2.1- 2.5. These are given by

$$\begin{aligned}
\underline{\mathbf{u}} \cdot \nabla\rho + \rho\nabla \cdot \underline{\mathbf{u}} =& 0, \\
\rho\underline{\mathbf{u}} \cdot \underline{\mathbf{u}} + \nabla p =& 0, \\
\underline{\mathbf{u}} \cdot \nabla e - \frac{p}{\rho^2}\underline{\mathbf{u}} \cdot \nabla\rho =& 0, \\
\underline{\mathbf{u}} \cdot \nabla\lambda =& W.
\end{aligned}$$

Writing these equations in Cartesian coordinates

$$u\frac{\partial \rho}{\partial x} + v\frac{\partial \rho}{\partial y} + \rho\frac{\partial u}{\partial x} + \rho\frac{\partial v}{\partial y} = 0, \qquad (7.5)$$

$$\rho u\frac{\partial u}{\partial x} + \rho u\frac{\partial u}{\partial y} + \frac{\partial p}{\partial x} = 0, \qquad (7.6)$$

$$\rho v \frac{\partial v}{\partial x} + \rho v \frac{\partial v}{\partial y} + \frac{\partial p}{\partial y} = 0, \tag{7.7}$$

$$u \frac{\partial e}{\partial x} + v \frac{\partial e}{\partial y} - \frac{pu}{\rho^2} \frac{\partial \rho}{\partial x} - \frac{pv}{\rho^2} \frac{\partial \rho}{\partial y} = 0, \tag{7.8}$$

$$u \frac{\partial \lambda}{\partial x} + v \frac{\partial \lambda}{\partial y} = W. \tag{7.9}$$

where equations 7.6 and 7.7 are the momentum equations in the x and y directions respectively. The energy and reaction equations, 7.8 and 7.9, can be combined with the equation of state $e = e(p, \rho, \lambda)$ and the expression for the sound speed (see equation A.2 in appendix A) to give

$$u \frac{\partial p}{\partial x} + v \frac{\partial p}{\partial y} - c^2 u \frac{\partial \rho}{\partial x} - c^2 v \frac{\partial \rho}{\partial y} = \frac{\partial e / \partial \lambda}{\partial e / \partial p} W. \tag{7.10}$$

Hence we have expressions involving partial derivatives of the flow velocities, pressure and density.

7.4.3 Derivatives along the shock

Further equations for the derivatives of the flow variables can be obtained by considering derivatives along the shock front. We first consider the parameterisation of the shock $y = y_f(x)$ and define the slope and curvature

$$s = \frac{dy_f}{dx}, \tag{7.11}$$

$$\kappa = \frac{ds}{dx}. \tag{7.12}$$

For an oblique shock, discussed in section 6.4.2, it was shown that the post-shock flow variables are a function of the shock slope only. Therefore, for some flow variable $g = g(s)$, we can write

$$dg = \frac{dg}{ds} \frac{ds}{dx} \, dx = \frac{dg}{ds} \, \kappa \, dx, \tag{7.13}$$

where κ has been substituted from 7.12. Along the shock

$$dg = (dx, dy) \cdot \nabla g = dx\,(1, s) \cdot \nabla g. \tag{7.14}$$

Equating 7.13 and 7.14 gives

$$\kappa \frac{dg}{ds} = (1, s) \cdot \nabla g. \tag{7.15}$$

Dropping the function g and writing ∇ in Cartesian coordinates gives

$$\kappa \frac{d}{ds} = \frac{\partial}{\partial x} + s\frac{\partial}{\partial y}. \tag{7.16}$$

This expression relates derivatives along the shock to partial derivatives in x and y. For example, for the pressure 7.16 gives

$$\kappa \frac{dp}{ds} = \frac{\partial p}{\partial x} + s\frac{\partial p}{\partial y}. \tag{7.17}$$

To evaluate the LHS of this expression $p(s)$ must be known, which requires the solution to the shock relations and will be dependent upon the equation of state chosen. Equation 7.16 can be applied to each of the flow variables u, v, p, ρ and thus gives four equations in terms of partial derivatives w.r.t. x and y.

7.4.4 Curved Shock Equations

We are now in a position to determine the streamline curvature as a function of the shock curvature for a given shock slope s. The Euler equations 7.5-7.10 can be combined with the derivative along the shock (7.16) applied to the flow variables u, v, p, ρ. This gives eight equations with eight unknowns allowing for each of the partial derivatives of u, v, p, ρ to be determined behind the shock. It can be written as a linear system of the form

$$\mathbf{M}\,\mathbf{z} = \mathbf{b}, \tag{7.18}$$

where $\mathbf{M}$ is a matrix and $\mathbf{z}$ and $\mathbf{b}$ are column vectors. In this case we have

$$\mathbf{M} = \begin{pmatrix} \rho & 0 & 0 & \rho & u & v & 0 & 0 \\ \rho u & \rho v & 0 & 0 & 0 & 0 & 1 & 0 \\ 0 & 0 & \rho u & \rho v & 0 & 0 & 0 & 1 \\ 0 & 0 & 0 & 0 & -c^2 u & -c^2 u & u & v \\ 1 & s & 0 & 0 & 0 & 0 & 0 & 0 \\ 0 & 0 & 1 & s & 0 & 0 & 0 & 0 \\ 0 & 0 & 0 & 0 & 1 & s & 0 & 0 \\ 0 & 0 & 0 & 0 & 0 & 0 & 1 & s \end{pmatrix}. \tag{7.19}$$

$$\mathbf{z} = \begin{pmatrix} \frac{\partial u}{\partial x} \\ \frac{\partial u}{\partial y} \\ \frac{\partial v}{\partial x} \\ \frac{\partial v}{\partial y} \\ \frac{\partial \rho}{\partial x} \\ \frac{\partial \rho}{\partial y} \\ \frac{\partial p}{\partial x} \\ \frac{\partial p}{\partial y} \end{pmatrix}, \qquad \mathbf{b} = \begin{pmatrix} 0 \\ 0 \\ 0 \\ -\frac{\partial e/\partial \lambda}{\partial e/\partial p} W \\ \kappa \frac{du}{ds} \\ \kappa \frac{dv}{ds} \\ \kappa \frac{d\rho}{ds} \\ \kappa \frac{dp}{ds} \end{pmatrix}. \tag{7.20}$$

For a given equation of state $e = e(p, \rho, \lambda)$ and reaction rate W this system can be solved for the vector $\mathbf{z}$. With the partial derivatives of u, v obtained these can be substituted into equation 7.4 to compute the streamline curvature immediately behind the shock. If the reaction rate is formally zero behind the shock then the shock-curvature system is modified by setting $W = 0$ in $\mathbf{b}$.

7.4.5 Streamline Curvature for Polytropic EOS

We recall the polytropic EOS

$$e = \frac{p}{(\gamma - 1)\rho} - \lambda q. \tag{7.21}$$

To determine the streamline curvature where there is reaction at the shock the reaction rate must be specified. For the polytropic EOS previously published results [30] used a reaction rate of the form

$$W = \alpha \left(1 - \lambda\right)^m p^n, \tag{7.22}$$

where α, m and n are constants. With the equation of state and reaction rate specified an analytical expression for the streamline curvature can be obtained.

The oblique shock relations, for the polytropic EOS, have been derived in section 6.6.1. They gives expressions for the two components of velocity (u, v) in the (x, y) directions, the pressure and density behind the shock as a function of the shock slope s. They are given by,

$$u_s = \frac{2Ds}{(\gamma + 1)\left(1 + s^2\right)}, \tag{7.23}$$

$$v_s = \frac{D\left(\gamma - 1 + (\gamma + 1)\, s^2\right)}{(\gamma + 1)\left(1 + s^2\right)}, \tag{7.24}$$

$$\rho_s = \frac{(\gamma + 1)}{(\gamma - 1)}, \tag{7.25}$$

$$p_s = \frac{2D^2}{(\gamma + 1)\left(1 + s^2\right)}. \tag{7.26}$$

The strong shock assumption of $p_0 = 0$ has been used and the pre-shocked density $\rho_0 = 1$. Equations 7.23 -7.26 can be substituted into 7.16. These expression can then be used with the Euler equations 7.5 -7.10 to obtain expressions for the partial derivatives of the velocity components.

We now proceed to apply 7.16 to the shock relations. From equation 7.23

$$\begin{aligned}\frac{du_s}{ds} =& \frac{2D}{(\gamma+1)}\frac{d}{ds}\left(\frac{s}{(1+s^2)}\right),\\ =& \frac{2D}{(\gamma+1)}\left[\frac{1}{(1+s^2)}-\frac{2s^2}{(1+s^2)^2}\right],\\ \frac{du_s}{ds} =& \frac{2D}{(\gamma+1)}\left[\frac{1-s^2}{(1+s^2)^2}\right],\end{aligned}$$

which, by 7.16, gives

$$\frac{2D\kappa\left(1-s^2\right)}{(\gamma+1)\left(1+s^2\right)^2} = \frac{\partial u}{\partial x}+s\frac{\partial u}{\partial y}. \tag{7.27}$$

Applying the same procedure to 7.24

$$\begin{aligned}\frac{dv_s}{ds} =& \frac{D}{(\gamma+1)}\left[\frac{2\left(\gamma+1\right)s}{(1+s^2)}-\frac{2s\left(\gamma-1+(\gamma+1)\,s^2\right)}{(1+s^2)^2}\right],\\ =& \frac{2Ds}{(\gamma+1)\left(1+s^2\right)^2}\left[\gamma+s^2+1+\gamma s^2-\gamma+1-\gamma s^2-s^2\right],\\ \frac{dv_s}{ds} =& \frac{4Ds}{(\gamma+1)\left(1+s^2\right)^2}.\end{aligned}$$

Substituting into 7.16 gives

$$\frac{4D\kappa s}{(\gamma+1)\left(1+s^2\right)^2} = \frac{\partial v}{\partial x}+s\frac{\partial v}{\partial y}. \tag{7.28}$$

From 7.25 we have

$$0 = \frac{\partial \rho}{\partial x}+s\frac{\partial \rho}{\partial y}. \tag{7.29}$$

And finally from 7.26

$$\frac{-2s\kappa D^2}{\left(1+s^2\right)^2} = \frac{\partial p}{\partial x}+s\frac{\partial p}{\partial y}. \tag{7.30}$$

Substitution of these results into the vector b in 7.20 gives

$$b = \begin{pmatrix} 0 \\ 0 \\ 0 \\ \rho(\gamma-1)qW \\ \frac{2D\kappa\left(1-s^2\right)}{(\gamma+1)(1+s^2)^2} \\ \frac{4D\kappa s}{(\gamma+1)(1+s^2)^2} \\ 0 \\ \frac{-2s\kappa D^2}{(1+s^2)^2} \end{pmatrix}. \tag{7.31}$$

The solution to the linear system given by 7.18 was solved using Gaussian elimination to obtain expressions in the partial derivatives of the flow variables. These were then substituted into equation 7.4 to obtain an expression for the streamline curvature behind the shock. For $\gamma = 3$ (as used for previous SSA calculations) the post-shock streamline curvature is

$$K = \frac{s\left[16q\left(1+s^2\right)^3 W + 5D^3\kappa\left(1-2s^2\right)\right]}{D^3\left(1+s^2\right)^3}. \tag{7.32}$$

The first term inside the square braces is directly proportional to the reaction rate and is strictly positive. The second term, which is proportional to the shockwave curvature κ, is of the opposite sign (as $s < 1$). The effect of a reaction at the shock is therefore to reduce the magnitude of the streamline curvature.

If there is no reaction at the shock ($W = 0$) then 7.32 reduces to

$$K = \frac{5\kappa s\left(1-2s^2\right)}{\left(1+s^2\right)^2}. \tag{7.33}$$

This expression indicates that in the absence of the reaction term the streamline curvature is linearly proportional to the shock front curvature.

An interesting feature of equation 7.33 is that the sign of the curvature changes as the shock slope increases. By inspection of 7.33 this occurs when

$$s = \frac{1}{\sqrt{2}}.$$

This shock slope coincides with the point where the post-shock flow velocity is exactly sonic as shown by equation 6.58 in section 6.6.1.

7.4.6 Calculations

The post-shock streamline curvature is calculated for the polytropic equation of state with and without reaction at the shock. The reaction rate equation was that described in equation 7.22 and the calculations were performed for $n = 0, m = 1/2$. Data from SSA calculations in slab geometry was used as input for the shock curvature at each shock slope. The calculations of the streamline curvature, without the reaction term, were verified by comparing results to previous publications [53][57].

Figures 7.14-7.16 show how the streamline curvature varies for different detonation velocities, the curves display similar qualitative features. Without reaction at the shock the streamline curvature is positive and monotonically increasing as a function of shock slope. When reaction at the shock is included the streamline curvature is of opposite sign for a significant proportion along the shock surface and of a much smaller magnitude.

As the presence of the reaction term reduces the magnitude of the post-shock streamline curvature, negating the contribution from the curvature of the shock, this may explain why the SSA proves to be more successful with a power law reaction rate than when an induction-type reaction rate is used.

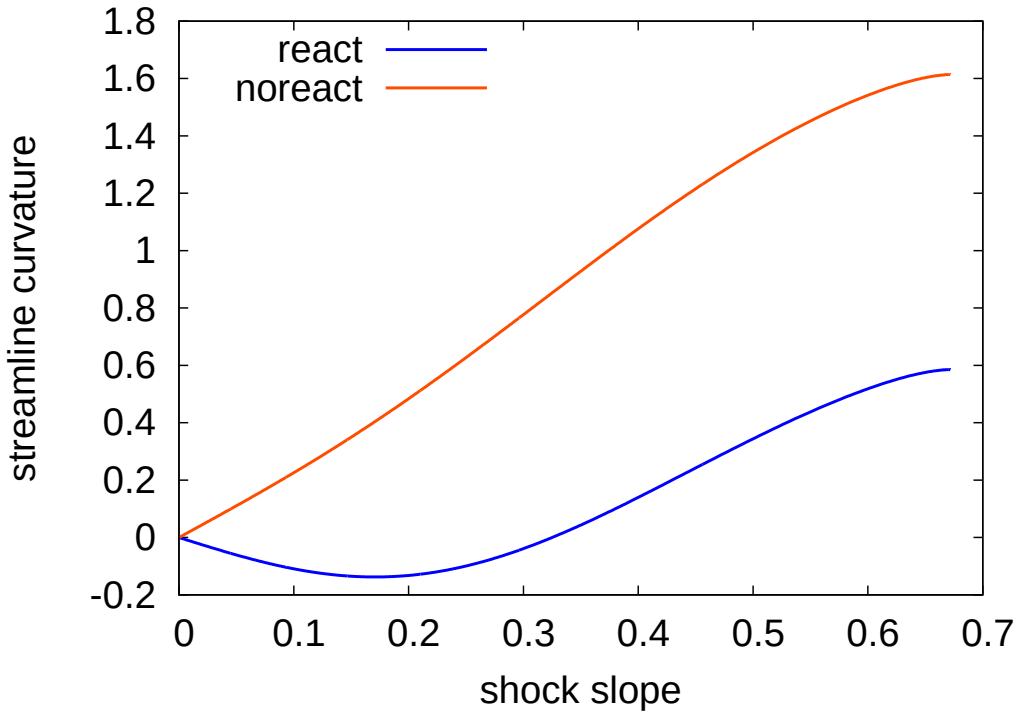

Figure 7.14: Streamline curvature as a function of shock slope for polytropic EOS with power law reaction rate $m = 0.5, n = 0.0$ and $D = 0.45$.

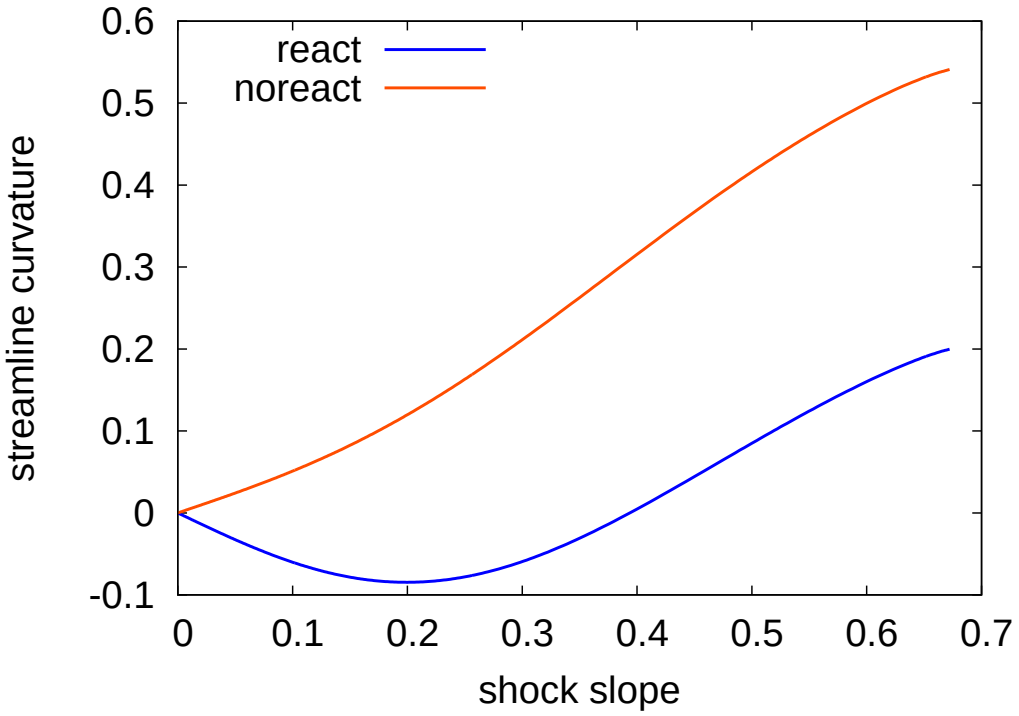

Figure 7.15: Streamline curvature as a function of shock slope for polytropic EOS with power law reaction rate $m = 0.5, n = 0.0$ and $D = 0.65$.

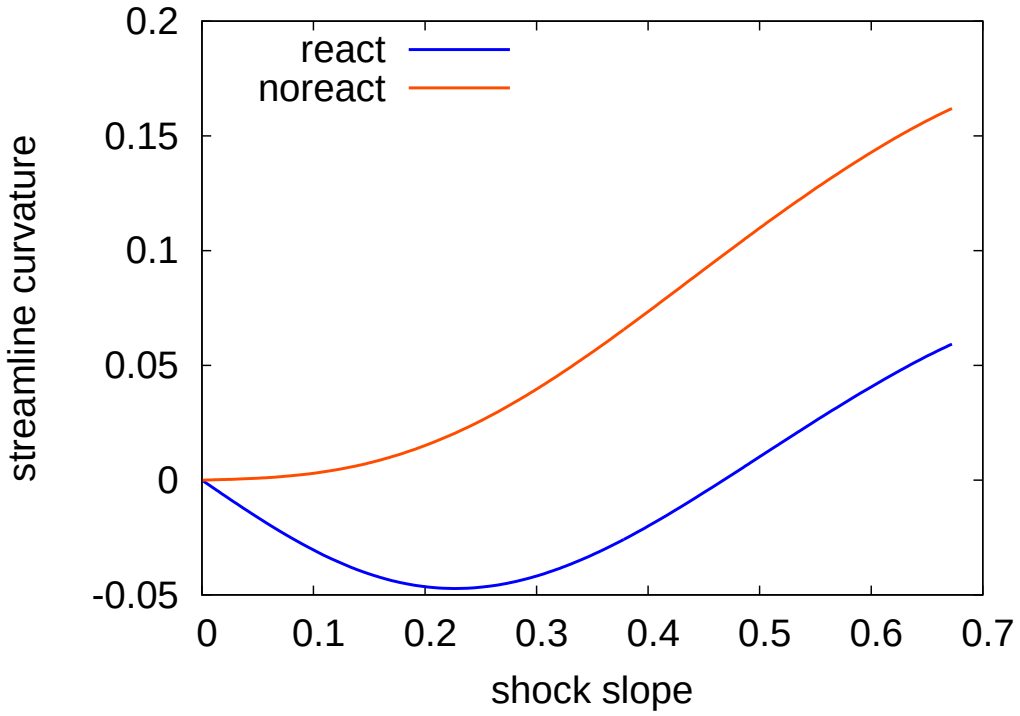

Figure 7.16: Streamline curvature as a function of shock slope for polytropic EOS with power law reaction rate $m = 0.5, n = 0.0$ and $D = 0.97$.

7.4.7 Curvature for CREST

We now consider the post-shock streamline curvature for the unreacted CREST EDC37 EOS. As the shock relations for the CREST equation of state must be solved numerically, the matrix equation to determine the streamline curvature must also be solved numerically.

For the CREST model there is formally zero reaction rate at the shock and thus in the curvature calculations there was no reaction. The results for CREST were compared to similar calculations for the polytropic EOS.

Figure 7.17 shows that for EDC37 the streamline curvature increases as shock slope increases, reaches a maximum and falls to zero. The sign of the streamline curvature changes before the post-shock sonic point. This coincides with the point where the streamlines begin to converge post-shock and the maximum shock slope that can be integrated to with the SSA. Figure 7.18 shows that the polytropic EOS behaves similarly to the CREST equation of state. However, the point at which the sign of curvature changes coincides exactly with the sonic point. In section 6.8.3 it was shown that when a reaction rate with a significant induction zone was used that the SSA failed to capture the curvature effects that are important near the edge of the rate-stick. As the qualitative behaviour, of the shock curvature as a function of shock slope, between the polytropic and CREST EOS is similar it can be concluded that the failure of the SSA to accurately reproduce shock shapes and diameter effect curves is due to the model failing to consider curvature effects.

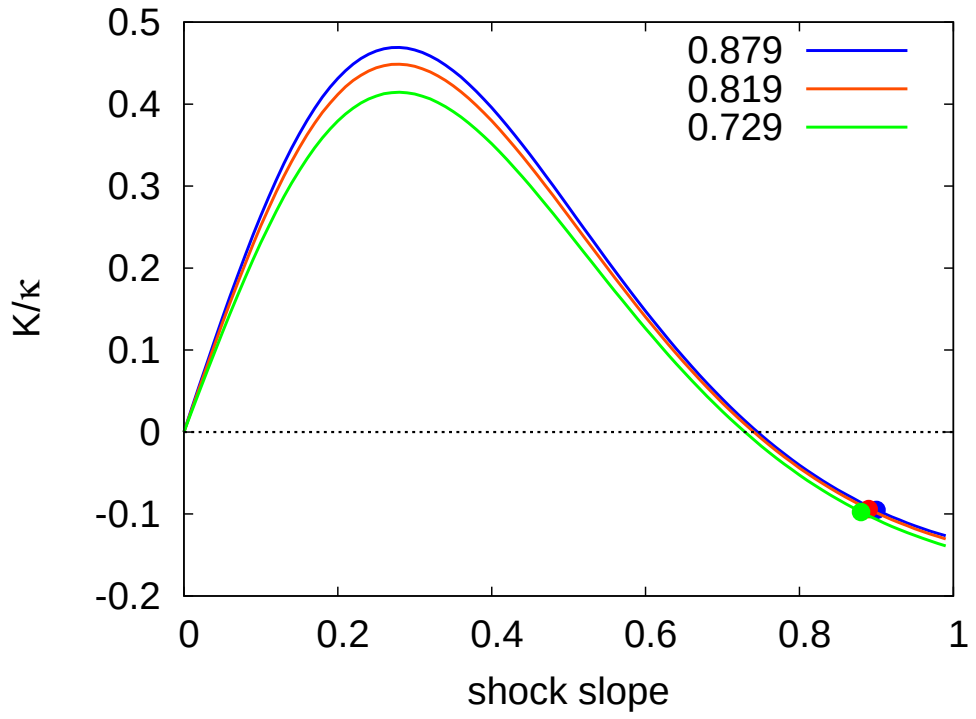

Figure 7.17: Streamline curvature as a function of shock slope for CREST EDC37 equation of state. The legend indicates the different detonation velocities (in $cm\,\mu s^{-1}$). The solid circles indicate the shock slope at which the post-shock flow becomes transonic.

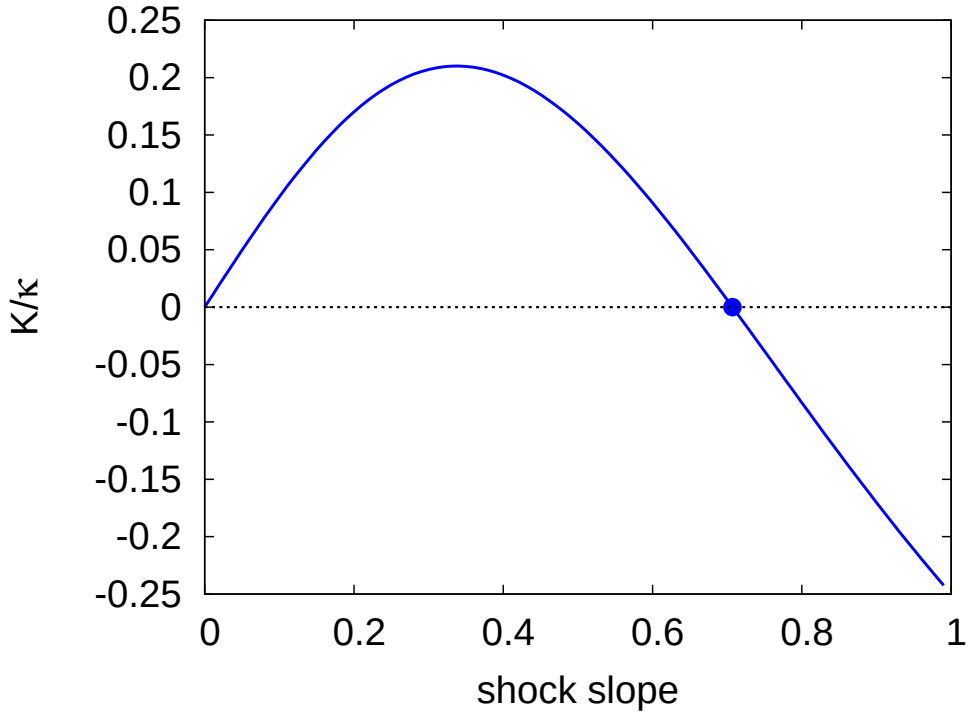

Figure 7.18: Streamline curvature as a function of shock slope for polytropic equation of state. The solid circle indicates the shock slope at which the post-shock flow becomes transonic. This curve is identical for all detonation velocities.

Chapter 8

Conclusions

In this thesis the SSA was implemented for a number of different explosives models including models where the reaction rate contained a significant induction zone before reaching a maximum. Previous work with the SSA had exclusively focused on a power law reaction rate where reaction is a maximum at the shock. In deriving the governing flow equations for the CREST reactive burn model a new relationship between the thermodynamic variables was developed. This mathematical implementation of the model was verified using one-dimensional simulations and compared to high resolution DNS calculations, where the CREST model was used, for the first time, in a Godunov-type numerical scheme. For a stationary shock it was shown that the entropy of the unreacted phase does not increase monotonically through the shock and is a result of the averaging function used to achieve second order accuracy. Moreover, for CREST, it was shown that the detonation velocity computed from a rate-stick calculation was not independent of the frame of reference in which the calculation was performed. This is in contrast with a polytropic EOS with a power law reaction rate where the detonation velocity is independent of the frame of reference of the calculation.

The SSA assumes that the streamlines are straight and diverging in the reaction zone. For a realistic equation of state it has been shown that the Crocco point, where the streamlines begin to converge behind the shock, is reached before the boundary condition defining the edge of the rate-stick. This result was verified with analysis of the DNS and, to the author's knowledge, has not been published before. Previous publications focused on the polytropic EOS where the streamlines are diverging up the boundary and the Crocco point coincides with the edge of the explosive. Failure to reach the charge edge boundary places a limitation on the modelling capabilities of the SSA for unconfined rate-sticks when a realistic EOS is used. However, analysis of high resolution DNS calculations showed that the Crocco point occurs very close to the edge of the rate-stick. Thus, if the SSA were accurate up to this point, the difference between the radius from the SSA and the DNS calculations would be small.

Unconfined rate-stick calculations with CREST explosive models showed that there was a large discrepancy between the size effect curves for the SSA and DNS calculations, which could not be explained by the inability of the SSA to integrate beyond the Crocco point. As the CREST reaction rate has an induction zone a state-insensitive power law reaction rate was implemented with the EDC37 EOS. Here, the SSA and DNS results were more closely matched, suggesting that the assumption that the streamlines are straight is a better assumption when a power law reaction rate is used. Moreover, the SSA and DNS results were in better agreement for confined rate-stick calculations. Here, curvature effects are reduced due to the lateral confinement provided by the confiner.

Inspection of the streamline shapes from the DNS calculations show that, with an induction zone, there is significant streamline curvature that coincides with the region of maximum reaction. In contrast, for the power law reaction rate the streamlines are very straight in the reaction zone. This suggests why the SSA is able to capture the

diameter effect curve accurately when a power law reaction rate is used and is less accurate when the reaction has an induction zone.

The streamline curvature at the shock was calculated for a polytropic EOS with and without reaction at the shock. It was shown that with the presence of a reaction term the sign of the curvature is changed and that the magnitude of the curvature is significantly reduced. Hence any curvature effects will be smaller when there is reaction at the shock. However, for a reaction with an induction zone the streamline curvature effects will be more significant. The post-shock streamline curvature, as a function of shock slope, was calculated using the CREST EDC37 explosive. It was shown that the magnitude of the streamline varies in a similar manner to that of the polytropic EOS.

In future work improving the accuracy of streamline based models would require consideration of the streamline curvature as part of the ansatz for the streamline shape. For a power law reaction rate there will be some curvature at the shock but the streamlines then remain very close to straight throughout the reaction zone. This would suggest that a streamline shape based upon the shock curvature may be effective. For an induction reaction rate equation the absence of reaction at the shock means that streamlines will curve away from the axis initially. However, when the reaction rate is significant, the DNS analysis shows that the streamlines then curve inwards. Predicting the magnitude of this curvature downstream of the shock may not be straightforward and could limit the predictive capability of any curved streamline model.

Appendices

Appendix A

Adiabatic Sound Speed

The adiabatic sound speed is given by [59],

$$c^2 = \left(\frac{\partial p}{\partial \rho}\right)_s . \tag{A.1}$$

Here s is the entropy. From the first law of thermodynamics we have

$$de = Tds - pdv = Tds + \frac{p}{\rho^2}d\rho,$$

where $v = 1/\rho$ has been used. For an adiabatic process $ds = 0$, expanding de assuming $e(p, \rho, \lambda)$

$$de = \left(\frac{\partial e}{\partial \rho}\right)_{p,\lambda} d\rho + \left(\frac{\partial e}{\partial p}\right)_{\rho,\lambda} dp + \left(\frac{\partial e}{\partial \lambda}\right)_{p,\rho} d\lambda = \frac{p}{\rho^2}d\rho.$$

The thermodynamic variables are assumed to be in local equilibrium such that the chemical reaction is frozen and $d\lambda = 0$, therefore

$$\left(\frac{\partial e}{\partial \rho}\right)_{p,\lambda} d\rho + \left(\frac{\partial e}{\partial p}\right)_{\rho,\lambda} dp = \frac{p}{\rho^2}d\rho.$$

Rearranging this expression and using the definition of the adiabatic sound speed A.1

$$c^2 = \left(\frac{p}{\rho^2} - \frac{\partial e}{\partial \rho}\right) \Big/ \frac{\partial e}{\partial p}, \tag{A.2}$$

which is an expression for the adiabatic sound speed for a material with equation of state $e = e(p, \rho, \lambda)$.

Appendix B

Derivation of the internal energy off an isentrope

The Grüneisen parameter is given by,

$$\Gamma = v \left(\frac{\partial p}{\partial e} \right)_v , \tag{B.1}$$

where v is the specific volume, p is the pressure and e is the specific internal energy. Γ is assumed to be independent of the internal energy, that is, $\Gamma = \Gamma(v)$. Integrating equation B.1 we obtain,

$$\frac{\Gamma}{v}(e - e_i) = p - p_i, \tag{B.2}$$

where the i subscript indicates the variable on a curve of constant entropy, this is the reference curve for the equation of state. Both forms of e_i and p_i are known. From the first law of thermodynamics, assuming constant entropy s, we can write,

$$\left(\frac{\partial e}{\partial v} \right)_s = -p. \tag{B.3}$$

Substituting equation B.3 into B.2 we obtain,

$$\left(\frac{\partial e}{\partial v} \right)_s = -p_i - \frac{\Gamma}{v}(e - e_i).$$

Rearranging this expression gives,

$$\left(\frac{\partial e}{\partial v}\right)_s + \frac{\Gamma}{v}e = -p_i + \frac{\Gamma}{v}e_i. \tag{B.4}$$

This equation is linear in e and is of the form,

$$\frac{\mathrm{d}e}{\mathrm{d}v} + P(v)e = Q(v).$$

To solve it we multiply each term by the integrating factor $\exp\left(\int (\Gamma/v)\,\mathrm{d}v\right)$ to give,

$$\begin{aligned}\frac{\mathrm{d}e}{\mathrm{d}v}\exp\left(\int (\Gamma/v)\,\mathrm{d}v\right) + \frac{\Gamma}{v}e\exp\left(\int (\Gamma/v)\,\mathrm{d}v\right) &= \exp\left(\int (\Gamma/v)\,\mathrm{d}v\right)\left(-p_i + \frac{\Gamma}{v}e_i\right),\\ \frac{\mathrm{d}}{\mathrm{d}v}\left[e\exp\left(\int (\Gamma/v)\,\mathrm{d}v\right)\right] &= \exp\left(\int (\Gamma/v)\,\mathrm{d}v\right)\left(-p_i + \frac{\Gamma}{v}e_i\right).\end{aligned}$$

Integrating with respect to v, noting that the entropy was constant for the differential equation,

$$e\exp\left(\int (\Gamma/v)\,\mathrm{d}v\right) = \int\left(-p_i + \frac{\Gamma}{v}e_i\right)\exp\left(\int (\Gamma/v)\,\mathrm{d}v\right)\mathrm{d}v + Z(s), \tag{B.5}$$

where $Z(s)$ is an integration constant that depends upon the entropy. We can define the function,

$$\tau = \exp\left(\int -(\Gamma/v)\,\mathrm{d}v\right). \tag{B.6}$$

Substituting for τ, from B.6, in equation B.5 gives,

$$\frac{e}{\tau} = \int\left(-p_i + \frac{\Gamma}{v}e_i\right)\frac{\mathrm{d}v}{\tau} + Z(s).$$

But on an isentrope, according to equation B.3, $\frac{\mathrm{d}e_i}{\mathrm{d}v} = -p_i$, so we can write,

$$\begin{aligned}\frac{e}{\tau} &= \int\left[\frac{\mathrm{d}e_i}{dv} + \frac{\Gamma}{v}e_i\right]\frac{\mathrm{d}v}{\tau} + Z(s),\\ &= \int\frac{\mathrm{d}e_i}{dv}\frac{\mathrm{d}v}{\tau} + \int\frac{\Gamma}{v}\frac{e_i}{\tau}\mathrm{d}v + Z(s)\end{aligned} \tag{B.7}$$

We can solve the first integral on the right-hand side of B.7 by parts,

$$\begin{aligned}\int \frac{\mathrm{d}e_i}{dv}\frac{\mathrm{d}v}{\tau} &= \int \frac{\mathrm{d}e_i}{dv}\frac{1}{\tau}\mathrm{d}v, \\ &= \frac{e_i}{\tau} + \int e_i \frac{1}{\tau^2}\frac{\mathrm{d}\tau}{\mathrm{d}v}dv.\end{aligned}$$

But, from equation (B.6), $\frac{\mathrm{d}\tau}{\mathrm{d}v} = \Gamma\tau/v$, therefore,

$$\int \frac{\mathrm{d}e_i}{dv}\frac{\mathrm{d}v}{\tau} = \frac{e_i}{\tau} - \int \frac{\Gamma}{v}\frac{e_i}{\tau}dv.$$

With this result we can immediately write equation B.7 as,

$$e = e_i + \tau Z(s). \tag{B.8}$$

This equation allows for the internal energy to be computed off the principal isentrope.

Bibliography

[1] W. Fickett and W. Davis, *Detonation: theory and experiment*. Courier Dover Publications, 1979.

[2] J. A. Zukas, W. Walters, and W. P. Walters, *Explosive effects and applications*. Springer Science & Business Media, 2002.

[3] C. Johansson and P. Persson, *Detonics of High Explosives (Academic, New York)*. 1970.

[4] A. Campbell, W. Davis, and J. Travis, "Shock initiation of detonation in liquid explosives," *Physics of fluids*, vol. 4, pp. 498–510, 1961.

[5] F. P. Bowden and A. D. Yoffe, *Initiation and growth of explosion in liquids and solids*. Cambridge University Press, 1985.

[6] C. M. Tarver, S. K. Chidester, and A. L. Nichols, "Critical conditions for impact- and shock-induced hot spots in solid explosives," *The Journal of Physical Chemistry*, vol. 100, no. 14, pp. 5794–5799, 1996.

[7] M. Baer and J. Nunziato, "A two-phase mixture theory for the deflagration-to-detonation transition (ddt) in reactive granular materials," *International journal of multiphase flow*, vol. 12, no. 6, pp. 861–889, 1986.

[8] J. Bdzil, R. Menikoff, S. Son, A. Kapila, and D. S. Stewart, "Two-phase modeling of deflagration-to-detonation transition in granular materials: A critical examination of modeling issues," *Physics of Fluids (1994-present)*, vol. 11, no. 2, pp. 378–402, 1999.

[9] J. Tringe, K. Vandersall, J. Reaugh, H. Levie, B. Henson, L. Smilowitz, and G. Parker, "Observation and modeling of deflagration-to-detonation (ddt) transition in low-density hmx," in *APS Shock Compression of Condensed Matter Meeting Abstracts*, vol. 1, p. 2005, 2015.

[10] A. Campbell, "Diameter effect and failure diameter of a tatb-based explosive," *Propellants, Explosives, Pyrotechnics*, vol. 9, no. 6, pp. 183–187, 1984.

[11] G. Sharpe and J. Bdzil, "Interactions of inert confiners with explosives," *Journal of engineering mathematics*, vol. 54, no. 3, pp. 273–298, 2006.

[12] F. Zhang, *Shock wave science and technology reference library*. Springer, 2009.

[13] J. Vorthman, G. Andrews, and J. Wackerle, "Reaction rates from electromagnetic gauge data," tech. rep., Los Alamos National Lab., NM (USA), 1985.

[14] S. Schoch, N. Nikiforakis, B. J. Lee, and R. Saurel, "Multi-phase simulation of ammonium nitrate emulsion detonations," *Combustion and Flame*, vol. 160, no. 9, pp. 1883 – 1899, 2013.

[15] E. Lee and C. Tarver, "Phenomenological model of shock initiation in heterogeneous explosives," *Physics of Fluids*, vol. 23, pp. 2362–2372, 1980.

[16] C. Handley, N. Whitworth, H. James, B. Lambourn, and M. Maheswaran, "The crest reactive-burn model for explosives," in *EPJ Web of Conferences*, vol. 10, p. 00004, EDP Sciences, 2010.

[17] G. J. Sharpe and S. Falle, "One-dimensional nonlinear stability of pathological detonations," *Journal of Fluid Mechanics*, vol. 414, pp. 339–366, 2000.

[18] D. L. Chapman, "Vi. on the rate of explosion in gases," *The London, Edinburgh, and Dublin Philosophical Magazine and Journal of Science*, vol. 47, no. 284, pp. 90–104, 1899.

[19] E. Jouguet, "Mechaniques des explosifs," *0. Doin et Fils, Paris*, 1917.

[20] Y. B. Zeldovich, "On the theory of the propagation of detonation in gaseous systems," *J. Experiment. Theoret. Phys*, vol. 10, pp. 542–568, 1940.

[21] J. von Neumann, "Theory of detonation waves," *John von Neumann, Collected Works. Macmillan, New York*, vol. 9, 1942.

[22] W. Doering, "On detonation processes in gases," *Ann. Phys.*, vol. 43, pp. 421–436, 1943.

[23] H. Eyring, R. E. Powell, G. H. Duffy, and R. B. Parlin, "The stability of detonation.," *Chemical Reviews*, vol. 45, no. 1, pp. 69–181, 1949.

[24] H. Jones, "A theory of the dependence of the rate of detonation of solid explosives on the diameter of the charge," in *Proceedings of the Royal Society of London A: Mathematical, Physical and Engineering Sciences*, vol. 189, pp. 415–426, The Royal Society, 1947.

[25] W. W. Wood and J. G. Kirkwood, "Diameter effect in condensed explosives. the relation between velocity and radius of curvature of the detonation wave," *The Journal of Chemical Physics*, vol. 22, p. 1920, 1954.

[26] J. Bdzil, "Steady-state two-dimensional detonation," *Journal of Fluid Mechanics*, vol. 108, pp. 195–226, 1981.

[27] J. Yao and D. Stewart, "On the dynamics of multi-dimensional detonation," *Journal of Fluid Mechanics*, vol. 309, pp. 225–275, 1966.

[28] T. Aslam, J. Bdzil, and L. Hill, "Extensions to dsd theory: Analysis of pbx9502 rate stick data," in *Eleventh Symposium (Intl) on Detonation*, pp. 21–29, 1998.

[29] T. D. Aslam, J. B. Bdzil, and D. S. Stewart, "Level set methods applied to modeling detonation shock dynamics," *Journal of Computational Physics*, vol. 126, no. 2, pp. 390–409, 1996.

[30] S. D. Watt, G. J. Sharpe, S. A. Falle, and M. Braithwaite, "A streamline approach to two-dimensional steady non-ideal detonation: the straight streamline approximation," *Journal of Engineering Mathematics*, vol. 75, no. 1, pp. 1–14, 2012.

[31] L. D. Landau and E. M. Lifshitz, *Fluid mechanics, by LD Landau and EM Lifshitz*. Pergamon Press, 1959.

[32] M. Cowperthwaite, "An exact solution for axial flow in cylindrically symmetric, steady state detonation in polytropic explosive with an arbitrary rate of decomposition," *Physics of Fluids*, vol. 6, no. 3, pp. 1357–1378, 1994.

[33] D. S. Stewart and J. Yao, "The normal detonation shock velocity–curvature relationship for materials with nonideal equation of state and multiple turning points," *Combustion and flame*, vol. 113, no. 1, pp. 224–235, 1998.

[34] I. Kirby and G. Leiper, "A small divergent detonation theory for intermolecular explosives," in *Proceedings of the 8th International Symposium on Detonation, Albuquerque*, vol. 176186, 1985.

[35] G. Sharpe and M. Braithwaite, "Steady non-ideal detonations in cylindrical sticks of explosives," *Journal of engineering mathematics*, vol. 53, no. 1, pp. 39–58, 2005.

[36] N. Whitworth, "Mathematical and numerical modelling of shock initiation in heterogeneous solid explosives," *PhD Thesis, Cranfield University*, 2008.

[37] N. Whitworth, "Application of the crest reactive burn model to two-dimensional pbx 9502 explosive experiments," in *SHOCK COMPRESSION OF CONDENSED MATTER-2007: Proceedings of the Conference of the American Physical Society Topical Group on Shock Compression of Condensed Matter*, vol. 955, pp. 881–884, AIP Publishing, 2007.

[38] N. Whitworth and M. Childs, "Determination of detonation wave boundary angles via direct numerical simulations using crest," in *APS Shock Compression of Condensed Matter Meeting Abstracts*, vol. 1, p. 2002, 2015.

[39] M. Cowperthwaite, "A constitutive model for calculating chemical energy release rates from the flow fields in shocked explosives," in *Seventh Symposium (International) on Detonation*, pp. 498–505, 1981.

[40] P. Lax and B. Wendroff, "Systems of conservation laws," *Communications on Pure and Applied mathematics*, vol. 13, no. 2, pp. 217–237, 1960.

[41] S. K. Godunov, "A difference method for numerical calculation of discontinuous solutions of the equations of hydrodynamics," *Matematicheskii Sbornik*, vol. 89, no. 3, pp. 271–306, 1959.

[42] E. F. Toro, *Riemann solvers and numerical methods for fluid dynamics: a practical introduction*. Springer Science & Business Media, 2013.

[43] E. F. Toro, M. Spruce, and W. Speares, "Restoration of the contact surface in the hll-riemann solver," *Shock waves*, vol. 4, no. 1, pp. 25–34, 1994.

[44] P. Batten, N. Clarke, C. Lambert, and D. Causon, "On the choice of wavespeeds for the hllc riemann solver," *SIAM Journal on Scientific Computing*, vol. 18, no. 6, pp. 1553–1570, 1997.

[45] S. Falle, S. Komissarov, and P. Joarder, "A multidimensional upwind scheme for magnetohydrodynamics," *Monthly Notices of the Royal Astronomical Society*, vol. 297, no. 1, pp. 265–277, 1998.

[46] S. Falle, "Self-similar jets," *Monthly Notices of the Royal Astronomical Society*, vol. 250, no. 3, pp. 581–596, 1991.

[47] T. W. Roberts, "The behavior of flux difference splitting schemes near slowly moving shock waves," *Journal of Computational Physics*, vol. 90, no. 1, pp. 141–160, 1990.

[48] J. J. Quirk, "A contribution to the great riemann solver debate," *International Journal for Numerical Methods in Fluids*, vol. 18, no. 6, pp. 555–574, 1994.

[49] T. H. Pulliam, "Artificial dissipation models for the euler equations," *AIAA journal*, vol. 24, no. 12, pp. 1931–1940, 1986.

[50] C. Handley, "The crest reactive burn model," in *SHOCK COMPRESSION OF CONDENSED MATTER-2007: Proceedings of the Conference of the American Physical Society Topical Group on Shock Compression of Condensed Matter*, vol. 955, pp. 373–376, AIP Publishing, 2007.

[51] T. D. Aslam and J. B. Bdzil, "Numerical and theoretical investigations on detonation-inert confinement interactions," in *The Twelfth Symposium (International) on Detonation*, pp. 483–488, 2002.

[52] C. J. Chapman, *High speed flow*, vol. 23. Cambridge University Press, 2000.

[53] P. RAO, "Streamline curvature and velocity gradient behind curved shocks.," *AIAA Journal*, vol. 11, no. 9, pp. 1352–1354, 1973.

[54] L. Hill, J. B. Bdzil, and T. D. Aslam, "Front curvature rate stick measurements and detonation shock dynamics calibration for pbx 9502 over a wide temperature range," in *Eleventh International Detonation Symposium*, pp. 1029–1037, 1998.

[55] L. Hill, R. Gustavsen, R. Alcon, and S. Sheffield, "Shock initiation of new and aged pbx 9501 measured with embedded electromagnetic particle velocity gauges," tech. rep., Los Alamos National Lab., NM (US), 1999.

[56] C. Handley, "Lagrangian analysis of velocity gauge data to determine reaction rate histories in edc37," in *SHOCK COMPRESSION OF CONDENSED MATTER-2005: Proceedings of the Conference of the American Physical Society Topical Group on Shock Compression of Condensed Matter*, vol. 845, pp. 1073–1076, AIP Publishing, 2006.

[57] T. Thomas, "On curved shock waves," *Journal of Mathematics and Physics*, vol. 26, no. 1, pp. 62–68, 1947.

[58] S. Mölder, "Curved shock theory," *Shock Waves*, pp. 1–17, 2016.

[59] H. W. Liepmann and A. Roshko, *Elements of gas dynamics*. Courier Dover Publications, 1957.